Hydrodynamic stability of a 3D printed concrete artificial reef design

MSc Thesis

Danai Chronopoulou

TU Delft

Coastruction

Hydrodynamic stability of a 3D printed concrete artificial reef design

MSc Thesis

by

Danai Chronopoulou

Student Name	Student Number
D. Chronopoulou	6073840

Thesis committee:	Dr. M.F.S Tissier	TU Delft, Chair
	Prof. Dr. M.R.A van Gent	TU Delft & Deltares
	Dr. N. Fani	Coastruction
	Ir. S. Haage	Boskalis
Project Duration:	August 2025 - May 2026	

TU Delft

Coastruction

Acknowledgments

This report represents my thesis to obtain the title Master of Science in Hydraulic Engineering at the Faculty of Civil Engineering and Geosciences at Delft University of Technology. It also marks the end of my journey as a student at TU Delft. Somehow, it feels like yesterday that I applied to come here, yet at the same time it is as if a century has passed. Through thick and thin, I would like to take this moment to express my gratitude to all the people that helped me and supported me along the way.

First and foremost, I would like to thank my committee as a whole, for contributing in me seeing this thesis as an enjoyable opportunity and never as a bureaucratic obligation. I can say with no hesitation that I have felt so much inspiration, admiration and respect for each and every one of you, and I am deeply grateful for both your time and your contribution in shaping my academic character. That being said, I would like to especially thank Marion, the chair of my committee, for her constant support and guidance, which I do not take for granted. Most importantly I want to thank you for sharing my excitement for the project, as sharing my findings with you and receiving your feedback and your ideas made me leave every meeting feeling energized and inspired about my work. I would also like to thank the rest of my committee members individually, Marcel, your calm and quick responses to my questions helped me to remain focused and not get off track. To Samantha, your insightful input and your practical perspective added another dimension to my topic, one that I found particularly exciting and valuable to explore.

To Nadia specifically a special thanks for trusting me with this topic and for giving me the opportunity to work on it. I also want to thank the entire team of Coastruction, for hosting me and for always making me feel welcome. Nadia, your positivity and ingenuity is definitely also reflected in the team of people you have built and getting to be part of it was really inspiring.

To the people from Deltares, thank you allowing me to work in your facilities, which had once felt like a distant unachievable dream. To Ivo and Joost, thank you for your guidance with planning the experiments and processing the results. Also, to Danny and Marlies and thank you for your practical support and for making the experiments even more enjoyable with your presence.

Lastly, I would like to thank my family and friends for supporting me through this journey of mine. And to my brother Ektoras, thank you for your truly unconditional support and for helping me remain stable during a thesis all about instability. I don't think I could have done it without you.

Danai Chronopoulou
Delft, May 2026

Abstract

Coral reefs are vital ecosystems that support marine biodiversity, yet their populations are declining. In response, artificial reef structures structures have been installed in several locations, to promote coral growth. In recent years, as ecological awareness has increased and initiatives such as Building with Nature have gained recognition, artificial reefs have been acknowledged beyond their ecological role, as potential sustainable engineering solutions which could help mitigate various coastal problems. Among the different AR solutions available, Coastruction is a company that specializes in 3D-printed artificial reef designs tailored to the ecosystem in which they are placed. As part of the 'Coral reef RESToration to reduce island flooding' (CREST) initiative, a project led by TU Delft in collaboration with Plymouth University, Deltares, Boskalis, they developed a design intended for an artificial reef restoration in a fringing reef environment. While its wave attenuation performance has been tested, the next step and the main objective of this thesis is to evaluate its stability under representative wave conditions found on a fringing reef.

As such, small scale experiments were conducted in the Western Scheldt flume in Deltares. The bathymetry used in the experiments was the same as that used in CREST, scaled down by a factor of 1:6.25 and it consisted of a foreshore with a slope of 1.4:5, intended to recreate fringing reef conditions. During the experiments, two artificial reef units with the same shape but different scaled-down dimensions were tested, with nominal printed heights of 4 and 5 cm. The analysis focus mainly on the stability of isolated elements, although full reef configurations were also explored experimentally.

To simplify the assessment of the stability of Coastruction's design, two sub questions are formed 1)examine how the offshore wave climate affects the hydrodynamic stability of individual reef units, by testing a) how the presence of the fringing reef transforms the offshore wave with particular attention to the role of infragravity waves on the reef flat; and second and 2) evaluate the consistency of stability predictions obtained from the Shields and Morison methods using laboratory time-series data, by comparing them with the observed stability outcomes.

Conducting the experiments showed that the transition point for instability was observed under the low water between conditions C9 (Hs = 0.16 m, Tp = 3 sec) and C11 (Hs=0.21m, Tp = 2.31 sec) for irregular waves, while both elements were stable under all the regular waves.

The analysis of the resulting forcing indicated that due to intense wave breaking imposed by the reef slope, combined with non linear interactions contributes to the enhancement of the infragravity waves (IG), which become the dominant wave motion in the low water level conditions WL05. For WL11 the presence of IG is magnified however to a lesser extent, resulting in a bimodal spectrum. As velocity was the main forcing parameter in the stability formulations, the higher values observed for WL05 were consistent with the corresponding unstable conditions.

Concerning the predictability of the stability formulations proposed, it is concluded that the Shields' method fails to predict the stability patterns observed in the context of the given hydraulic conditions, likely due to violations of several assumptions underlying its derivation. Regarding the Morison method, its effectiveness depends on the definition of the input parameters, where considering that the resulting forcing is bimodal, the assumption of representing the entire reef by an equivalent monochromatic component appears to be a simplification that results in reduced predictability. Instead, if the contribution of each frequency band in shaping the force components is explored separately, the method provides more efficient predictions. Constructing the force time series utilizing velocity measurements showed that infragravity waves influence stability by imposing a low frequency oscillation, which combined with the persistent short scale oscillation of the sea swell waves contributes in initiating motion. Therefore, it is concluded that the predictability of the Morison formulation, as is traditionally defined is limited and instead a more suitable approach is to substitute the velocity term using the infragravity component and the acceleration term using the sea-swell component.

Acknowledging the inherent uncertainty in the results, further research is required to evaluate the effectiveness of the proposed approach. As a first step, uncertainty should be reduced by obtaining direct force measurements to calibrate the force coefficients and by expanding the experimental dataset, particularly for conditions with varying infragravity-wave contributions. If such improvements are not feasible, applying a safety factor to the estimated required weight is recommended. Nonetheless, the presence of both IG and the SS waves in shaping the resulting weight is evident in a fringing reef environment, and thus more emphasis should be given in research where the contribution of these two frequency bands are considered.

Contents

1

Introduction

Coral reef systems are some of the most diverse ecosystems on earth. They cover only 1 % of the world's ocean, however they are home to about 25% of all marine species, attracting numerous types of fish, corals, invertebrates and other animals (NOAA 2024), thus proving their importance in sustaining marine biodiversity. Coral reefs also contribute to carbon and nutrient cycling, as certain types of plant life inhabiting these ecosystems, absorb carbon dioxide and release oxygen. These are very important processes for the oceans, as they help maintaining the ocean's water quality by filtering the water and producing oxygen.

In addition to their great ecological value, coral reefs have been found to play an important role in coastal protection (Ferrario et al. 2014). As an example, findings from Ferrario et al. (2014) showed that the influence of the complete reef morphology, which consists of the fore-reef, the reef crest and the reef flat, as shown in figure 1.1, exhibited an average wave height reduction of 64% and a maximum value observed being as high as 84% . By attenuating incoming waves, the wave forces and currents acted on the shore are weakened, which reduces the magnitude of beach erosion. The wave attenuation also results in a reduction of the wave height that reaches the shore, helping with wwave driven flooding, especially in low lying areas. Furthermore, coral reefs can act as a natural barrier, trapping sediment within the reef flat which that would otherwise be moved offshore, which helps sustain the beach's cross-shore profile.

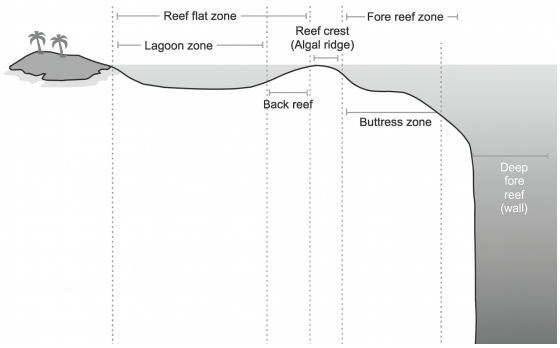

Figure 1.1: General classification of reef zones

Nevertheless, despite their ecological and protective importance, coral reefs worldwide are facing severe and accelerating threats. In recent years, direct and indirect human interventions, that range from tourism and overfishing, to pollution and climate change, have led to the degradation of many of the existing reefs and a significant decline in the numbers of the reefs in general (Harris 2004). Climate change in particular has led to the occurrence of more extreme and frequent weather conditions and natural disasters (Trégarot et al. 2023). The combination of more severe storms and the loss of coral reefs, results in increased energy reaching the shores which increases the risk of flooding (Ferrario et al. 2014).

To mitigate these effects, efforts have been made to restore the degraded coral fields by deploying Artificial Reefs (ARs). Artificial reefs are structures that are created in a way that resembles natural coral reefs. As their original conventional use was focused on ecosystem restoration, most of the doc-

umented cases found in literature referring to ARs, explore their impact on ecology, fishery and management (Baine 2001). Additionally, considering the only recent recognition of the contribution of coral reefs in coastal protection, less references exist that address the potential of using them as a coastal protection measure. Nonetheless, this trend is beginning to shift and the topic is gaining increasing attention. As the ecological movement has increased its influence and support from the people, there has been a general shift in policies and engineering towards more sustainable practices. In line with that trend, coastal management, erosion mitigation and protection measures now opt for soft and novel eco friendly solutions (Lokesh, Sundar, and Sannasiraj 2013). Within this context, the installation of ARs presented a great opportunity to combine ecological restoration with coastal protection.

Reflecting this emerging research direction, projects have been developed to investigate the effectiveness of artificial reefs in coastal protection. Among others, one such project, that investigates the interactions between artificial reefs and their surrounding hydrodynamics, is the CREST project. The 'Coral reef RESToration to reduce island flooding' (CREST) project, is an initiative led by Delft University of Technology in collaboration with Plymouth University, Deltares, Boskalis and Coastruction. Their aim is to acquire information on the hydrodynamic response of a fringing reef environment including artificial reef elements installed on the reef flat. As part of the project, large scale experiments have been conducted in the Delta flume in Deltares where the artificial reef units, placed on the bottom of the flume, were tested against the most optimal reef restoration design to maximize energy dissipation (Takens 2024) and to explore how the density of the restoration affects nearshore hydrodynamics and in-canopy flow (Albers 2025). A photograph of the artificial reef units used throughout the experiments are shown in figure 1.2 below.

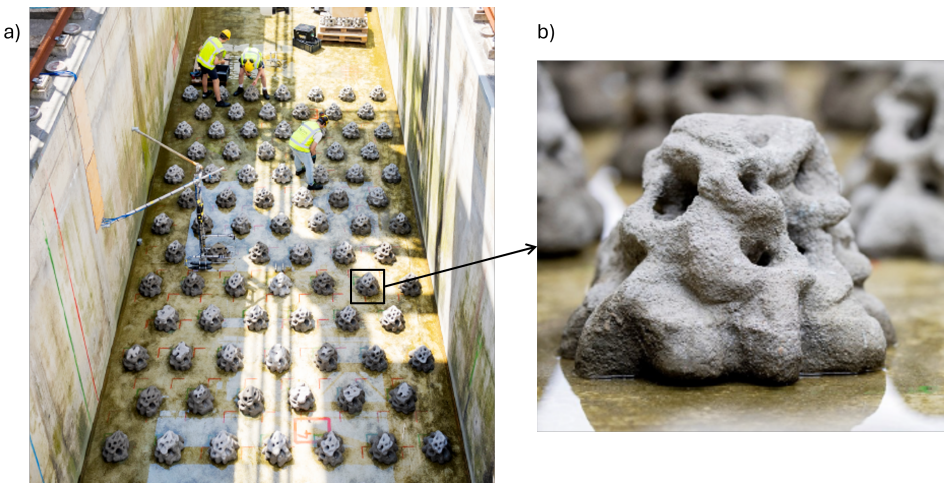

Figure 1.2: Photos of the 3D printed AR units during the CREST experiments, taken from Takens (2024), a) full reef restoration placed on the Delta Flume, b) Coastruction's AR design used during the experiments.

The aforementioned units used in the CREST experiments were provided and designed by Coastruction. Coastruction is a 3D-printing startup company founded in 2021, whose goal is to design, produce and install 3D-printed Purpose Built Reefs (PBRs) to aid in the restoration of damaged reef ecosystems and protect vulnerable coastlines.
In contrast with most 3D printing companies that, either specialize in mass production of simple designs or creating detailed prints on a smaller scale, Coastruction has developed a printer whose aim is to combine both those elements as best as possible. Their printer uses the pioneering technique of powder bed technology which allows completing intricate designs in a fast rate, giving them a competitive advantage in the job market. The high design flexibility of their printer creates the opportunity of customized and site specific reef installations, which aligns perfectly with one of the company's core principles, that is that there is no one-size-fits-all solution. Some of Coastruction's designs are presented in figure 1.3:

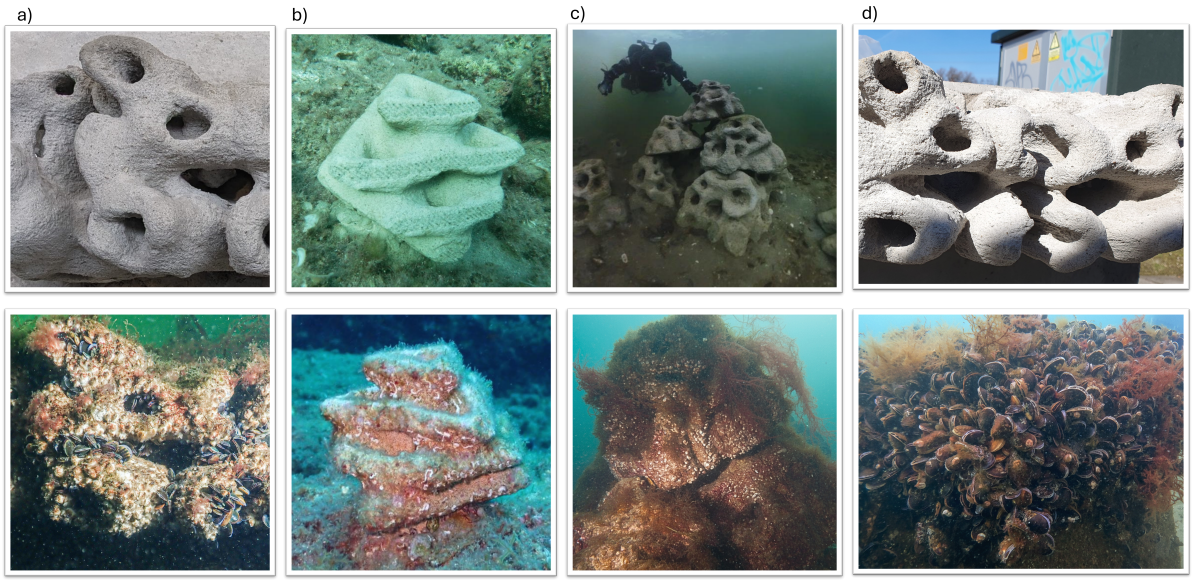

Figure 1.3: Artificial reef designs developed by Coastruction, before and after installation, a) Oostvoornse lake, 6 months apart, b) Sardinia, 5 months apart, c) Oostvoornse lake, 2.5 years apart, d) Oostvoornse lake, 2.5 years apart

While working on the CREST project, they developed the AR design shown in figure 1.2, intended to form an artificial reef restoration which can be used for coastal protection and to promote coral reef restoration at a low-lying island like the Maldives.
The success of the AR restoration in attenuating waves has already been tested in the CREST experiments conducted. A further critical step toward its practical implementation, and the primary motivation of the main research goal of this thesis, is to assess its stability.

1.1. Research Objective and Research Questions

Considering that the artificial reef was specifically designed to be installed in a given environment, its stability must be evaluated under the corresponding hydrodynamic conditions. Therefore, this research aims to perform a case specific analysis to assess the hydrodynamic stability of the artificial reef element that was used in the CREST experiments, under the hydrodynamic conditions that are typically found in a fringing reef environment. To identify stability under these conditions, small scale laboratory experiments are performed in the Scheldt flume in Deltares.

The experiments intend to investigate the hydrodynamic stability of Coastruction's design focusing primarily the isolated AR unit, while secondary experiments are also performed that explore the stability of the complete reef restoration. Two elements varying in size are examined, both of the same shape, which consist of a differently scaled down version of the original AR element used in the CREST experiments. In terms of the full artificial reef configuration, one geometry will be explored, and its location across the reef flat will be kept constant.

As the potential target installation locations for the reef restoration have been defined, the forcing conditions are established based on representative wave climates characteristic of low-lying coral reef islands in the Indian and Pacific Oceans. The stability of the AR elements is examined under unidirectional forcing limited to incident waves, not considering the effect of currents or scour.

To frame the research performed, the following research questions are formed.

Main Research Question:

> ***What is the hydrodynamic stability of the artificial reef design previously used in the CREST project?***

With the following sub-Questions:

How is the offshore wave climate affecting the hydrodynamic stability of individual artificial reef units of varying height over a fringing reef?

- How does the presence of a fringing reef transform the offshore wave climate into the hydrodynamic forcing that reaches the shore?
- Does the presence of infragravity waves on the reef flat, created by the irregular wave field, lead to a greater instability of the units?

How consistent are the predictions derived from the Morison and Shields' methods, using time-series data from the laboratory experiments as input, compared to the observed stability outcomes?

2

Theoretical Background

2.1. Hydrodynamic Processes at Reefs

Understanding the hydrodynamic processes that occur in reef environments is an essential step before assessing the stability of an artificial reef. These processes require further consideration as they are very different from the hydrodynamic patterns typically observed on a sandy beach. The observed differences are attributed to the characteristic morphology of fringing reefs and to the complex patterns of canopy flow dynamics.

2.1.1. Canopy Flow dynamics

As the example of flow over a coral reef is very specific, a popular approach, is to treat flow similarly to flow propagating through a vegetated field or a field of elements with rough surfaces termed as ”canopies”. To simplify the study even further, all reef elements will be considered as vertically placed cylinders, thus forming an ideal canopy. Then flow over the coral reef can be studied similarly to canopy flow. A characteristic of canopy flow is that when waves propagate through the canopy, interaction of flow with cylinders, causes wave energy dissipation, wave height reduction and overall wave attenuation. Two important processes that affect the flow, are sheltering and blockage:

- **Sheltering** occurs when downstream cylinders are placed in the wake of the upstream ones, where flow decelerates, resulting in reduced drag forces. This effect depends on whether flow excursion, (denoted in figure 2.1 as ξ), is sufficiently long to reach the next neighboring cylinder.Some studies suggest that for sparse arrays, sheltering effects can be neglected and the drag force is described only by blockage.
- **Blockage** occurs when the lateral spacing of the cylinders is small, causing flow to accelerate though the cross-section and drag forces on the cylinders to increase.

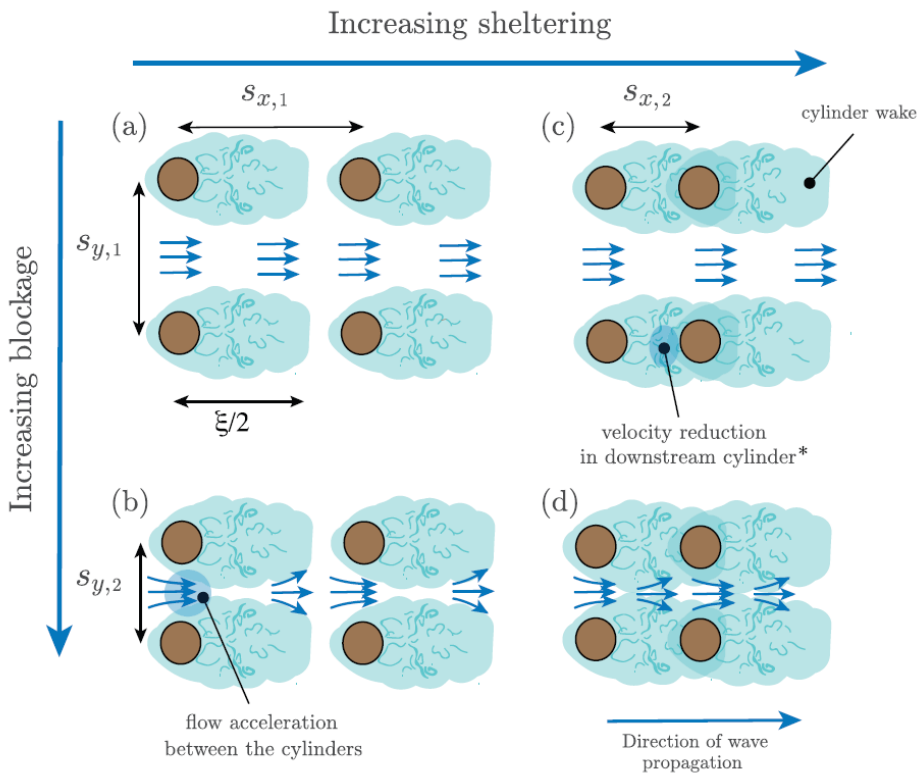

Figure 2.1: Sheltering and blockage effects (Figure from (Gijón et al. 2021))

As illustrated in figure 2.1, small lateral spacing S_y increases blockage effects while smaller streamwise separation S_x increases sheltering effects. Extending this concept, (Gijón et al. 2021; Mendez and Losada 2004; Phan et al. 2019; Bonakdar and Oumeraci 2015) have proven that for a given canopy geometry, variations in density and cylinder dimensions, influence the spacing between the elements and thus the magnitude of sheltering and blockage. These factors significantly influence the resulting hydrodynamics, as they govern the spatial variability of the in-canopy flow velocity, and thus the resulting hydrodynamic forces acted on each individual element.

A way to quantify the effect of the presence of the canopy in flow is through wave attenuation, expressed either in terms of wave height reduction or energy dissipation. Wave height attenuation can be quantified with the use of the transmission coefficient K_t which is defined as:

$$K_t = \frac{H}{H_0} \tag{2.1}$$

Where: H [m] = Incoming wave height just downstream the last row of cylinders
H_0 [m] = Incoming wave height at the toe of the first row of cylinders

A small transmission coefficient K_t implies that the reef was successful in attenuating the wave height. Gijón et al. (2021) found that short-period waves, present a smaller K_t than long-period waves, implying that shorter waves dissipate more. They also reported that increased canopy density produces a similar effect, of a reduced K_t, which is consistent with observations from Phan et al. (2019). Furthermore, both Gijón et al. (2021) and Phan et al. (2019) state that the transmission rate decreases with increasing the number of rows. A decreasing transmission rate already suggests that dissipation of the wave height does not occur linearly across the length of the canopy. Figures from Phan et al. (2019) explicitly support that claim, showing biggest transmission rates occurring in the first meters of the configuration.

Regarding wave energy dissipation, many formulations have been proposed in literature. In general, the dissipation of wave energy over a field of objects, can be represented by the work done by the wave-induced horizontal forces F_x, acting on the objects. Therefore force and energy dissipation are

analogous. Furthermore, regardless of which specific formulation is used, many of them (Dalrymple, Kirby, and Hwang 1984; Mendez and Losada 2004; Gijón et al. 2021; Lowe et al. 2007) follow a general form like the one proposed by Jonsson (1966) for dissipation over a rough surface such as:

$$\varepsilon = \frac{2}{3\pi}\rho f_e \left(U_{\infty,w}^{max}\right)^3 \tag{2.2}$$

Where:	ε	[m/s]	=	Wave energy dissipation
	f_e	[-]	=	Wave energy dissipation factor
	$U_{\infty,w}^{max}$	[m/s]	=	Maximum horizontal velocity above the rough surface

The wave energy dissipation factor, f_e, includes the influence of the characteristics of the canopy's design and in many cases is a function of the drag coefficient C_d. Consequently, the velocity fieldand the forces exerted on the reef are all parameters directly linked to dissipation, where, studying one of them, provides insights into the behavior of the other.

Observations from Gijón et al. (2021) showed that placing one row of cylinders or a full reef restoration on the flume, resulted to a velocity in the first row that is 2 to 2.5 times higher compared to a case of a single cylinder present. Measurements gathered from more downstream rows within the restoration revealed what the K_t graphs from Phan et al. (2019) had already proposed, which is that the downstream rows experience reduced velocities.
A similar pattern with the velocity observations is identified in measured forces; the first rows experience approximately double the force than what an isolated cylinder would.

Apart from comparing velocity and force measurements directly, Gijón et al. (2021) also used the KC Keulegan-Carpenter number to explore the variation in measured energy dissipation. KC is a dimensionless number used to characterize wave-structure interaction and it represents the relative importance of drag and inertia forces acting on the elements of the reef. It is defined as:

$$KC = \frac{UT}{D} \tag{2.3}$$

Where:	U_m	[m/s]	=	Maximum flow velocity
	T	[s]	=	Wave period
	D	[m]	=	Cylinder's diameter

More specifically, the total hydrodynamic force acting on the reef consists of three main components: skin friction forces, often neglected, form drag forces, related to flow separation behind the poles and inertia forces, related to the acceleration of the wave driven force. The value of the KC number helps identify which one of the forces is dominant. Small KC numbers correspond to inertia dominated cases, whereas big KC numbers ($KC > 20 - 30$), correspond to drag dominated cases. For $KC > 100$, the drag coefficients converge to the ones for steady flow.

That being said, Gijón et al. (2021), indicated that dissipation rates remain relatively constant after $KC = 15$. This insight is useful in terms of design as it suggests that increasing KC beyond this threshold, does not lead to significantly greater energy dissipation.

All these observations are relevant for this research because understanding attenuation and thus the hydrodynamic force acted on the elements, can give insights on the behavior of the full AR restoration, which address the third Research sub-Question.

Last but not least, most formulations regarding energy dissipation, use as input the maximum horizontal velocity acting above the reef, assuming it is constant on the vertical. Lowe et al. (2007) proved that this is not the case, and that actually velocity attenuates in the vertical due to interaction of the flow with the canopy. He also concluded that for an irregular wave field, different frequency components, present different attenuation rates with short-period waves presenting less attenuation, since orbital velocities are big enough to penetrate deeper into the canopy compared to long-period waves. As a result more dissipation is expected from short-period waves. Lowe et al. (2007) proposed a new formulation for the wave energy dissipation equation, where this frequency dependent attenuation is included into the f_e parameter.

As in fringing reef environments, longer waves dominate, the complicacy of the frequency dependent dissipation is an important part to keep in mind when examining the influence of the presence of infragravity waves on the reef.

2.2. Stability prediction methods for isolated elements

Depending on the context, many definitions have been given on the term ”stability”. When describing the instability of an object, definitions generally involve the notion of movement or rotation of the object, away from its original state of rest or equilibrium. For an equilibrium to be disturbed and the object to start moving, a certain threshold value is exceeded.

2.2.1. The Morison Method

A straightforward approach to describe instability, is to assume that it occurs once the force or moment acting on an object exceeds its corresponding resisting component. In the example of force equilibrium, which will be the case examined within the scope of this thesis, the mobilizing forces acting on the object, are the hydrodynamic forces. Specifically, only wave forces F_{wave} are taken into account, while current induced forces are neglected. The resisting force is the friction force F_F.

The friction force can be quantified, therefore problem then lies on quantifying the hydrodynamic loading. A popular semi-empirical approach for the wave force was proposed by Morison et al. (1950). Morison expressed the force F_{wave} acting on a cylindrical object, such as a pile, as the sum of two components: a drag force and an inertia force. Their depth integrated values are given by:

$$F_{wave} = F_{drag} + F_{inertia} \tag{2.4}$$

$$F_{drag} = C_d \rho_w A_p \frac{u^2}{2} \tag{2.5}$$

$$F_{inertia} = C_m \rho_w V \alpha \tag{2.6}$$

Where:

C_d	[-]	=	Drag coefficient
ρ_w	[kg/m^3]	=	Water density
A_p	[m^2]	=	Projected cross-sectional area as seen from the direction of the flow
u	[m/s]	=	Horizontal flow velocity
C_m	[-]	=	Inertia coefficient
V	[m^3]	=	Volume of the pile
α	[m/s^2]	=	Water particle acceleration

Morison performed the analysis assuming waves of small amplitudes where Linear Wave theory can be used to describe the velocity and acceleration variations. Therefore, the maximum calculated values of u and α are calculated as shown in equations (2.7) and (2.8). The expected deviations of the velocity and acceleration oscillation from the assumed sinusoidal form, are accounted in the empirical coefficients.

$$u = \frac{\pi H_s}{T} \frac{1}{\sinh kh} \tag{2.7}$$

$$\alpha = \frac{2\pi^2 H_s}{T^2} \frac{1}{\sinh kh} \tag{2.8}$$

Regarding the friction force, it is equal to the multiplication of vertical net force N with the coefficient of friction μ. The coefficient depends on the two materials that are sliding over each other. For concrete, used for the A.R.s, sliding on sand, μ is 0.5. The vertical force N, consists of the weight of the object W_{obj} reduced by the buoyancy $F_{buoyancy}$ and the lift F_{lift} forces.

$$F_F = N\mu \tag{2.9}$$

$$N = W_{obj} - F_{buoyancy} - F_{lift} \tag{2.10}$$

$$F_{friction} = \mu \left(W_{obj} - F_{buoyancy} - F_{lift} \right) \tag{2.11}$$

$$F_{wave} = F_{drag} + F_{inertia} \tag{2.12}$$

The aforementioned forces are given by:

$$F_{buoyancy} = \rho_w V g \tag{2.13}$$

$$F_{Lift} = C_L \rho_w S \frac{u^2}{2} \tag{2.14}$$

Where: C_L [-] = Lift coefficient
S [m^2] = Planform area of the submerged object

Ultimately, a first approach on stability would be to combine the above equations, equate the total wave force with the total resisting force and then solve for the required weight. This calculation results in the minimum required weight [N] needed for a stable pile.

$$W_{req} = \frac{F_{wave}}{\mu} + F_{buoyancy} + F_{lift} = \frac{C_d \rho_w A_p \frac{u^2}{2} + C_m \rho_w V \alpha}{\mu} + \rho_w V g + C_L \rho_w S \frac{u^2}{2} \tag{2.15}$$

$$W_{req} = \frac{F_{wave}}{\mu} + F_{buoyancy} + F_{lift} = W_{req} = \frac{C_d \rho_w A_p \frac{u^2}{2} + C_m \rho_w V \alpha}{\mu} + \rho_w V g + C_L \rho_w S \frac{u^2}{2} \tag{2.16}$$

2.2.1.1. The Force Coefficients

The Morison method is semi-empirical, as the force coefficients used in the equations, namely C_d, C_m and C_L are determined experimentally for each specific case. They are influenced by flow characteristics and the shape and dimensions of the object which the forces are acted on. The most accurate way to define the coefficients, is by measuring the forces acting on the AR unit during the experiments, a procedure that requires the appropriate force measuring instrument. Since such an instrument is not available for the present study, the values of the coefficients will have to be defined based on similar examples and researches found in literature.

Studies and reports examining vertical cylinders, have shown that C_d and C_m can be considered to be a function of the Reynolds number Re, given by equation 2.17, the Keulegan-Carpenter number KC, given by equation 2.3 and the relative roughness Δ, given by equation 2.18 (Det Norske Veritas 2010; Sarpkaya 2010).

$$Re = \frac{UD}{\nu} \tag{2.17}$$

$$\Delta = \frac{k}{D} \tag{2.18}$$

Where: u [m/s] = Total flow velocity
D [m] = Cylinder's diameter
ν [m^2/s] = Kinematic viscosity ($= 10^{-6}$ m^2/s)
k [m] = Roughness height

Accounting first for smooth cylinders, in steady oscillatory flow, Keulegan and Carpenter (1958) found that, for a constant value of KC, the values of C_d and C_m decrease with increasing Reynolds numbers,

while C_m increases with increasing Re. Guidelines presented in the USACE (1984) manual, which compile information from multiple studies, appear to support the above observations. Both Keulegan and Carpenter (1958) and USACE (1984) suggest that a conservative value for C_m for a smooth cylinder is 2. However, Sarpkaya (2010) performed similar experiments where, even though his findings for the C_d coefficient are consistent with the findings of the other authors above, his results concerning the C_m coefficient, suggest an opposite trend, with C_m values increasing with increasing Re numbers. Regardless, all authors agree that for high Reynolds numbers, both C_d and C_m appear to have a constant value independent from the Reynolds number.

Sarpkaya (2010) also performed experiments with cylinders of varying roughness, uniformly roughened, for two values of KC, 20 and 100. Plotting curves where Δ is constant, across varying Reynolds numbers, he concluded that the inclusion of roughness on the surface of the cylinders, results in curves that undergo similar changes compared to a smooth cylinder. However, he found that the values of the force coefficients can be significantly altered. Specifically, for high Reynolds numbers, a rough surface suggests increase of the C_d coefficient, compared to a value corresponding to a smooth cylinder, whereas on the contrary C_m's value decreases. This behavior is reversed for low Re. His results can be found in figures C.3, C.4 and C.5 in the Appendix B.

The lift coefficient represents the lift or transverse forces, and is related to vortex shedding in the wake of the object. Although comparatively fewer studies exist on this particular coefficient, USACE (1984) suggests that a reasonable approximation is to assume C_L to be equal with C_d. This assumption has been supported experimentally for example by observation performed by Tomasicchio, Aristodemo, and Veltri (2009). Sarpkaya (2010) generally further enforces that statement whilst he also suggested that for low Reynolds numbers, below 20000, C_L depends mostly on KC, whereas for higher values of Re, C_L varies as a function of both Re and KC, Additionally he proposed values for C_L for a rough cylinder, where he showed that roughness decreases the value of the coefficient (figure C.5).

2.2.2. The Shields' parameter method

Another method to assess stability, is to use the Shields' parameter. Shields investigated experimentally the threshold of motion for a planar bed consisting of non-cohesive sediment of a circular shape, under a unidirectional stream. He proposed a dimensionless parameter θ as representative of the resulting motion pattern, which he defined as the ratio between the driving forces acting on a sediment particle and the resisting forces opposing its motion. As a representative driving or active force, he selected the bed shear stress, while for the resisting force, he chose the immersed weight of the grain. Motion is expected to occur when the driving forces exceed the resisting forces. The shear stress corresponding to the initiation of motion is referred to as critical shear stress τ_{cr}, and the associated dimensionless number is known as the critical Shields' parameter θ_{cr}. In its original form, the Shields' parameter is given by equation 2.19. If the actual velocity is substituted in equation 2.19, θ acts simply as a mobility parameter.

$$\theta_{cr} = \frac{\text{driving force}}{\text{resisting force}} = \frac{\tau_{cr}}{(\rho_s - \rho_w)gd} \tag{2.19}$$

Where:	θ_{cr}	[-]	=	Critical Shields' parameter
	τ_{cr}	$[kg/m^{-1}/s^2]$	=	Critical shear stress at the bed
	ρ_s	[kg/m^3]	=	Sediment grain density
	ρ_w	[kg/m^3]	=	Water density
	g	$[m/s^2]$	=	Gravitational acceleration (=9.81 m/s^2)
	d	[m]	=	Grain diameter

Including into the formulation the grain Reynolds number, which is defined as $Re_* = \frac{u_{*cr}d}{\nu}$, where u_{*cr} is the critical shear stress velocity $u_{*cr} = (\tau_{cr}/\rho_w)^{1/2}$, equation 2.19 is rewritten as:

$$\theta_{cr} = \frac{u_{*cr}^2}{g\Delta d} \tag{2.20}$$

Where: Δ [-] = Relative density ($= (\rho_s - \rho_w)/\rho_w$)

To further account for the non-spherical shape of sediment grains and the shear stress induced by the oscillatory wave motion instead of unidirectional flow, the final formulation of the Shields' mobility parameter is expressed as:

$$\theta = \frac{\hat{u}_\delta^2}{g\Delta d_n} \tag{2.21}$$

Where: $\hat{u}_\delta$ [m/s] = Peak orbital velocity on top of the boundary layer
d_n [m] = Nominal diameter

Plotting the various critical Shields parameters obtained by the experiments, against the particle Reynolds number, Shields derived what is now known as the Shields curve. This curve provides a criterion for sediment mobility, where the resulting θ values lying above the curve, correspond to unstable conditions and imply movement. The traditional threshold of motion, proposed by the Shields' curve, is derived for a sea or river bed, implying a medium of multiple possibly interacting grains. As such, the threshold of motion is not necessarily a uniquely defined value. In particular, the position of each grain within the bed has to be accounted for, as it influences its exposure and thus its stability, and subsequently motion is not expected to occur simultaneously for all grains. Therefore, the threshold of motion is more appropriately described by a range of values, typically between 0.03 and 0.06, with 0.06 indicating continuous movement in all locations.

Even though the medium on which the formulation is applied on, in the context of this thesis, is not the same as the one used for the derivation of the Shields parameter, a previous study by Diederen (2023) found that using a Shields curve can provide a good representation of the reef. Thus, it would be interesting to test its applicability in the current project, as its dimensionless nature enables up-scaling the conclusions which would be beneficial to following stages of production and design of more AR units of the shame shape.

2.2.3. Empirical Observations on stability

In addition to theoretical analyses, empirical observations from experiments and numerical simulations can be found in literature. These serve to examine the validity of the proposed approaches and give more insight on the behavior of the artificial reefs in question. In the following chapter, the most important findings from relevant papers are summarized.

Miao (2006), Düzbastılar and Şentürk (2009), Diederen (2023), and Harris (2004) give examples of case studies that examine the stability of an artificial reef design, using the Morison approach to quantify the hydrodynamic force acting on the reef element.

Since velocity and acceleration are calculated by linear wave theory, the hydrodynamic force is expected to depend on the wave height, wave period and water depth. As the wave height increases while wave propagate towards the shore and water depth decreases, the hydrodynamic force would increase as well. That increase results in an increase in the required weight, a pattern that is depicted in (Düzbastılar and Şentürk 2009; Diederen 2023; Harris 2004; Miao 2006). Düzbastılar and Şentürk (2009) revealed that the highest force in the cross-shore direction occurs before breaking, a fact consistent with the location where the wave height is maximum. Therefore, it can be summarized that an increase in wave height and decrease in water depth, result in increased weight requirement before wave breaking.

After the waves started breaking, Düzbastılar and Şentürk (2009) and Diederen (2023) presented graphs, that give initial estimations on the required weight for the reef unit. These graphs suggest that installation of the reef on a smaller water depth where the waves have broken, requires a smaller weight compared to prior wave breaking. This is also explicitly mentioned in (Düzbastılar and Şentürk 2009). However, these estimations are calculated using the observed wave height after breaking and accepting all simplifications imposed by the Morison method, that for instance neglect the influence of the turbulence in the water column, imposed by the wave breaking. The validity of these predictions has not yet been verified experimentally, therefore their applicability remains to be determined.

Regarding other wave characteristics, it is found that an increase in wave period, leads to a more unstable reef, while on the contrary, a higher steepness value leads to a more stable case, and thus

a smaller required weight (Diederen 2023). Furthermore as steepness increases, stability becomes more dependent on the water depth. An advantage of using the wave steepness to explore instability, is that it is dimensionless and includes both the wave height and wave period, therefore, more than one wave conditions can be described by the same steepness value and it can thus provide information on the behavior of more than one wave forcing scenarios.

Another factor that influences the results is the relative depth $d_{relative}$, which is given by the ratio of the water depth to the height of the artificial reef restoration $\frac{d}{d_{reef}}$. Diederen (2023) found that the relative depth is linked to wave steepness in its effect on stability, showing a tipping point; for low relative depths, the two parameters are negatively correlated whereas beyond this point, the correlation becomes positive. (Miao 2006) found that the hydrodynamic force is maximum when $d_{relative}$ is equal to one and decreases with a further increase.

Some other factors that were found to affect stability but are not examined in this research, are the bottom slope on which the restoration is placed and the orientation of the artificial reef units in regards to forcing. In particular, an increase in the bottom slope generally leads to a higher required weight (Düzbastılar and Şentürk 2009). Changes in AR's orientation, alter the projected area A_P exposed to flow, which subsequently affects the resulting forces and ultimately the required weight.

2.3. Scaling Laws

Hydraulic experiments, also termed as physical models, replicate conditions and phenomena encountered in nature, typically on a smaller scale. Contrary to real-scale field observations, they allow to recreate and repeat the boundary conditions on demand, while being generally cost-effective. In essence, their goal is to create a physical model that is simulates a physical system, in such a way where the major dominant forces acting on the system are represented in the model in correct proportion to the actual physical system (Hughes 1993). Then, the prototype and the model can be assumed to behave similarly and studying the behavior of the model suffices to understand the behavior of the prototype. Thus, measurements from physical modeling can help assess and validate theoretical models and refine or develop empirical observations.

Before being more specific, certain definitions are introduced (Hughes 1993);

- **Scaling factor** or scale, is the ratio of a given parameter between the prototype and the model; $N_X = \frac{X_p}{X_m}$
- **Similitude Criteria** or scaling laws are mathematical conditions that must be met by the ratios of certain parameters between the model and the prototype and they cannot be altered without changing the underlying physical assumptions.
- **Similarity Conditions** are conditions that exist when a model gives a similar response to the prototype. It is possible to have the model and the prototype being similar, even without meeting all the similitude criteria.
- **Scaling effects** are the differences between the prototype and the model response, that arise from the inability to replicate all relevant forces in the model, at the proper scale.

By definition, similitude is achieved when the ratios of all major factors influencing reactions are in proportion between prototype and model, while the factors that are not in proportion, are so small that are ultimately insignificant for the experiment(Hughes 1993). Then, to obtain completely similar models, all relevant similitude criteria must be met. Moreover, a prerequisite for complete similarity, is complete geometrical similarity (Hughes 1993). Geometrical similarity exists when all ratios of every linear length dimension between model and prototype are constant. Other popular types of similarity are the kinematic and dynamic similarity, with dynamic similarity being prioritized in hydraulic experiments (Frostick, McLelland, and Mercer 2011). Kinematic and dynamic similarity are defined in a similar manner, where they are achieved when the ratios of all vectorial motions or all vectorial forces respectively, are the same for model and prototype for all particles. That being said, full dynamic similarity, which is essential for obtaining reliable results, requires:

$$\frac{(F_i)_p}{(F_i)_m} = \frac{(F_g)_p}{(F_g)_m} = \frac{(F_\mu)_p}{(F_\mu)_m} = \frac{(F_e)_p}{(F_e)_m} = \frac{(F_p)_p}{(F_p)_m} = \frac{(F_s)_p}{(F_s)_m} \tag{2.22}$$

where, F_i is the inertia force, F_g the gravity force, F_μ the fluid friction force, F_e the elastic compression force, F_p the pressure force and F_s the surface tension force.

However, no known fluid is able to satisfy all the force ratio requirements, unless the scaling factor is 1:1 (Hughes 1993). Therefore, the challenge lies in identifying the forces whose influence in the results is insignificant, so that by neglecting them and only scaling the rest, the final model can still behave similarly to the prototype.

Experience has shown that almost all hydraulic experiments, can be simplified to a relationship between two forces. Since inertia forces are always present in flow problems, the question now is which other force will be chosen to balance it.
If gravity is considered the dominant force that balances inertia, then $N_{Fi} = N_{Fg}$ is maintained. The ratio of inertia and gravity forces is also known to give the Froude number Fr as such:

$$\sqrt{\frac{inertia force}{gravity force}} = \sqrt{\frac{\rho L^3 V^2}{\rho L^3 g}} = \frac{V}{\sqrt{gL}} = Fr \tag{2.23}$$

Where: ρ [kg/m^3] = Fluid density
L [m] = Characteristic length dimension
V [m/s] = Characteristic flow velocity
g [m/s^2] = Gravitational acceleration

Then, rewriting $N_{Fi} = N_{Fg}$ gives:

$$N_{Fi} = N_{Fg} \Rightarrow \frac{N_{Fi}}{N_{Fg}} = 1 \Rightarrow N_{Fr^2} = 1 \Rightarrow N_{Fr_p} = N_{Fr_m} \Rightarrow \left(\frac{V}{\sqrt{gL}}\right)_p = \left(\frac{V}{\sqrt{gL}}\right)_m \tag{2.24}$$

where the indexes p and m, refer to the prototype and the model respectively. Incorporating the notion of scale in 2.24, ultimately leads to:

$$N_{Fr} = 1 \Rightarrow \frac{V_p}{V_m} = \sqrt{\left(\frac{g_p}{g_m}\right)\left(\frac{L_p}{L_m}\right)} \Rightarrow \frac{N_V}{\sqrt{N_g N_L}} = 1 \tag{2.25}$$

Equation 2.25 constitutes the Froude model and defines the conditions for achieving Froude scaling. Froude scaling is used for most hydraulic problems involving a free surface. If a similar procedure is followed, where now the force balancing the inertia force is friction or surface tension, the Reynolds and the Weber criteria will be defined.
Reynolds scaling is preferred when viscous forces dominate, for instance when experiments are conducted with laminar boundary layers or forces acted on cylinders with low Reynolds numbers. Weber scaling is chosen when there is an interface between two fluids and the surface tension force on a fluid is significant compared to inertia. (Hughes 1993)

For wave experiments, the relevant forces are gravity, friction and surface tension. Specifically, in the scope of this study, the dominant forces are gravity and inertia; therefore, Froude scaling is considered the appropriate similitude law. Observations have shown that the rest of the similitude criteria do not have to be fully satisfied if certain conditions are followed.
Regarding surface tension, since it usually negligible in the prototype, Weber similitude can be disregarded provided that surface tension in the model is also negligible. This is ensured for the wavelengths of the modeled waves bigger than 2cm, wave periods are bigger than 0.35s and water depths bigger than 0.02m (Frostick, McLelland, and Mercer 2011). Concerning friction, if the Reynolds number in the model is in the same range as the prototype and large enough so that fully turbulent flow conditions are encountered at the reef ($Re_D > 30000$), scaling only the gravity force suffices to give reliable results (Frostick, McLelland, and Mercer 2011). The grain Reynolds number is defined as:

$$Re_d = \frac{\sqrt{gH_s}d_n}{\nu} \tag{2.26}$$

Where: ν [m^2/s] = Kinematic Viscosity (=10^{-6} m^2/s for water)

Once the appropriate scaling law is decided, rearranging the terms in the equation that constitutes the similitude law gives the scaling factors of other parameter such as the velocity or time. For Froude scaling, the one utilized for designing the experiments, the time and velocity scale factors are:

$$\frac{N_V}{\sqrt{N_g N_L}} = 1 \Rightarrow N_V = \sqrt{N_g N_L} \Rightarrow N_V = \sqrt{N_L} \tag{2.27}$$

$$\frac{N_V}{\sqrt{N_g N_L}} = 1 \Rightarrow N_V = \sqrt{N_g N_L} \Rightarrow \frac{N_L}{N_t} = \sqrt{N_L} \Rightarrow N_t = \sqrt{N_L} \tag{2.28}$$

Similar relationships, give formulas to determine the rest of the parameters. The most important ones are summarized on the table bellow:

Parameter	Froude Scaling
Length L	N_L
Area A	N_L^2
Volume V	N_L^3
Time T	$\sqrt{N_L}$
Velocity V	$\sqrt{N_L}$
Acceleration α	1
Mass M	N_L^3
Force F	N_L^3

Table 2.1: Scaling factors for Froude Scaling

3

Research methodology

3.1. Physical Model

Designing a robust experiment is the first step to ensure that the datasets obtained can effectively address the research questions. As the AR design was developed specifically for the CREST project, the experimental conditions in this study largely align with those adopted in CREST.

Consequently, the general outline of the experimental parameters builds upon the framework established in CREST, thus several experimental parameters are already partially defined. A key distinction however, lies in the scale of the experiments, with the present study being conducted in a smaller scale in the Scheldt Flume, rather than the Delta Flume used in CREST. Due to the similarities with the CREST project, the present experiments will be referred to as the ***miniCREST*** experiments.

3.1.1. Scaling

The miniCREST experiments can be considered, to a certain degree, as a scaled down version of the original CREST ones. Consequently, the appropriate scaling law and factor must be defined.

The experiments explore the behavior of free surface gravity waves. As such, Frouede scaling is deemed the appropriate scaling law, provided that the experimental design satisfies the conditions mentioned in Chapter 2, to approximate similarity as closely as possible.

The geometric scaling ratio is usually determined by the largest dimension found in the test facilities. Thus, in general, the dimensions of the laboratory basin or the flume are used to calculate that ratio (Frostick, McLelland, and Mercer 2011). However, for this study, the defining factor was the printer's limitation in accurately replicating the reef on a small scale. After some testing, it was deemed that the smallest reef height that the printer could reproduce while still preserving the main characteristics of the originally proposed CREST design was 4 cm. Then, the length scale factor was defined as the ratio of the height of the reef between the prototype (CREST) and the model (miniCREST):

$$\frac{h_p}{h_m} = \frac{25}{4} \Rightarrow \mathbf{N_L} = 6.25 \tag{3.1}$$

All other length dimensions were scaled down using that ratio. The rest of the variables, such as the element's volume V or the wave period T, where calculated using the scale relations found on table 2.1.

An important observation is the fact that the scaling ratio used throughout the thesis is based on the parameters used in CREST. CREST itself presents a scaled down model of an assumed prototype of a fringing reef environment, using a geometric scaling factor of 3 (Takens 2024). Consequently, scaling between the parameters used in the current thesis and their corresponding values in reality, corresponds to a geometric scaling factor of 18.75.

3.1.2. Experimental set-up

As the experiments' main objective is to explore the AR's stability specifically in a fringing reef environment, the unique morphology characteristic to this reef type must be replicated.

3.1.2.1. Laboratory Facilities

The experiments are conducted in the Western part of the Scheldt Flume in Deltares. The flume has a length of 55 m, width of 1 m and height of 1.2 m (Deltares n.d.).

Within this flume, a concrete foreshore is installed to reproduce the characteristic morphology of a fringing reef and the associated hydrodynamic patterns found. The foreshore has a slope of 1:4.5, a height of 0.8 m and includes a reef flat of total length of 7.28 m. The cross-shore placement of the AR restoration on the reef flat was determined in a previous study performed by Takens (2024), as the location where energy dissipation is expected to be maximum. As such, the first row of the AR restoration is placed 3.44 m from the edge of the reef flat. The total length of the complete reef restoration covers 1.60 m. Downstream the reef restoration, a run-up berm is placed, to simulate the shoreline of the island. It consists of a slope of 1:10 and a height of 0.36 m, measured from the top of the reef flat. All the dimensions mentioned are scaled down values of the set-up that was used during the large-scale CREST experiments and are presented in figure 3.2.

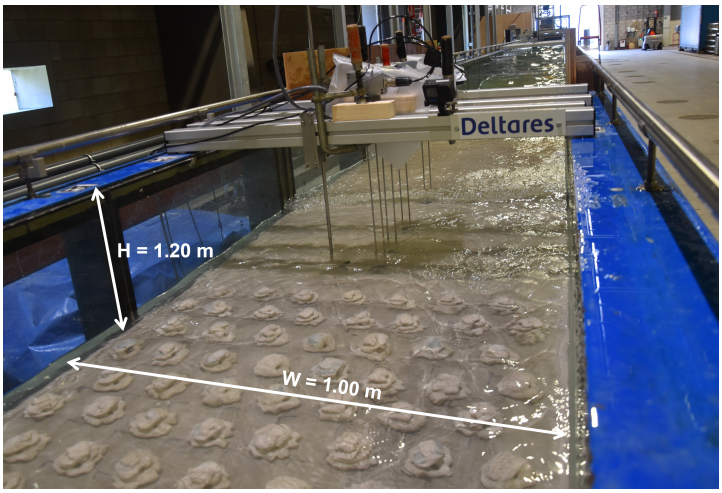

Figure 3.1: Installation of the reef restoration within the flume and dimensions of the flume

3.1.2.2. Instrumentation

During the experiments 12 Wave Gauges (WG) and 2 ElectroMegnetic Flow meters (EMF) are used.

The WGs are arranged in groups of four so that either the Zelt and Skjelbreia method or the Nonlinear modified Eldrup Lykke Andersen method can be applied, to separate the incoming and reflected waves components. Since the primary locations of interest are situated before and after the reef, eight WGs in total are deployed along the reef flat, four upstream and four downstream the reef restoration. The remaining four WGs are placed on the offshore flat section of the flume, seaward of the foreshore at distances 22.37, 23.47, 24.07 and 24.52 m from the wave maker. The two EMFs are placed on the transects where WG8 and WG9 are installed. These locations will be referred to as location A and location B respectively. The precise locations of the WGs and the EMFs, is described in table B.1 in Appendix.

In addition to those, cameras are placed on different locations of the flume, on the top and on the sides, to take videos that capture the movement of the ARs. The data obtained from the instruments described make it possible to identify and document which conditions lead to unstable results, the degree and nature of the observed movement, and ideally, the precise moment at which unit displacement occurs.

A complete summary of the foreshore dimensions mentioned and a top view layout of the flume is presented in figure 3.2.

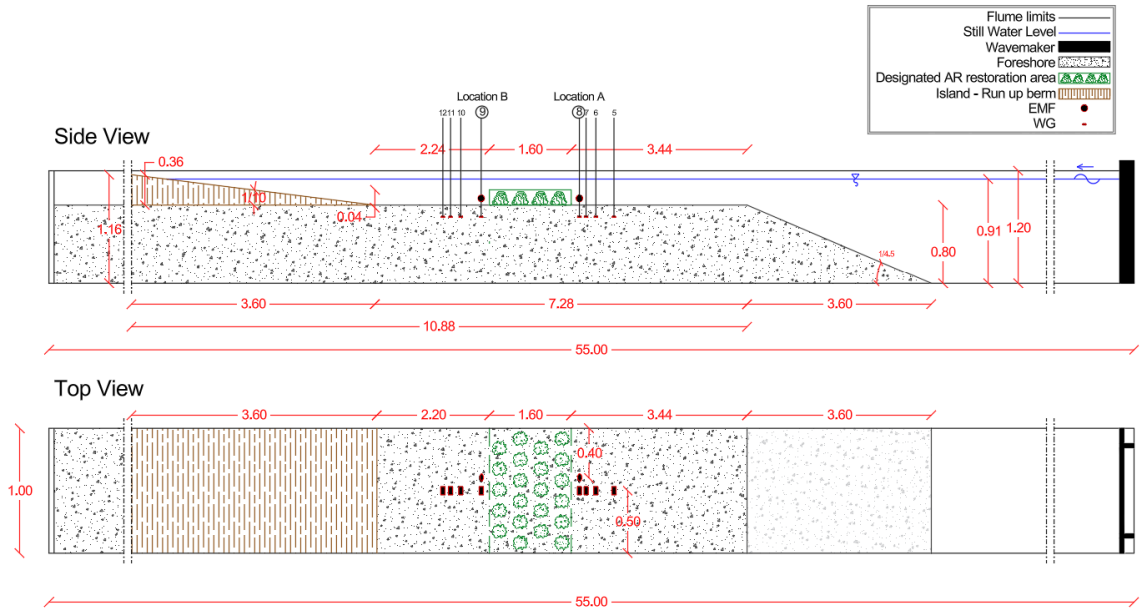

Figure 3.2: Side and Top view of the set-up used in the experiments, for WL11 and the considering the full 4 cm restoration installed on the reef flat

3.1.3. Hydrodynamic Conditions

To complement the replication of fringing reef conditions, the hydrodynamic forcing is selected to reflect wave climates and water levels typical of coral reef islands in the Indian and Pacific Oceans, which represent potential installation locations for the reef restoration.

Low-lying coral reef islands in the Indian Ocean, such as the Maldives, typically experience mild wave conditions and are rarely exposed to storm surges and cyclones. Cases of extreme water levels have been observed in Fiyoaree, but they are the result of distant swell waves with large periods and small wave heights. In contrast, islands in the Pacific ocean are more frequently subjected to extreme wave events caused by cyclones, where short waves with large wave heights are encountered. To facilitate the investigation of the AR's stability in both possible installation locations, both mild swell-dominated and extreme storm-driven scenarios are simulated during the experiments.

3.1.3.1. Wave conditions

The foundation of the wave conditions used stems from realistic wave height and wave period combinations, representative of the areas described, defined within the overall framework of the ARISE project. Consequently, some conditions are directly scaled down from CREST, which provides the advantage to utilize the already available experimental data of surface elevation and wave height for preliminary calculations to verify the feasibility of the proposed condition. These include conditions C3, C9 and C11. C3 represents the mild wave climate found in the Indian Ocean and C9 and C11 account for storms in the Pacific.

Two extra conditions were created to increase the range of the given conditions; C0: as a more mild alternative of C3 and C11*: a more extreme alternative of C11. Regarding the definition of a more extreme condition, opting for a higher wave height instead of period was not feasible due to the wavemaker's limitations. Therefore, the more unstable condition was obtained by increasing the wave period of the given most energetic condition.

The experiments are performed for both irregular and regular waves. The regular wave cases are designed such that for each irregular wave condition, a corresponding regular wave is defined with equivalent incoming offshore wave energy. Testing with irregular waves provides more realistic representation of natural conditions, while including regular waves enables comparisons to be made. Specifically, with the appropriate analysis, comparing cases with the same offshore energy, can possibly provide insights

on whether the expected energy repartition that occurs for an irregular wave spectrum, near the reef, towards different frequencies, presents significantly different results in terms of stability. Based on these considerations, the final wave conditions are the following:

Condition	**miniCREST Model**		**Prototype**	
	Significant wave height [m]	Peak Period [s]	Significant wave height [m]	Peak Period [s]
C0	0.04	3.70	0.75	16
C3	0.08	3.70	1.50	16
C9	0.16	3.00	3.00	13
C11	0.21	2.31	4.00	10
C11*	0.21	3.00	4.00	13

Table 3.1: Incoming wave conditions for irregular waves

Condition	Wave height [m]	Period [s]
R0	0.03	3.70
R3	0.06	3.70
R9	0.11	3.00
R11	0.15	2.31

Table 3.2: Incoming wave conditions for regular waves

3.1.3.2. Water level

In terms of the water depths used, two still water levels are defined, measured in front of the wave maker as 0.91 m and 0.85 m. These values are scaled representations of the corresponding depths used in the CREST experiments, 5.67m and 5.33m, which in turn represent prototype water levels of 1 and 2 meters. Since the foreshore's slope height is 0.80m, the still water level on the reef flat will be 0.05 m and 0.11 m, thus the naming convention for each water level as WL05 and WL11.

The range of the explored water depths is proposed by the ARISE project and represents the expected range of the water levels that is expected to be encountered on fringing reef environments, accounting for the additional limitation that the reef should ideally be submerged at all times. This limitation defined the smallest allowed water level, which, offshore, corresponds to 0.85 m.

Condition	Still water depth offshore [m]	Still Water depth [m]
WL05	0.85	0.05
WL11	0.91	0.11

Table 3.3: Design water depths defined offshore in front of the wave maker and on the reef flat

3.1.3.3. Duration of the runs

The minimum duration of the irregular wave experiment is chosen such that reliable results are ensured. The largest peak period within the defined wave conditions, dictated by conditions C0 and C3 being T_p of 3.70 sec, results to the maximum peak frequency f_p observed, equal to 0.27 Hz. A spectral resolution of $\delta f = \frac{f_p}{20} = 0.0135Hz$ was used, and considering that $\delta f = \frac{f_p}{20} = \frac{1}{D_block}$, the minimum duration of the block is $D_{block} = \frac{1}{\delta f} = 74sec.$ Using 20 blocks, the minimum duration for a reliable time series would then be 25 min. Assuming spin-up time of 2 minutes, the total required duration of the run is 27 minutes. The duration time will be the same for all the irregular wave conditions. Given that the rest of the conditions have smaller peak periods, the minimum duration that each one would require would be smaller than the one derive described above. Thus, using the same value for all is

conservative. For regular wave conditions, a minimum duration where 100 waves would be generated was assumed. Adding the spin-up time, and considering the least favorable condition, resulted in a total duration of the runs of 8 minutes.

3.1.4. Artificial Reef Structures and Configurations

During the experiments, the stability of only one artificial reef element design is investigated, which corresponds to the geometry used in the CREST experiments. Accordingly, all the AR elements placed on the flume share the same geometry as the CREST units and differ only in scale. Two different sizes are considered, which will be hereafter identified by their input design heights being 4 cm and 5 cm, figure 3.3.

The choice to include an extra reef height served to assess whether elements of different sizes exhibit different behavior. From the two stability methods for isolated elements presented, the Shields' method suggests that larger objects are more prone to instability (equation 2.21). In contrast, the Morison formulation yields less straightforward predictions: increasing object dimensions results in larger input geometric parameters, but it simultaneously modifies the associated force coefficients. As a result, the overall stability response becomes more complex and difficult to predict. Thus, subjecting elements of different sizes to identical forcing conditions can provide useful observations on the influence of size on stability patterns.

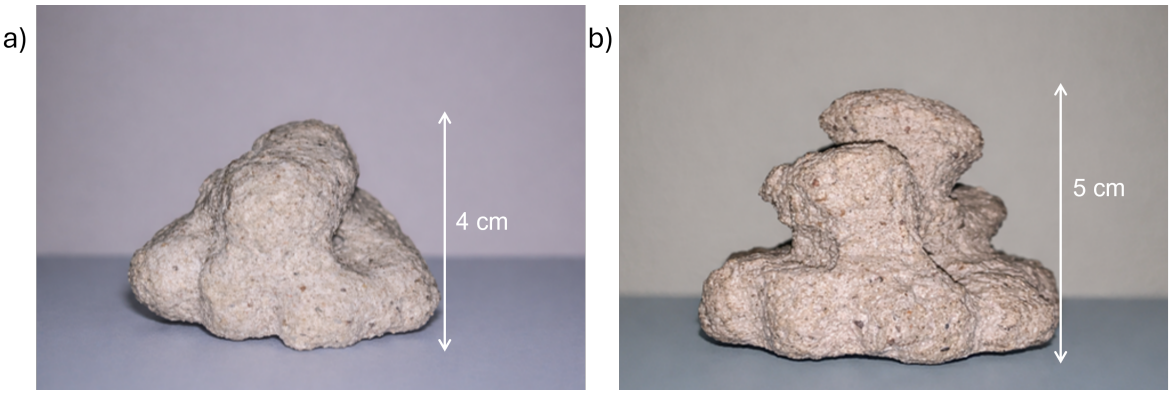

Figure 3.3: AR units used in the miniCREST experiments, a) 4 cm AR, b) 5 cm AR

As shown in figure 3.3, although theoretically identical, the geometry of the 4 cm reef is less detailed and thus differs in practice from the 5 cm one. Furthermore, comparison of figures 1.2 and 3.3 indicates that the final dimensions and shape of the small scale ARs, do not fully replicate the original geometry of the CREST element. The discrepancies observed are attributed to the printing process.

3.1.4.1. Printing process

The required AR units were fabricated using the 3D-printer developed by Coastruction. The printer uses an .stl file as input, which contains all the important information regarding the element's 3D geometry. The two sizes used, originate from the .stl file designed for the CREST project, scaled down accordingly to match the desired heights needed. This approach ensures that from a design point of view, the elements would have the same shape, differing only in scale. Once the input file is prepared, the printer builds the design with the cement mixture provided, using powder bed technology.

Figure 3.4: 3D printing process of the miniCREST ARs in progress

When the printing process is complete, the units remain buried within the excess cement powder and need to be cleaned manually. The cleaning involves excavating the elements out of the printing tray and carefully removing any residual cement from their surfaces. As a final step, the printed elements are cured with water to improve their structural integrity and also gain their final mechanical strength.

Figure 3.5: Different stages of the cleaning process: a) excavation of the elements from tray, b) removal of excess cement material, c) curing with water

Largely due to the small scale of the printed items, the implementation of this procedure in practice led to complications that resulted in the structural variability presented among the AR units. The first complication arises from the printer's ability to accurately reproduce the intricate geometric details imported from the .stl file; although the printer is designed in a way that allows it to produce complex shapes, it is mainly optimized for larger scale applications. Therefore its ability to recreate the small features required to perfectly scale down the CREST design is limited and deviations between the imported and the printed geometry arise. The second complication concerns the manual cleaning of the elements, where mainly due to human error, further inconsistencies occurred in the final shape of the elements.

The combination of the above factors resulted to structural variability, not only between the geometry of the original CREST AR units and the miniCREST ones, but also among units of identical input design height. For simplicity, the intra-structure variability is neglected and it is assumed that each reef size can be characterized by one randomly selected AR, whose weight and overall dimensions are considered to be close to the average ones found when comparing all the units. To ensure accurate results, the actual dimensions of the selected elements are recalculated and used in the analyses, instead of the design values.

The selected ARs of input heights of 4 and 5 cm respectively, have a measured height of 4.12 cm and 5.75 cm. The characteristic dimension for each size is defined as the diameter of the volumetric equiv-

alent cylinder and is equal to 0.054 m and 0.059 m for the 4 cm and the 5 cm height reefs respectively. This definition was selected over the one of a volumetric equivalent sphere because many of the theoretical formulations employed in the analysis have been developed assuming a cylindrical geometry. Therefore, when adjusting these formulations to objects with complex shapes, it is more appropriate to retain the same fundamental reference geometry, the cylinder. Their measured cross-sectional areas as seen from the direction of the flow, A_p, as well as their planform areas S and volumes V can be found in the table below.

The above dimensions correspond to printed weights of 0.145 kg and 0.267 kg for the 4 cm and 5 cm AR unit respectively. The weight values are of considerable importance, as they constitute the threshold of motion, where if the required weight calculated is larger, then movement is expected.

Input height	$d_{meas}[cm]$	$d_n[m]$	A_p $[m^2]$	S $[m^2]$	V $[m^3]$	$W_{printed}[kg]$
4 cm	4.12	0.048	0.0014	0.0032	7.60 $\times 10^{-5}$	0.145
5 cm	5.75	0.058	0.0030	0.0041	0.000152	0.267

Table 3.4: Actual measured characteristics of the elements selected for the 2-elements phase

3.1.4.2. Artificial Reef Configurations

Regarding the placement of the printed AR on the reef flat, the following three configurations are identified:

No reef elements placed on the reef flat: to create a base dataset for each wave condition. A comparison between the measured time series and those obtained from experiments with ARs present on the reef, allows to identify the influence of the reef on the flow.

2 elements placed on the reef flat: one of each size, with the 4 cm one being on the upper part of the transect, as shown in figure 3.6. The elements chosen for these experiments are the ones whose dimensions were measured to define the geometrical characteristics of each reef size. They are consistently used for all the experiments of the "2-elements" configurations and are placed on the location where the first row of the complete reef would be, considering that the first row of the restoration is the one that encounters the biggest amount of energy. Although, two ARs are present in the same transect on the flume, each one is assumed hydraulically isolated and therefore conclusions can be drawn on how the proposed design of the reef elements responds in terms of stability without initially considering the influence of neighboring elements. To safely characterize the elements isolated, implying that there is no flow interference between them and that any lateral disturbance, if present, is be negligible, they are placed 28 cm apart, a distance that corresponds to 3.5 times of the approximate base dimension (8 cm) of the biggest one of the two. This is chosen as the interaction effects between piles placed in the same transect, on an arrangement perpendicular to flow, becomes negligible if $S_G/D = 3$, where S_G is the gap between the surfaces of two neighboring piles in a pile group and D the pile diameter (Bonakdar and Oumeraci 2015).

Full reef restoration present on the reef flat: the complete reef restoration will be tested separately for each reef height. Comparing those results with the ones from the 2 elements experiments, allows the added complexity of inter-element interactions

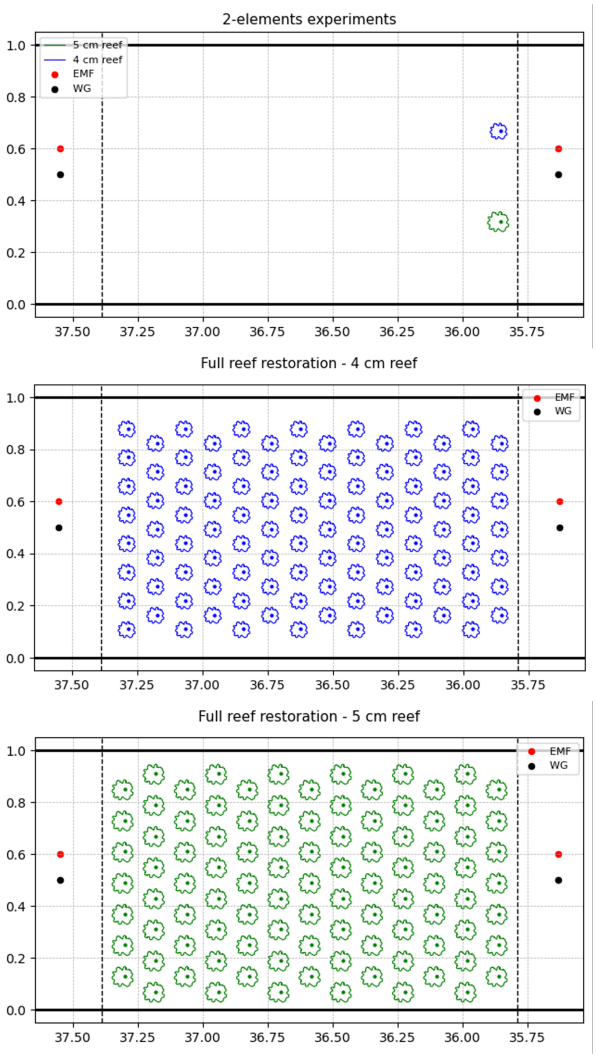

Figure 3.6: Presentation of the different AR configurations utilized during the experiments

between the units to be roughly quantified, thus the effect of the reef's presence on the stability of individual elements can be isolated and evaluated.

Concerning the stability of the complete reef restoration, only one configuration will be tested. During the large scale CREST experiments, two configurations were modeled on the Delta Flume. The choice of which configuration to select for the current experiments was between the aforementioned two and ultimately the low density one was chosen. This decision was made to minimize the total number of elements required per reef configuration, and consequently reduce the construction costs for Coastruction, given that two different reef heights are used during the experiments.

The design characteristics of the configuration itself are the same for both reef heights. The chosen configuration consists of a staggered grid, which, as compared to an aligned arrangement, provides higher dissipation rates (Gijón et al. 2021). The lateral and vertical spacing between the elements, as defined in CREST, are kept the same as in the original configuration, scaled down. As a result S_y and S_x for both reefs heights were 0.067 m. Keeping the same lateral distance for the 5 cm reef as well, where the elements' dimensions are larger, implies that reef density is larger compared to the 4 cm reef.
Since scaling was performed based on the ratio of the reef heights and because the Delta and the Scheldt Flumes have disproportionate dimensions, one extra element was needed per row to maintain the reef density proposed in CREST. Consequently, the 4 cm height reef consisted of 14 rows with 7 or 8 elements per row, leading to 105 elements in total. For the 5 cm reef, 13 rows where used, with 98 elements in total.

Accounting for all the experimental parameters described above, a complete description of the experiments conducted can be found in table B.2 in the Appendix. Regarding the naming convention, summarized as WaveType**XX**WL**Y**Y_Conf can be explained as follows:

- **WaveType**: C or R, identifies the wave type where Irregular:C, or Regular:R
- **XX**: 0, 3, 9, 11, 11*, identifies the wave climate, as defined in tables 3.1 and 3.2
- **WLYY**: 05 or 11, identifies the water level on the reef flat, as defined in 3.3
- **Conf**: ' ', _R*****, FR4 or FR5, identifies the configuration where ":base condition, _R: 2 element experiments, FR 4 or FR5: Full reef restoration of 4 cm or 5 cm

*= Refers to condition C11*WL05_R_Op, which is a special case with wave conditions identical to that of C11*WL05_R and the only difference being the placement of the selected two elements on the reef flat, which is now **Op**posite than indicated in figure 3.6 (for a visual representation see figure 6.2).

3.2. Data Analysis

3.2.1. Preliminary processing

Instrument offset and spin-up time.

It is common that the instruments may capture a non-zero electrical signal during still water conditions, where no oscillations are expected. This introduces an offset to the measured time signals that has no physical meaning and therefore must be removed.

To resolve that, for every run, 30 seconds are assigned in the beginning of each time series , where the wave maker has not yet started but the instruments are already recording. During that interval the offset of each instrument (if any) is captured. The mean value over these 30 seconds is calculated and subtracted from the entire signal for all the cases. Additionally, two minutes are included after the start of the wave maker to account for the spin-up time that the system requires to dissipate the transient effects imposed by the initial conditions. This also includes the time that is required for the first wave to reach the reef flat. Consequently, the first 2.5 minutes of each signal are removed for all of the conditions.

Low Pass Filter

Since the maximum measured velocity u_{max} will be used in the analyses, any spurious high-frequency spikes must be removed from the signals so that the peak velocities used, correspond to physically meaningful wave measurements, rather than noise in the signal. Therefore, a low pass filter is applied. The low-pass filter suggests defining a cut-off frequency f_c, where only wave components with a frequency lower than the cut-off are allowed in the final signal. The implementation of such a method smooths the resulting signal and removes oscillations of a high frequency that have no physical meaning.

In the current study a Butterworth with an order of 4 is used, while the cut-off frequency was chosen to be at 2 Hz. The choice of that limit stems from the fact that looking at the different spectra, for all of the conditions, there appears to be almost no energy after that point. An example of this is presented for case C11WL05 in figure C.1, which can be found in Appendix B. An additional concern regarding the choice of the cut-off frequency, is that fact that a wave with with a frequency equal to 2 Hz would have a period of 0.5 sec, which is unrealistically small. As a result, if such a wave exists in the signal, it is probably generated numerically rather than physically and therefore it should be removed.

3.2.2. Separation of Incoming and Reflected waves

Due to the reef's steep slope, significant wave reflection is expected. To separate the incoming and reflected components from the total measured signals, the method proposed by Buckley et al. (2016) is applied. Their approach utilizes collocated measurements of surface elevation and point velocity in the frequency domain, assuming Linear Wave Theory to be valid.

The method is based on the widely adopted assumption in wave-separation theories, that the total measured signal can be expressed as is a linear superposition of the incoming "+" and reflected "-"components. Formulated in the frequency domain and denoting the Fourier components of surface elevation by F_η and F_u respectively, this assumption is expressed mathematically as follows:

$$F_\eta = F_\eta^+ + F_\eta^- \tag{3.2a}$$

$$F_u = F_u^+ + F_u^- \tag{3.2b}$$

The point velocity signal is related to the surface elevation one through Linear Wave Theory by:

$$F_u^+ = \frac{kg}{2\pi f} K_u F_\eta^+ \tag{3.3a}$$

$$F_u^- = -\frac{kg}{2\pi f} K_u F_\eta^- \tag{3.3b}$$

Where:

$$K_u = \frac{\cosh\left(kh_u\right)}{\cosh\left(k\left(h_0 + \overline{\eta}\right)\right)} \tag{3.4}$$

An analytic derivation of equations A.10 can be found in A.1 in Appendix A.
The system of equations 3.2a, 3.2b and 3.3a, 3.3b has four equations and four unknowns, where its solution provides the formulations for the incoming and reflected components as such:

$$F_\eta^+ = \frac{1}{2}\left(F_\eta + \frac{2\pi f}{gkK_u} F_u\right) \tag{3.5a}$$

$$F_\eta^- = \frac{1}{2}\left(F_\eta - \frac{2\pi f}{gkK_u} F_u\right) \tag{3.5b}$$

Equations 3.5a and 3.5b are a function of the wave number k, which is derived from the dispersion equation:

$$\omega^2 = gk \tanh kh \tag{3.6}$$

The calculation of the wave number is performed separately for each wave harmonic in the frequency domain, as described in A.2. Performing the inverse Fourier Transform on equations 3.5a and 3.5b, the final time series of the incoming and reflected components of the surface elevation and velocity are obtained.

As the proposed decomposition method requires collocated measurements of surface elevation and velocity, the incoming and reflected components can only be calculated on locations A and B. After the decomposition, for each wave condition and location, the following time series are obtained: $\eta_8, \eta_{8,inc}, \eta_{8,ref}, u_8, u_{8,inc}, u_{8,ref}$

3.2.3. Acceleration time series

The Morison equation will be tested with velocity and acceleration inputs derived from both Linear Wave Theory and the actual measured time series . As the acceleration time series are not given, they are obtained by differentiating the velocity signal, a method which was also used by Gijón Mancheño (2016).

The horizontal acceleration α_x is related to the horizontal velocity u_x by $\alpha = \frac{\partial u}{\partial t}$. The differentiation is performed in the frequency domain through a Fourier transformation in order to avoid using a numerical formulation that could amplify noise in the signal. As a result, the velocity derivative is reformed as such:

$$\alpha_x(t) = \frac{\partial u(t)}{\partial t} \overset{\mathcal{F}}{\Longrightarrow} \alpha_x(\omega) = i\omega u_x(\omega) \implies \alpha_x(\omega) = 2\pi f i u_x(\omega) \tag{3.7}$$

An important consideration, is that the Fourier Transformation assumes the signal to be periodic. Therefore, if in practice the first and last points of the signal are not equal, an artificial discontinuity will be introduced at the boundaries which will create high frequency wiggles and spikes that are not representative of the governing physics. To avoid that before the the Fourier transformation is applied, the signal is mirrored both at its beginning and its end.

Since acceleration is directly proportional to frequency in the spectra domain as seen by equation 3.7, a low pass filter is applied in the transformation procedure to prevent an unnatural amplification of the high frequency components. The cut-off frequency is set to 2 Hz, for the same reasons explained in sub-section 3.2.1. For the same reason, the high frequency components (the sea-swell waves), are expected to have larger acceleration values, compared to the infragravity waves.

3.2.4. Infragravity and Sea-Swell waves

When classifying ocean waves based on their length, represented by their period, several categories can be distinguished, illustrated in figure 3.7.

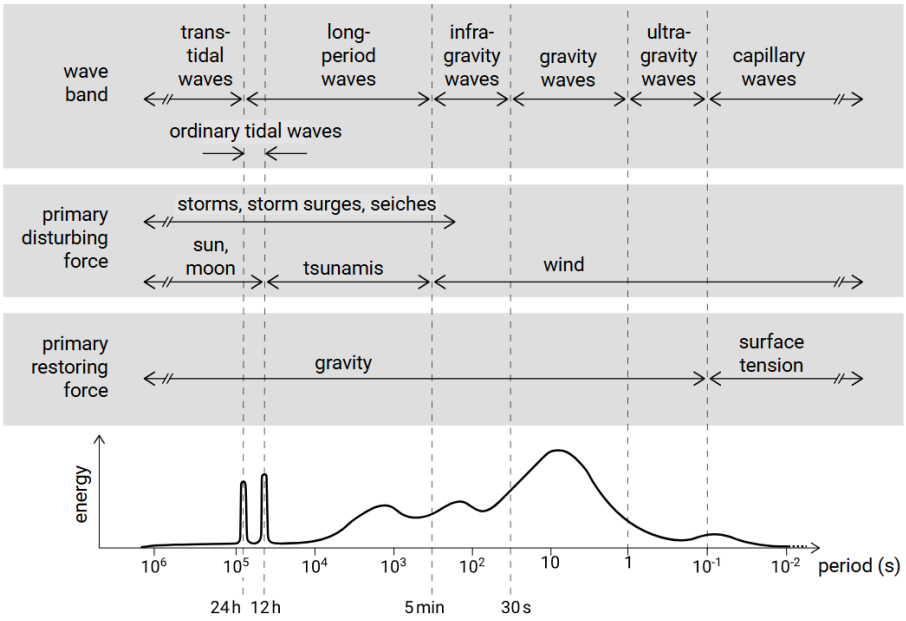

Figure 3.7: Classification of waves based on their length, the disturbing force and the restoring force. Figure taken from (Bosboom and Stive 2023)

For simplicity, in this report, the categorization is limited to two groups, short and long waves. Expressed in terms of frequency, the threshold for the classification is defined such that harmonics oscillating with a larger frequency are characterized as short Sea-Swell waves (SS), while components oscillating with a lower frequency are considered long waves and are referred to as infragravity waves (IG). The threshold frequency bellow which IG occur will be named f_{IG} and is assumed to be equal to half the offshore peak period f_p/2 of each wave climate. The frequency bands for the wave conditions explored are presented in table 3.5

Condition	T_p [s]	f_p offshore [Hz]	f_{IG} [Hz]
C0	3.70	0.270	0.135
C3	3.70	0.270	0.135
C9	3.00	0.333	0.167
C11	2.31	0.433	0.216
C11*	3.00	0.333	0.167

Table 3.5: Peak frequency and infragravity wave limit frequency f_{IG} for all the explored irregular wave conditions

It is possible to isolate the short and long waves in the signal by applying a frequency filter pass, using f_{IG} as the cut-off frequency. This filtering procedure can be applied to all the obtained time series mentioned so far, therefore to both the total and incoming or reflected components of surface elevation and velocity, as well as the computed acceleration time series . As a result, the relevant wave parameters can be calculated separately for the sea swell and infragravity frequency bands, which allows an initial assessment of their contribution in shaping the wave climate on the reef.

A separation between the IG and SS components is only meaningful for irregular wave cases, where more than one frequency components are present in the spectrum.

3.2.5. Definition of representative wave parameters

After obtaining the relevant time series , the wave parameters required in the stability analyses, can be calculated either from the time series itself, or their corresponding variance density spectra. As

discussed in Chapter 2, for both irregular and regular waves, the key variables that must be identified for the stability analyses are:

- **a representative wave velocity**, used directly in the Keulegan Carpenter number, Reynolds number, Shields and Morison Methods
- **a representative wave acceleration**, used directly in the Morison Method

As characteristic values, mainly the maximum values are considered. These can either be obtained directly from the measured time series or they can be calculated using equations 2.7 and 2.8.

The measured maxima u_{max} and α_{max} are defined as the peak values extracted from each the velocity or acceleration time series, for both regular and irregular wave conditions.

For the calculation of the maximum estimated velocity u_{est} and acceleration α_{est} using equations 2.7 and 2.8, the wave height and wave period of an equivalent monochromatic wave, representative of the sea state, are required. The depth term is substituted by the mean depth d_{mean} found on the reef flat, specifically at the location A. It is defined as the measured initial SWL imposed by each condition, increased by the mean set-up. In the case of regular waves, which are inherently monochromatic, the definition of a representative wave height and wave period is straightforward, with the wave height H defined as the amplitude of the oscillation of the surface elevation signal and the period T, defined as the period of that oscillatory motion. In contrast, irregular waves consist of multiple harmonics, making the definition of a representative wave height and period less direct. For the present study, as well as in other cases found in literature such as Düzbastılar and Şentürk (2009) and Diederen (2023), the spectral wave height obtained using equation 3.8 is used as a characteristic wave height for the irregular waves.

$$H_{m0} = 4\sqrt{m_{0_{\eta\eta}}} \tag{3.8}$$

Where: H_{m0} [m] = Spectral Wave height
$m_{0_{\eta\eta}}$ [m^2] = Zeroth spectral moment of spectra $S_{\eta\eta}$

The represented irregular wave period is substituted by the mean spectral period $T_{m_{-1,0}}$, defined by equation 3.9. The use of the mean spectral period in the analysis over T_p is selected to account for the influence of low frequency components in the wave spectrum. More specifically, this formulation assigns greater weight to lower frequencies in the calculation of the representative wave period, thereby capturing more effectively the low frequency waves.

$$T_{m_{-1,0}} = \frac{m_{-1_{\eta\eta}}}{m_{0_{\eta\eta}}} \tag{3.9}$$

Where: $T_{m_{-1,0}}$ [s] = Mean Spectral Wave period
$m_{-1_{\eta\eta}}$ [m^{2}Hz^{-1}] = Negative first spectral moment of spectra $S_{\eta\eta}$

The spectral moments moments found in equations 3.8 and 3.9 can be calculated using the general definition the n^{th} order spectral moment m_n of a spectrum E, which is given by:

$$m_n = \int_0^\infty f^n E(f) df \quad \text{for} \quad n = ... -1, 0, 1, 2, ... \tag{3.10}$$

Provided that the corresponding time series are available, the above definitions can be applied to calculate the wave characteristics of all wave components defined above, including the total, incoming, and reflected waves, as well as their decomposition into sea-swell, infragravity, or full frequency bands (FF), and any combination thereof. For example, if the surface elevation of the incoming infragravity waves is considered, then the spectral wave height $H_{m0_{inc,IG}}$ can be calculated for the respective variance density spectra $S_{\eta\eta_{inc,IG}}$. With all the respective variables defined, u_{est} and α_{est} are calculated by combining the correct input parameters. Namely, following the previous example, $u_{est_{inc,IG}}$ is calculated using d_{mean}, $H_{m0_{inc,IG}}$ and $T_{m_{-1,0_{inc,IG}}}$.

The above variables suffice to calculate the maximum values of velocity and acceleration used in the Morison Method. However, for the Shields Method, since the definition of the wave parameters for irregular waves is complicated, one extra parameter was explored, the root mean square velocity u_{rms}. The root mean square velocity can be calculated by the zeroth spectral moment of the velocity variance density spectra S_{uu} as such:

$$u_{rms} = \sqrt{m_{0_{uu}}} \tag{3.11}$$

Where: $m_{0_{uu}}$ [[m^{2}Hz^2]] = Zeroth spectral moment of the velocity variance density spectra

4

Hydrodynamic Forcing at the Reef flat

As waves propagate from offshore towards the reef flat, the natural increase of the seabed, combined with the hydrodynamic processes characteristic of a fringing reef environment, significantly influence the transformation of the offshore forcing and the energy reaching the reef flat. Furthermore, since the stability of a structure is dependent on the hydrodynamic forcing it experiences, it is directly governed by the nearshore values of certain key wave variables. Therefore, understanding the dominant processes found on a fringing reef and their role in transforming the offshore wave climate, especially in shaping the values of the key variables that govern stability, is essential for identifying and interpreting emerging stability patterns.

The identification of which are the key variables depends on the approach adopted to describe the instability. Specifically, when the Shields' number is employed, stability is primarily related to the near bed flow velocity found on the reef, while the Morison method relates stability to both wave velocity and acceleration. Nevertheless, even though both approaches have velocity in common as a key variable, with the Shields number, the measured velocity is usually preferred, whereas in the Morison Method, the velocity and acceleration inputs are traditionally is estimated using equation 2.7. Since both estimated and measured velocities will be explored in terms of how effectively they can describe instability based on the proposed formulations, two sets of parameters are identified to influence instability: the values of wave height H, wave period T and water depth d, that are used as inputs in equations 2.7 and 2.8 to estimate u and α, and the directly measured values of u and α.

4.1. Dominant hydrodynamic processes on a fringing reef

The unique morphology of a fringing reef environment, particularly the steep reef slope in front of the flat, imposes sudden and concentrated wave breaking as well as reflection, leading to energy dissipation and partial reflection of wave energy offshore. Additionally, nonlinear wave interactions combined with the moving break point forcing, amplify the energy of long wave components within the wave spectrum found on the reef flat (Pequignet et al. 2009). In this section, the influence of wave breaking and reflection in transforming the offshore wave climate are examined.

4.1.1. Wave breaking

As shown in tables 4.1 and 4.2, wave breaking becomes progressively more intense under more energetic conditions, shown from the fact that higher offshore wave heights, present a larger reduction. Furthermore, the smaller available depth imposed by WL05, results in higher attenuation rates between conditions with the same offshore wave height. For instance the attenuation rate is 69% for C11WL05, compared to 65% for C11WL11, resulting in a larger wave height on the reef under WL11. Regardless of the resulted attenuation rate, most of the wave heights that ultimately reach the reef flat, remain confined within a narrow range. For example, for irregular waves, the offshore wave height variation of 17 cm between the most and the least energetic cases is reduced, after breaking, to a 7 cm difference. This indicates that due to depth limited breaking, imposed by the reef's steep slope, increases in the offshore wave height do not translate into proportional increases in wave height on the reef flat.

In addition to governing wave height attenuation, the intensity of wave breaking is related to the mean water depth found on the reef. The mean water level d_{mean} for each wave condition is determined by the still water level d_0, increased by the set up η. As the d_0 is constant, the different mean water depth values between cases with the same initial depth, are dictated by the mean wave induced set up η. Tables 4.1 and 4.2 indicate that between runs with identical offshore wave conditions, larger set up values are observed for WL05 than WL11. This is consistent with the more intense wave breaking occurring on the reef, as set up is driven by changes in the cross-shore radiation stress resulting from wave energy dissipation. Similarly, more energetic conditions present higher set up than lower energy ones, which can be seen for instance when comparing the set up from C11 (0.054 m for WL05) to C0 (0.017 m for WL11).

Regardless of the relative increase in water level due to wave breaking, the initially higher still water level in WL11, results in a greater mean water depth in the cases considered, when compared to conditions with the same offshore wave height. This occurs even though wave set up is larger for the low water level condition. Since the resulting wave heights are depth limited, the greater water level in WL11 contributes to the higher wave heights observed, compared to WL05.

Table 4.1: Input significant wave height, spectral wave height and wave induced set up elevation at location A, for **irregular waves**

Condition	H_s Input [m]	H_{m0} [m]	η_8 [m]
C0WL05	0.040	0.035	0.017
C3WL05	0.080	0.060	0.017
C9WL05	0.160	0.087	0.040
C11WL05	0.210	0.087	0.047
C11*WL05	0.210	0.106	0.054
C0WL11	0.040	0.053	0.000
C3WL11	0.080	0.071	0.017
C9WL11	0.160	0.093	0.077
C11WL11	0.210	0.093	0.025

Table 4.2: Input wave height, wave height and wave induced set up at location A for **regular waves**

Condition	H Input [m]	H [m]	η_8 [m]
R3WL05	0.057	0.040	0.021
R9WL05	0.113	0.057	0.046
R11WL05	0.147	0.051	0.056
R3WL11	0.057	0.072	0.005
R9WL11	0.113	0.051	0.024
R11WL11	0.147	0.053	0.034

Wave breaking on the reef's slope, not only results in loss of energy through turbulence, but also contributes to long wave generation. To examine energy loss and redistribution across the reef profile, the variance density spectra of the surface elevation $S_{\eta\eta}$ are analyzed. This approach allows the observation of the local energy, as multiplication of $S_{\eta\eta}$ by ρg yields the wave energy spectrum. Accordingly, the plots of the surface elevation spectra referring to the total waves found on the flat are created, presented in figure 4.1. Figure 4.1 shows a reduction in the total spectral energy at locations A and B, compared to the offshore one, validating the loss of energy implied by table 4.1 as the waves propagate nearshore.

Regarding energy redistribution and infragravity wave generation associated with the moving break point, although it is difficult to isolate their individual contribution in shaping the total signal, the combined effect of these phenomena is also depicted in figure 4.1, as energy is transferred towards the lower frequencies.

Especially for WL05 cases, most of the energy found around the previously dominant peak frequencies f_p for each wave condition appears to have either been dissipated or transferred towards the IG frequency band. Consequently, in the majority of the cases, most of the wave energy is concentrated towards the low frequencies, which already suggests that infragravity waves dominate over the reef flat. For WL11, the situation is similar as in WL05, with the presence of IG waves still enhanced, notwithstanding to a lesser extent, especially for the low energy conditions. Although clear peaks are present at low frequencies as shown in figure 4.1, the dominance of the sea swell waves in the wave spectrum is maintained on the reef flat. The most notable difference and the most relevant observation in terms of the stability analysis for WL11, is the fact that in contrast to WL05 where there is mainly only one

peak in the spectrum, now a distinct secondary peak is present. The existence of two peaks, one in each frequency band, indicates that both the infragravity and sea swell waves contribute significantly in shaping the overall wave signal.

The redistribution of energy among different frequency bands, especially when it leads to a bimodal spectrum, raises the question of which definition of wave parameters most appropriately represents the wave field on the locations of interest. This is particularly important as these parameters are used as inputs to the formulations of Morison and Shields and therefore dictate the effectiveness of the proposed methods.

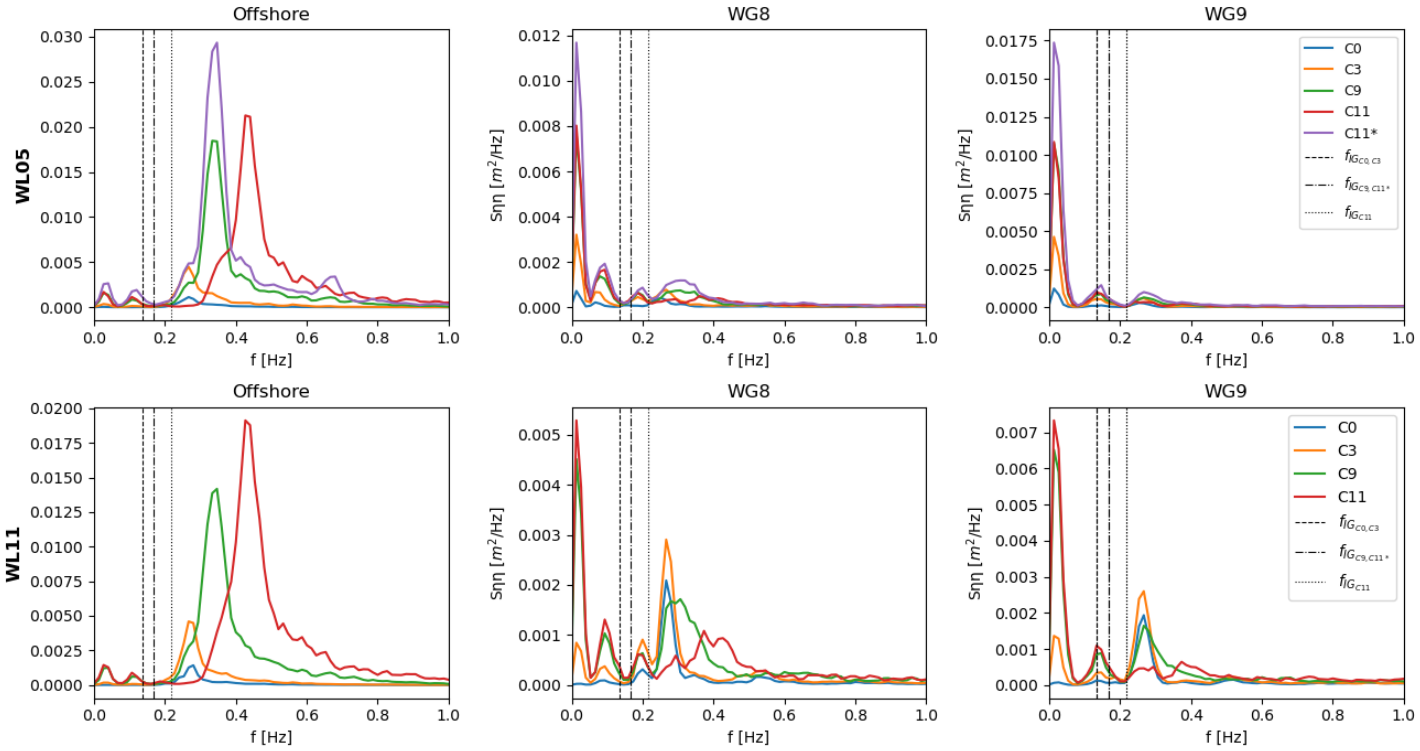

Figure 4.1: Variance density spectra of surface elevation for the total wave field, including both incoming and reflected waves on the reef flat and considering the full frequency band, for all the explored wave conditions and water levels (WL05:first row, WL11: second row)

The strong influence of infragravity waves on the reef flat in shaping the total signal can further be observed, directly from the timeseries itself. When a segment of the record is plotted, as shown in figure 4.2, the free surface elevation oscillates on a timescale consistent with the period of the long waves.

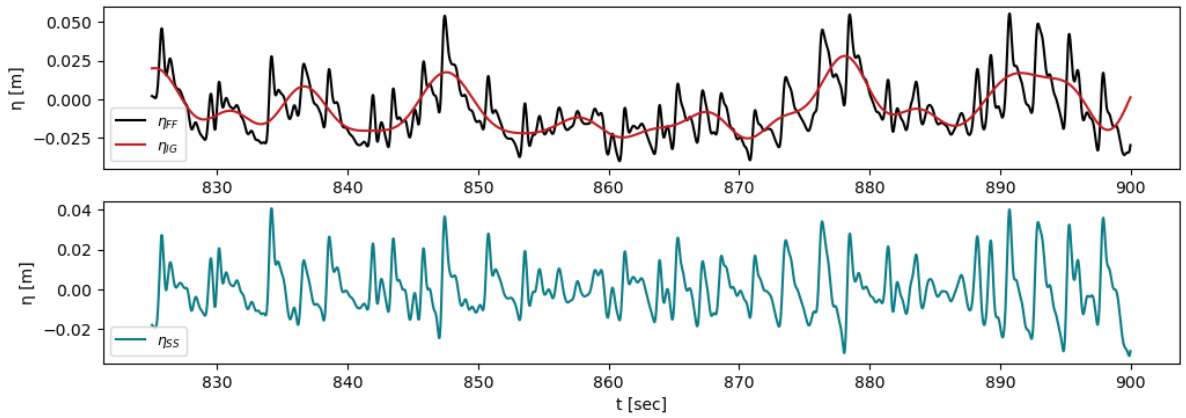

Figure 4.2: Surface elevation time series at the location A, for condition **C11WL05**, considering the total wave field, top figure: full frequency band and infragravity waves, bottom figure: sea swell waves

To clearly identify the dominance of infragravity or sea swell waves across the different conditions, figure 4.3 is created, which presents the percentage of energy contained within each frequency band relative to the full band signal, based on the total wave field. The graph confirms the dominance of infragravity waves on the reef flat for most of the cases in WL05, as suggested by figure 4.1. For the high water level experiments, the contribution of infragravity waves is below 32% for almost all cases, which corresponds to the lowest value observed for WL05. This suggests that the dominance of infragravity waves may be more strongly influenced by the imposed water level than by the incoming wave conditions. Furthermore, for conditions C9 and C11 which represent stormy weather conditions, the percentage of infragravity waves increases. Nevertheless, even under these energetic conditions, sea swell waves remain the dominant component of wave motion for all the wave conditions.

A final remark concerns the example of condition C11WL05. As shown in figure 4.3, C11WL05 exhibits the highest percentage of IG waves, reaching up to 66% of the full frequency band. However, as depicted in figure 4.2, although the presence of long waves significantly alters the resulting signal, the contribution of the sea swell waves remains clearly identifiable.

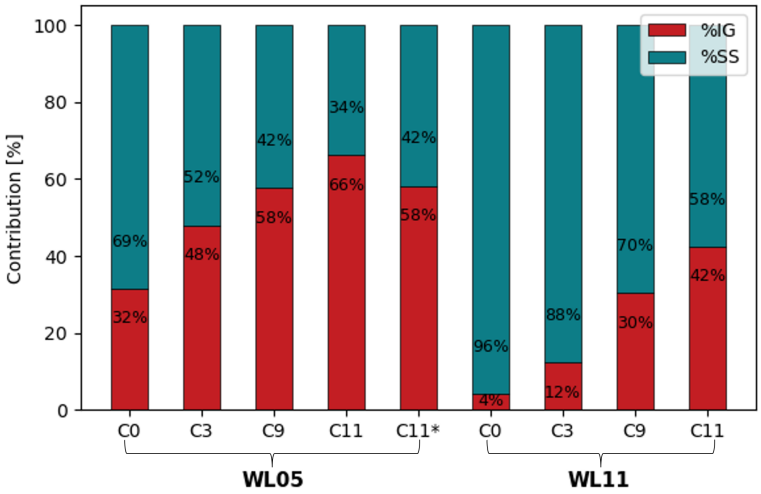

Figure 4.3: Percentage of infragravity and sea swell wave energy among the full frequency band, considering the total wave field at the location of WG8

Depth induced wave breaking imposed by the reef's steep slope, leads to wave height saturation on the reef flat and, depending on its intensity, increases the relative contribution of infragravity waves in the wave spectrum.

4.1.2. Reflection

The second characteristic phenomenon found in a fringing reef environment that should be addressed, is reflection. Although reflection can occur on any beach, in a fringing reef environment specifically, the steep slopes present on the foreshore are expected to result in high reflection rates. Furthermore, long waves are known to reflect almost fully for steep slopes. Considering the significant percentage of long waves propagating on the reef flat, this behavior is particularly relevant for the present experimental set up, where IG waves are expected to contribute substantially towards high reflection rates.

To quantify reflection, the reflection coefficient K_r is defined:

$$K_r \overset{(1)}{=} \frac{H_r}{H_i} \overset{(2)}{=} \sqrt{\frac{E_r}{E_i}} \overset{(3)}{=} \sqrt{\frac{m_{0,r}}{m_{0,i}}} \tag{4.1}$$

Where:	H_r	[m]	=	Reflected wave height
	H_i	[m]	=	Incident wave height
	E_r	[Jm^{-2}]	=	Reflected wave energy
	E_i	[Jm^{-2}]	=	Incident wave energy
	$m_{0,r}$	[m^2]	=	Zeroth spectral moment of $S_{\eta\eta}$ of the reflected waves
	$m_{0,i}$	[m^2]	=	Zeroth spectral moment of $S_{\eta\eta}$ of the incident waves

The incoming and reflected components used in equation 4.1 are obtained using the separation method described in 3.2.2. For irregular waves, when the spectral wave height H_{m_0} is used as input in equation 4.1, relationship (1) can be reformulated into relationship (3). This follows from the fact that wave energy is proportional to the square root of the wave height $E \propto H^2$, and to the zeroth spectral moment of surface elevation moment by $E = m_0/\rho g$. This transformation suggests that if more than 50% of the incoming energy is reflected, thus $E_i/E_r > 0.5$, then the corresponding reflection coefficient will be greater than approximately 0.707. The reflection coefficient can be calculated for the full frequency band, as well as for the infragravity or sea swell waves individually.

Table 4.3 presents the calculated reflection coefficients for each case corresponding to the full frequency band. The second column indicates the percentage of IG waves in the incoming wave field, while the third one presents the zeroth moments, which are representative for the wave energy, of the total wave field. The results indicate that for almost all low water level cases, more than 50$\%$ of the incoming wave energy is reflected seaward and propagates back across the reef flat. The strong presence of infragravity waves on the reef flat, already suggested by figures 4.1 and 4.3, and further verified by the second column of the table, contributes to the high reflection rates. Furthermore, the cases with the highest percentage of incoming IG waves, namely C9WL05, C11WL05 and C11*WL05, exhibit the largest reflection rates, suggesting that as the dominance of the infragravity waves in the incoming wave field increases, the reflection coefficient also increases. For the high water level, WL11, although the presence of long waves is less dominant and the reflection coefficients are consequently smaller, the total wave energy present on the reef is, however, greater than in WL05, as seen by the third column of the table.

Table 4.3: Infragravity energy fraction and reflection coefficient for different conditions

Condition	K_{r8}	IG_{inc} (%)	$m0_8$
C0WL05	0.628	24.50	0.00008
C3WL05	0.745	36.87	0.00023
C9WL05	0.799	47.52	0.00047
C11WL05	0.813	56.30	0.00048
C11*WL05	0.813	48.41	0.00071
C0WL11	0.542	2.29	0.00017
C3WL11	0.573	7.45	0.00032
C9WL11	0.643	20.35	0.00054
C11WL11	0.665	29.83	0.00054

Reflection is important to be acknowledged, as superposition of reflected and incoming waves modifies the incoming wave height. For location A, the waves are superimposed such that the total wave field presents an increase in the wave height. This explains why the total forcing found on certain locations can be more intense compared to the incoming one, although waves are breaking and wave energy would otherwise be expected to decrease. Specifically for fringing reefs, Pequignet et al. (2009) has shown, that the reef flat - offshore bathymetry system, can be treated as a semi-closed basin where standing waves can develop. In such a case, resonant modes with nodes and antinodes can appear, with an antinode at the shore and a node at the reef edge. Consequently, the degree of amplification of the wave parameters, resulting from the superposition of the incoming and reflected waves, depends on the cross-shore location.

Considering location A, the amplification of the total wave height can be observed from figure 4.4. The figure presents the variance density spectra, of the full frequency band, for the total and incoming waves, for all the experimented conditions. The larger area under the curves representing the total surface elevation, compared to the incoming signals, indicates that the total wave height H_{m_0} is in fact larger than the incoming$H_{m_0,inc}$.

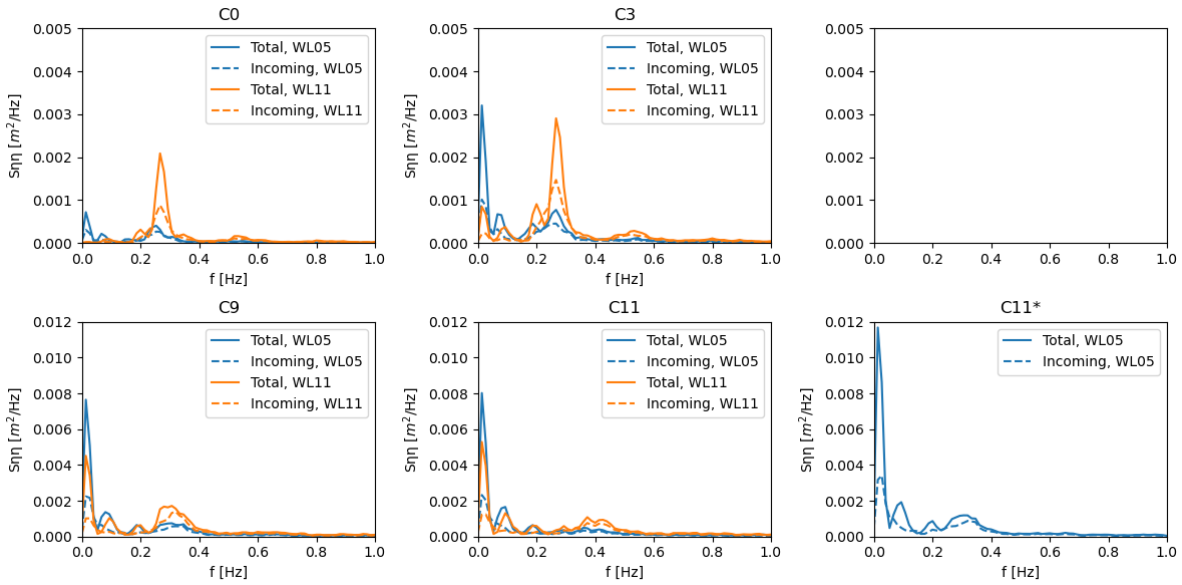

Figure 4.4: Total and Incoming surface elevation variance density spectra for all the conditions tested under WL05 considering the full frequency band

Reflection results to an amplification of the wave forcing found on location A, and thus experienced by an object placed in flow in that location. Since the highest reflection rates are observed in cases where the infragravity wave presence is more pronounced, these conditions exhibit the most significant amplification of the incoming wave parameters.

4.2. Estimated velocity and acceleration

Using equations 2.7 and 2.8, the estimated velocity and acceleration are calculated for the total wave field and the incoming waves, as explained in chapter 3. The resulted values for the irregular and regular waves are presented on figures 4.5 and 4.6 respectively. The input values of the required parameters for the calculations and the analytic values u_{est} and α_{est} for both the total and incoming waves are concentrated in tables C.1, C.2, C.3 and C.4 in appendix B.

As multiple variables are used as inputs in the calculation of velocity and acceleration, isolating the individual effects of the wave height, period, or water depth is not straightforward. However, certain patterns found in the nearshore values of these parameters are imprinted in the estimated velocity and acceleration values.

For instance, both figures 4.5 and 4.6 show that the estimated incoming wave variables, following the pattern proposed by the wave heights (figure 4.4), present smaller velocity values compared to the ones corresponding to the total wave field, therefore, $u_{est,tot} > u_{est,inc}$. This difference reflects the influence of reflection in shaping the total forcing on the reef flat. A similar trend is observed for most of the acceleration values, although for conditions C9, C11 under the high water level, this relationship is reversed. Furthermore, figure 4.5 indicates that larger velocities are observed under the low water level (WL05), although WL11 resulted to more energetic conditions, as shown by 4.1.

Considering an intra-case comparison with constant initial SWL, figure 4.5 shows that more energetic conditions result into higher estimated velocities. This is particularly relevant when comparing conditions C9WL05 and C11WL05, which correspond to the transition point between instability and stability observed in the experiments. Specifically, the higher energy associated with C9WL05 is reflected in the estimated velocities, as both the total and incoming estimated velocities for C9, 0.476 m/s and 0.336 m/s respectively (also found in table C.3) are higher than the ones calculated for C11: 0.447 m/s and 0.317 m/s. When these values are used as inputs in the Shield's and Morison formulations, (equations 2.4 and 2.21), the difference presented, becomes even more pronounced, since the minimum required weight depends on the velocity term raised to the power of two.

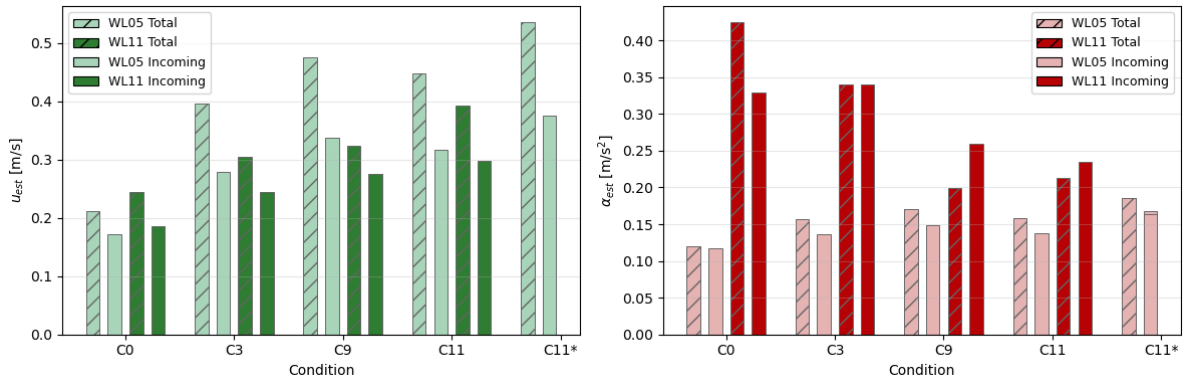

Figure 4.5: Estimated velocity and acceleration using equations 2.7 and 2.8, considering the total and incoming waves, for irregular waves

For regular waves, the influence of the nearshore values of the governing parameters is more easily interpreted for the estimated accelerations. Across cases R3 to R11, the wave energy increases, due to the larger offshore wave height, and the waves become shorter (table 3.2). Since acceleration scales linearly with the wave height and to the power of two with the frequency, the pattern illustrated by figure

4.6 is probably dominated by the differences in wave periods and the resulting wave heights. This explains the increase in accelerations from R3 to R11.

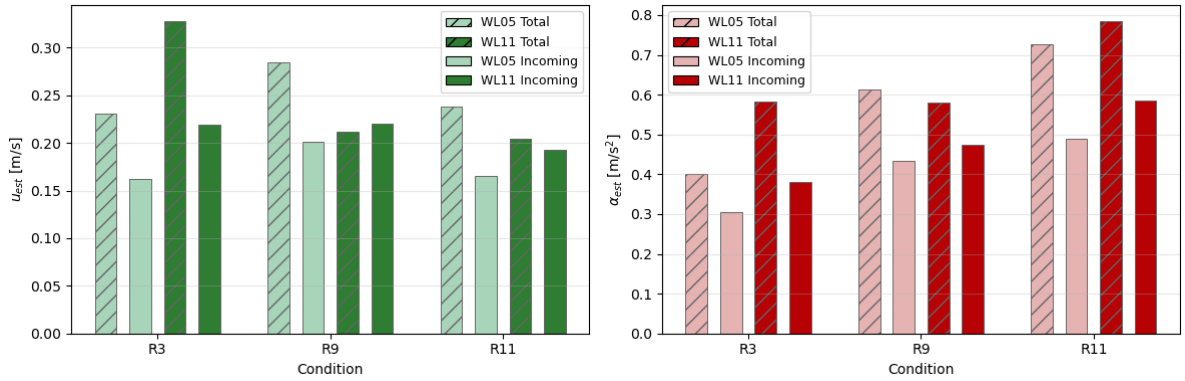

Figure 4.6: Estimated velocity and acceleration using equations 2.7 and 2.8, considering the total and incoming waves, for regular waves

For the case of irregular waves, where multiple harmonics are present, it becomes interesting to examine the contributions of two proposed frequency bands separately. Therefore, using the spectral wave height and the mean spectral period of the total wave field, derived from the timeseries of either the infragravity or sea swell waves, the corresponding $u_{est,IG}$ and $\alpha_{est,IG}$ are calculated (similarly, $u_{est,SS}$ and $\alpha_{est,SS}$ for the sea swell waves). These values, together with the estimated values considering the full frequency band, are presented in figure 4.7. The input parameters used for these calculations, as well as the resulting values, are provided in tables C.1, C.3 in the appendix B.

Figure 4.7 indicates that for both variables, most of the full band wave values are closer in magnitude to the corresponding infragravity waves values. The only cases that deviate from this behavior occur when the infragravity wave contribution is weak, such as C0WL11, C3WL11 (figure 4.3).

Furthermore, the smaller magnitudes of the sea swell wave velocities, relative to the other components, are consistent with their lower energy found relative to IG waves (figure 4.3), influenced by the mechanisms discussed in chapter 4.1. Consequently, the difference in their respective obtained wave heights (table C.1), is sufficient to produce differences in the calculated velocities. In contrast, as far as acceleration is concerned, the sea swell waves clearly dominate over the IG waves. As acceleration is a function of the frequency squared, the SS waves, characterized by smaller mean spectral periods (table C.1) and thus larger frequencies, result into larger acceleration values.

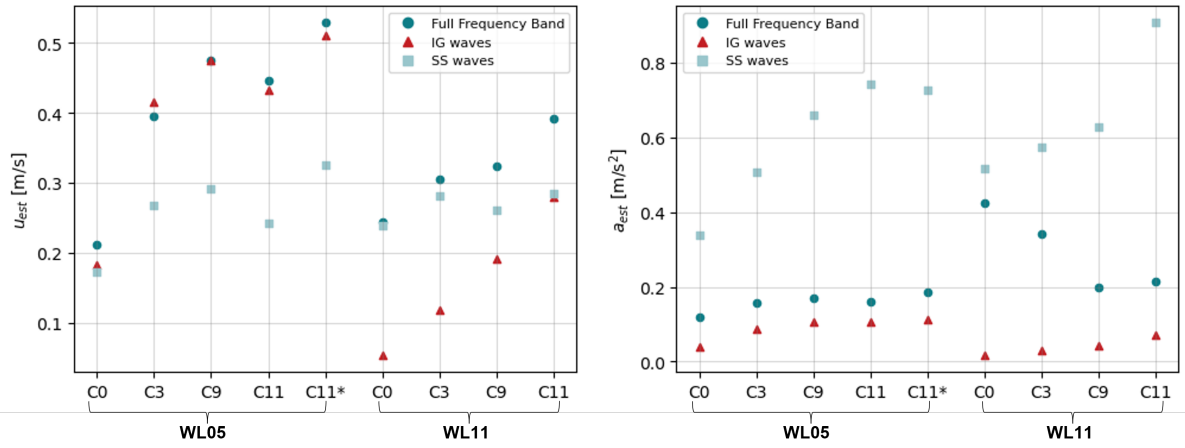

Figure 4.7: Estimated velocity and acceleration using equations 2.7 and 2.8, considering seperately the full frequency band, IG waves and SS waves

Considering the estimated parameters, infragravity waves dominate the velocity values, while sea swell waves dominate the acceleration field

4.3. Measured velocity and resulting acceleration

The second set of parameters refers to values of the velocity and acceleration, obtained directly from the velocity and acceleration timeseries. The parameters considered, namely the maximum velocity u_{max}, the root mean square velocity u_{rms} and the maximum acceleration α_{max} are computed from the time series based on the identified maxima and equation 3.11. Firstly, the values of the full frequency band are considered and presented in table 4.4.

Table 4.4: Measured root mean squared velocity, maximum velocity and maximum acceleration at location A for **irregular waves**

Condition	u_{rms} [m/s]	u_{max} [m/s]	a_{max} [m/s^2]
C0WL05	0.101	0.414	1.633
C3WL05	0.156	0.632	1.893
C9WL05	0.199	0.920	2.312
C11WL05	0.188	0.869	2.460
C11*WL05	0.220	0.974	2.810
C0WL11	0.095	0.348	1.583
C3WL11	0.131	0.498	1.846
C9WL11	0.158	0.632	2.049
C11WL11	0.160	0.625	2.058

Table 4.5: Measured root mean squared velocity, maximum velocity and maximum acceleration at location A for **regular waves**

Condition	u_{max} [m/s]	a_{max} [m/s^2]
R3WL05	0.281	1.296
R9WL05	0.289	1.497
R11WL05	0.254	1.264
R3WL11	0.257	1.400
R9WL11	0.356	1.581
R11WL11	0.345	1.503

The root mean square velocity values are used as an input option in the calculation of the Shields' parameter . The u_{rms} values presented in table 4.4, are smaller than the corresponding u_{est} ones per wave condition as shown in figure 4.5. Furthermore, the maximum velocities obtained directly from the measured time series exceed the corresponding root mean squared ones. This is expected, as a root mean square value, obtained from any signal, represents a measure of the average signal magnitude, whereas the maximum value captures its peak.

Comparing the measured maximum quantities with their corresponding estimated values, as shown in figure 4.5 (and in table form in C.3), table 4.4 reveals that for most cases, the maximum measured velocities are larger than the estimated ones. Regarding acceleration, the maximum values α_{max} clearly exceed their respective estimated values. In fact, the magnitude of the calculated maximum accelerations may seem unrealistically large at first. However, this behavior is expected to some degree, considering that the acceleration signal is derived from the derivative of velocity signal over time. Accordingly, the mathematical properties of differentiation, imply that steep gradients in the examined time series, here referring to the velocity signal, result in large magnitudes of its derivative, the acceleration signal. This behavior is illustrated in figure 4.8. As the total velocity signal presents saw-tooth asymmetry, imposed by the short waves, the steep slope found during the rising phase of the velocity signal, is translated into the large acceleration magnitudes suggested by table 4.4.

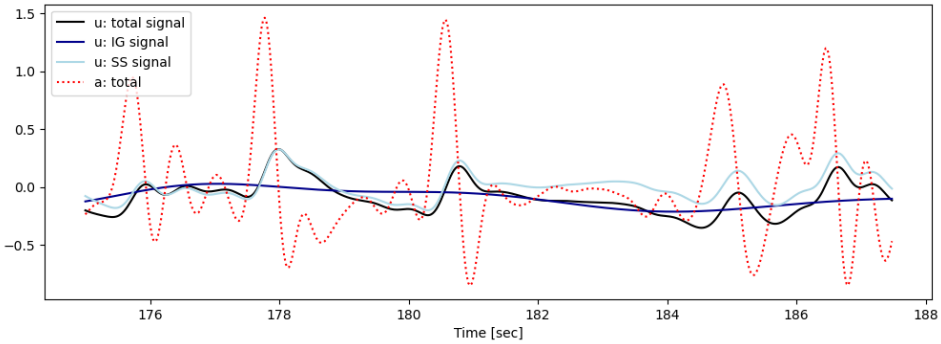

Figure 4.8: Influence of the velocity signals in shaping the total acceleration timeseries

Lastly, for irregular waves, a similar analysis is performed as for the estimated variables, in which the maximum values of velocity and acceleration are plotted separately in figure 4.9 for each frequency band. The figure reveals a significantly different distribution of dominance among the frequency bands compared to that shown in Figure 4.7 for velocity. Specifically, the measured maximum values, suggest that the SS wave velocity is no longer negligible, considering its magnitude is very similar to the corresponding IG component and, in most cases (except C11WL05), it exceeds it. Regarding acceleration, the sea swell contributions nearly coincide with the total signal. Therefore, the maximum acceleration values can be attributed almost entirely to SS waves. The IG wave acceleration components, although significantly lower from both the total and SS values, appear to lie within a similar range than the one proposed by the estimated values by equation 2.8.

A final remark, concerns the intra-case distribution of measured quantities. Specifically, the decomposition into separate frequency bands reveals that the velocities of the FF and SS waves present a similar behavior across conditions C9, C11 and C11* conditions for WL05, as their values are higher for C9 than C11 (figure 4.9. In contrast, the measured values for the IG waves, are the only set of values found, in terms of velocity and acceleration, among all the estimated and measured combinations presented in figures 4.5, 4.7 and 4.9, that suggest that the velocity of C11WL05 is larger compared to C9WL05.

This is an important observation, as in practice, for the 2 element experiments, C11WL05 produced unstable conditions, whereas C9WL05 did not. In order for any of the proposed formulations to be successful in predicting instability, the input values of the governing parameters should be able reproduce the instability pattern observe in terms of their magnitudes. For instance, the value of the Shields' parameter, is directly related to the magnitude of the input velocity. Therefore, for the Shield's method to be effective in identifying the stability transition observed between C9 and C11, it should be that the velocity input for C11 should exceed the C9 one. Otherwise, it would be impossible for equation 2.21 alone to capture the observed stability transition point. A similar reasoning , although more complex due to the role of the maximum velocity in defining the force coefficients, applies to the input variables of the Morison equation as well.

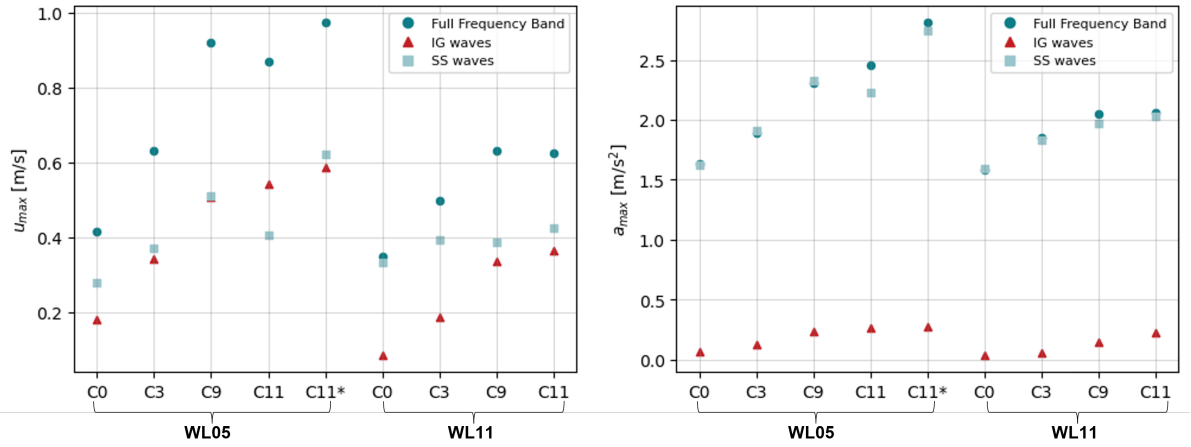

Figure 4.9: Measured maximum velocity and acceleration, considering separately the full frequency band, IG waves and SS waves

Considering the measured parameters, both infragravity and sea swell waves contribute significantly to the velocity field, whereas the acceleration field is predominantly governed by the sea swell component.

5

Stability Observations

This chapter presents the stability outcomes observed visually during the experiments. These observations are used to classify each condition as stable or unstable, a characterization essential to assessing whether the effectiveness of the predictions acquired by the Shields or Morison methods are reliable or not. In that context, **a condition is characterized as unstable if the AR on the reef flat exhibited noticeable displacement or rotation.**

Of the two experimental phases originally planned, more emphasis is placed during the analysis on the two-element experiments. This is because the intra-structure variability of the down-scaled reefs, introduced significant uncertainty regarding its suitability to represent the original configuration. Nevertheless, some preliminary results are presented for both.

5.1. 2 element experiments

Firstly, the stability of the two element experiments is discussed. From the defined conditions across both regular and irregular waves, clear movement was observed under conditions **C11WL05, C11*WL05** and **C11*WL05_Op**, shown in figure 5.1. A minor movement of was observed for the 5 cm AR during C9WL05, which however was smaller than 0.5 cm and thus being almost inconceivable it is assumed as negligible. Accordingly, C9WL05 is classified as stable for both AR elements. The resulting movement for these cases is presented in figure 5.1. For reference, the Γ symbols on the foreshore shown in the figure, indicate the locations of the AR units on the foreshore within the complete reef restoration. Therefore, the vertical spacing between the black Γs corresponding to the 4 cm restoration, is 11 cm, while the spacing between the red markers 12 cm.

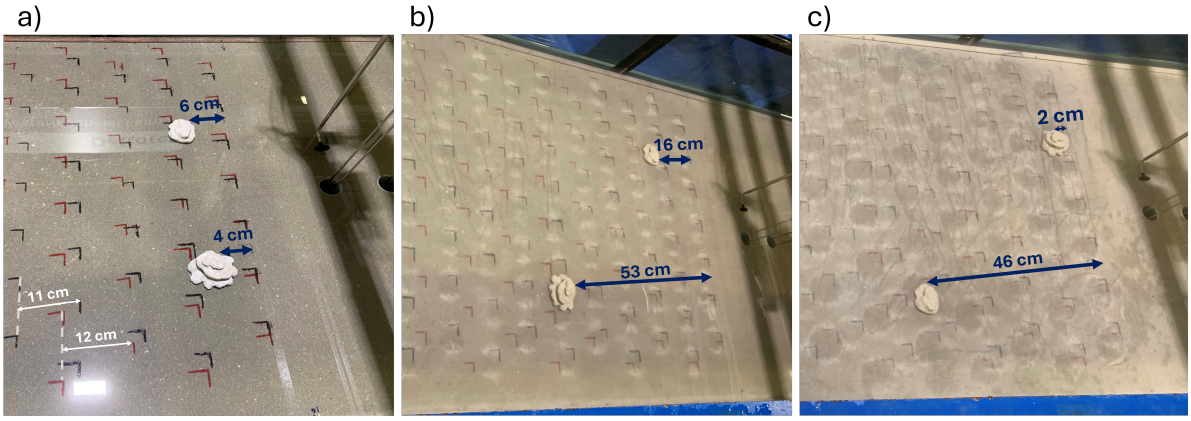

Figure 5.1: Top view of total movement observed by the end of each run for conditions a) C11WL05, b) C11*WL05, and c) C11WL05_Op

For condition C11, movement was abrupt and occurred only once, around t = 1450 sec ≈ 24 min (figure 5.2). Both elements moved simultaneously, where between the two, the 4 cm exhibited greater displacement, moving 6 cm, while the 5 cm one moved 4 cm. The 4 cm AR also displayed a slight rotation about its axis.

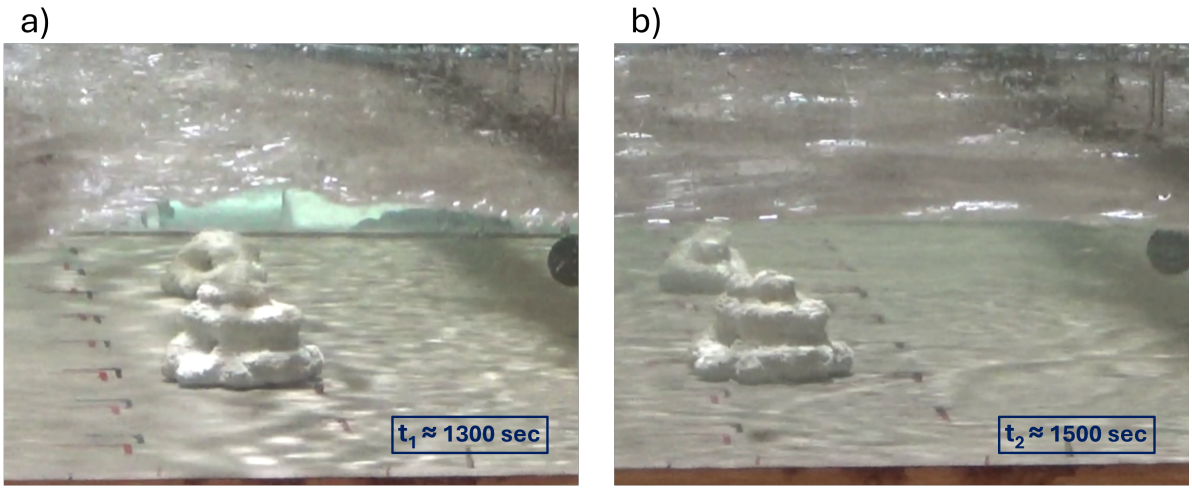

Figure 5.2: Side view of movement observed during condition C11WL05, captured before and after the observed movement, approximately at a) t_1 = 1300 sec, and b) t_2 = 1500 sec

In contrast with condition C11, during condition C11*, the 5 cm AR was more unstable than the 4 cm one. Quantified in terms of displacement, the 5 cm one moved 53 cm from its original position, whereas the 4 cm moved 16 cm, thus covering a comparatively smaller distance. Furthermore, the 4 cm AR moved only once, at approximately t = 1440 sec ≈ 24 min, although minor rotations were observed prior to that. The 5 cm AR unit exhibited more frequent motion, with at least five distinct movement events occurring approximately at 700, 900, 1140, and 1440 s, corresponding roughly to 11.5, 15, 19, and 24 minutes. The average displacement per event was approximately 15 cm. Some of the intermediate locations that the ARs where found on which indicate the movement of each event are presented in figure 5.3

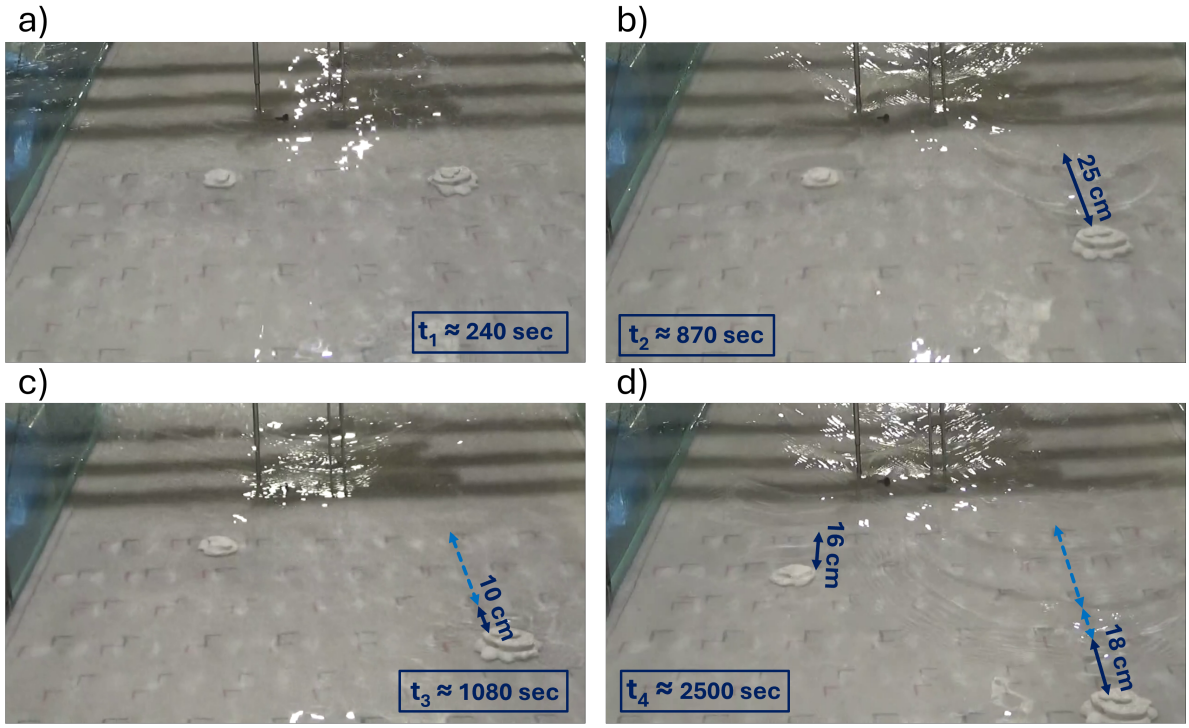

Figure 5.3: Top view of movement observed during condition C11*WL05, successive movement events: a) t_1 = 240 sec: original placement, b) t_2 = 870 sec: after the first major motion, c) t_3 = 1080 sec: following the second movement d)t_4 = 2500 sec: final position

For condition C11*WL05_Op, the available footage does not allow the identification of all instances were movement occurred. A common issue during the experiments was that suspended cement in the water hindered visibility thereby limiting the effectiveness of the side view videos, while top view recordings were also of limited use, as the propagating turbulence made it difficult to clearly discern the elements. Regardless, for the 4 cm AR, at least 3 movement events are reported, around 610 sec, 650 sec and 660 sec, thus being concentrated around the 10th minute of the simulation. Beyond this point, the 4 cm AR unit left the frame and could no longer be monitored. The movement of the 5 cm reef was too small to be captured from the cameras due to the reasons discussed. The final movement of each one was 45 cm for the 4 cm AR and 3 cm for the 5 cm AR.

A comparison of the stability outcomes between conditions C11*WL05 and C11*WL05_Op presented in figure 5.1, suggests that the element placed on the upper part of the cross-section is consistently more stable. This observation implies that, possibly, it is the position of the element within the cross-section that creates more unstable conditions, and not the size of the element itself. This behavior may be attributed to a sheltering effect, as the upper unit is positioned behind the EMF. Although relatively small, the presence of the EMF during small scaling experiments, combined with the shallow water conditions, might have influenced the local forcing. Considering the above observations, it is not safe to make assumptions on the influence of the reef's size in stability optically.

A summary of the stability classification of each AR under each forcing condition is described in tables 5.1 and 5.2:

Table 5.1: Observed stability for the 2 element experiments under **irregular waves**, *stable = minor movement observed which was ultimately neglected

Condition	4 cm AR	5 cm AR
C0WL05	Stable	Stable
C3WL05	Stable	Stable
C9WL05	Stable	Stable*
C11WL05	**Unstable**	**Unstable**
C11*WL05	**Unstable**	**Unstable**
C11*WL05_Op	**Unstable**	**Unstable**
C0WL11	Stable	Stable
C3WL11	Stable	Stable
C9WL11	Stable	Stable
C11WL11	Stable	Stable

Table 5.2: Observed resulted stability for the 2 element experiments under **regular waves**

Condition	4 cm AR	5 cm AR
R3WL05	Stable	Stable
R9WL05	Stable	Stable
R11WL05	Stable	Stable
R3WL11	Stable	Stable
R9WL11	Stable	Stable
R11WL11	Stable	Stable

5.2. Full Reef experiments

In this section, some preliminary observations regarding the stability of the full reef restorations are presented. The total numbers of ARs that were found unstable for each wave condition are summarized on tables 5.4 and 5.4.

Table 5.3: Number of unstable AR units per configuration under **irregular waves**

Condition	4 cm AR restoration	5 cm AR restoration
C3WL05	4	0
C9WL05	10	4
C11WL05	23	10
C11*WL05	Reef Failure	17
C0WL11	2	-
C3WL11	4	0
C9WL11	11	1
C11WL11	14	3

Table 5.4: Number of unstable AR units per configuration under **regular waves**

Condition	4 cm AR restoration	5 cm AR restoration
R9WL05	2	0
R11WL05	3	2
R9WL11	-	0
R11WL11	-	2

Under regular waves the restorations were mostly stable, with motion limited to less than 3 units moving across both water levels and reef heights. In contrast, irregular waves had a greater impact on the restorations' stability, exhibiting variable patterns of motion depending on the intensity imposed wave forcing. In particular, for the most energetic cases, significant movement was observed (table 5.3), with condition C11*WL05 leading the 4 cm reef to failure, as shown in figure 5.5. Table 5.3 further suggests that conditions C9WL05, C11WL05, and C11*WL05, which were identified as the most unstable in the 2 element experiments, are likewise observed to be the most unstable during the full reef experiments.

Particular attention should be given to the difference in movement between conditions C9WL05 and C11WL05, which represent the transition point identified in the 2 element experiments. Table 5.3 shows that for both reef sizes, once this threshold is exceeded, the number of unstable units approximately doubles, as for condition C9WL05 10 and 4 AR units were unstable for the 4 cm and 5 cm restorations respectively, whereas for condition C11WL05 the unstable pieces were 23 and 10. Figure 5.4 further illustrates the increased motion that transpired under condition C11WL05, compared to C9WL05.

An additional observation concerns the behaviour of the AR units selected to represent the reef in the two element experiments, when placed in the full reef restoration. Although both units were unstable

for condition C11WL05, when placed within the full restoration they remained stable, as indicated by the blue circles in 5.4.

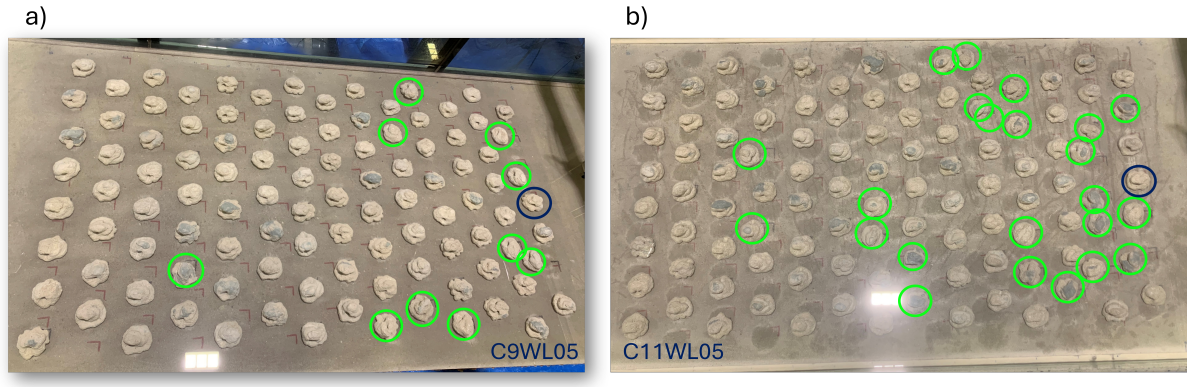

Figure 5.4: Top view of total movement observed in the **4 cm AR restoration** by the end of each run for conditions **C9WL05** and **C11WL05** a) condition C9WL05, b) condition C11WL05. Green circles: unstable AR units, Blue circles: AR unit that was used for the 2 element experiments

Comparing the response of the two reef heights under identical forcing conditions, table 5.3 reveals that the 5 cm reef appears to be more stable. This is particularly evident for condition C11*WL05, where as shown in figure 5.5, the 5 cm reef exhibited movement primarily in the front rows, whereas the 4 cm reef experienced complete failure. Therefore, no elements are marked as unstable in the left image of the figure, as only a few of the elements in the last rows appear to have remained in their initial positions.

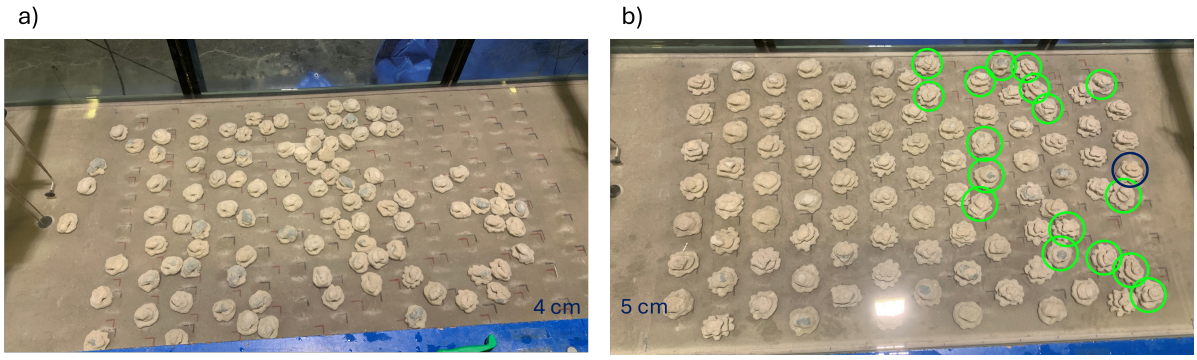

Figure 5.5: Top view of total movement observed in the **4 cm AR restoration** by the end of each run for conditions **C9WL05** and **C11WL05** a) condition C9WL05, b) condition C11WL05. Green circles: unstable AR units, Blue circles: AR unit that was used for the 2 element experiments

6

Stability Prediction Methods for Isolated Reef Elements

Having defined the stability outcomes for each case, the effectiveness of the Shields and Morison methods in accurately predicting these outcomes is examined.

6.1. Shields' method Predictions

Compared to the Morison approach, Shields' formulation is simpler, as it evaluates whether the threshold of motion is exceeded, and thus only suggests if movement is expected to occur. Therefore, if effective in predicting stability, it can be used as an initial assessment regarding the stability conditions. Moreover, although the magnitude of exceedance of the Shields parameter θ relative to its critical value θ_{cr} does not directly quantify the degree of instability, an intra-case comparison of the resulted θ values can act as an indication of which case is more unstable. Considering this clarification, hereafter, examining the Shields' parameters obtained, a case characterized as more unstable, refers to a case with a higher θ which is therefore more likely to experience movement, depending on the threshold of motion defined. As mentioned in chapter 2.2.2, the critical Shields parameter range is defined for the traditional case of a granular bed, as a range of 0.03 to 0.06. In this study, a representative value of θ_{cr} equal to 0.055 is adopted.

The Shields parameters θ are calculated for each of the tested wave conditions using equation 2.21. The velocity term is initially substituted by the maximum measured near-bed velocity, selected to represent the most critical hydrodynamic conditions encountered during each run. Taking into account the complexity of selecting the appropriate parameter to accurately describe an irregular wave field, the Shields number is also computed using the root mean square velocity u_{rms} and the estimated velocity u_{est} of the total wave field, both considering the full frequency band. More precisely, u_{rms} is employed in an attempt to examine whether using an average characterization of the sea state, also considering its smaller values compared to u_{max} (table 4.4), could provide a closer approximation to the conventional instability threshold θ_{cr}. The estimated velocity u_{est}, is included to reflect practical situations where only surface elevation data are available and thus the velocity term has to be estimated. All resulting values are presented in figure 6.1.

Figure 6.1 shows that when the maximum velocities measured are used, the resulting Shields numbers significantly exceed the proposed critical number θ_{cr}= 0.055 threshold. As a result, the method predicts movement for all the tested cases. This contradicts the experimentally observed stability pattern, proposed in table 5.1, indicating that the use of the maximum measured velocity as input does not provide reliable results. Considering the root mean square velocity u_{rms}, due to the smaller magnitude of the input parameters, the Shields parameters are accordingly smaller than those using u_{max}. Nevertheless, it appears to be that the traditionally defined threshold still fails to capture correctly the unstable cases, as it incorrectly predicts movement for conditions C3WL05, C9WL05, C9WL11 and C11WL11. The θ values derived from u_{est}, are smallest than the values derived by using u_{max}, however they remain

above the proposed stability threshold, leading to the same conclusion regarding the overprediction of instability.

In conclusion, none of the proposed options is able to perfectly reproduce the observed stability pattern. Furthermore, all the approaches suggest that condition C9WL05 is more unstable compared to C11WL05. This, although logical as the variation of the calculated θ values follows the variation of the velocity across the examined cases, fails to identify the true transition point. A last remark concerns the two sizes used in the experiments. All of the proposed approaches suggest the 4 cm to be more unstable than the 5 cm one. However, this unfortunately cannot be verified from the experimental observations.

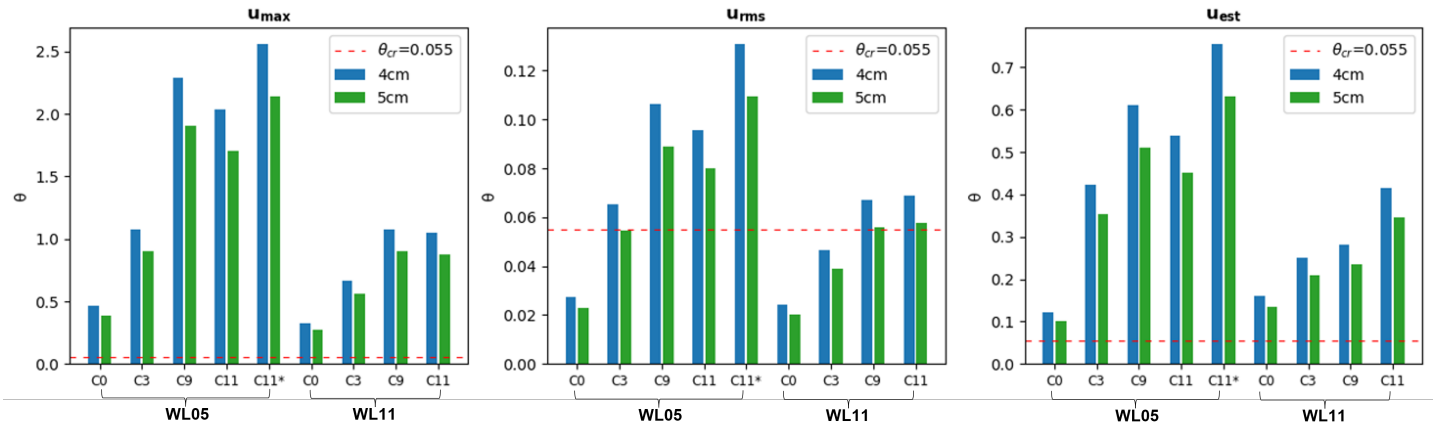

Figure 6.1: Shields numbers calculated using u_{max}, u_{rms} and u_{est} for the two AR designs of height 4 cm and 5 cm for irregular wave conditions

To investigate whether the method's inability to reproduce the observed behavior stems from the choice of the input parameters or from inherent limitations of the method itself, the Shields' parameters are calculated for the regular waves as well. Regular waves present the advantage that they consist of a single harmonic offshore and therefore their characteristic velocity can be defined more straightforwardly. The input parameters for the regular waves are the maximum measured velocity and the estimated one, for the same reasons proposed for the irregular waves, and the calculated Shields' parameters are shown in figure 6.2.

Since all the regular wave cases were stable (table 5.2), figure 6.2 shows that using neither the maximum velocity nor the estimated velocity leads to reliable results, as the threshold of motion is always exceeded. Considering that the offshore incoming field is monochromatic, the uncertainty in selecting a representative velocity as input for the calculations is reduced and thus any discrepancy between the predictions and the observations cannot be attributed to the definition of the velocity parameter. This suggests that the Shields' method, considering the traditionally proposed threshold values is insufficient to predict instability under the conditions examined in the present study.

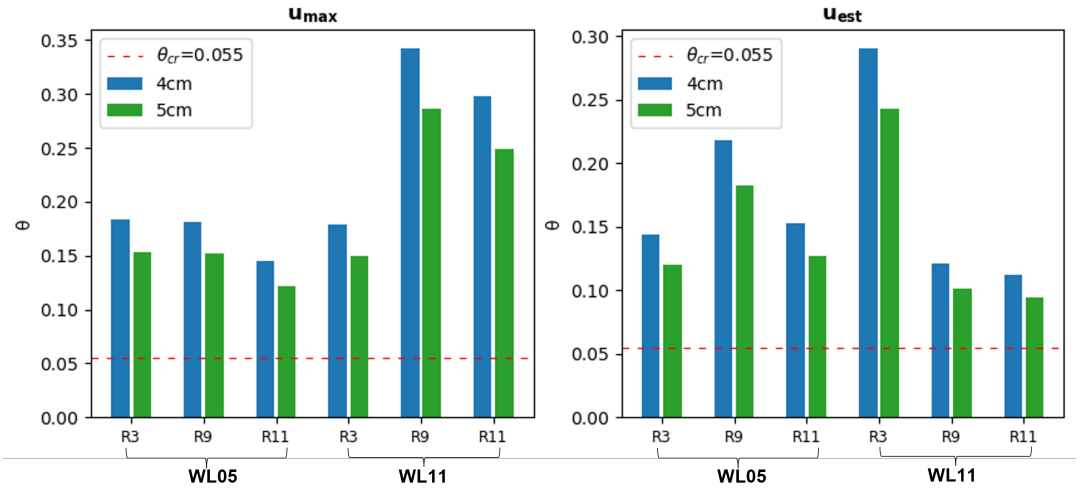

Figure 6.2: Shields numbers calculated using u_{max}, and u_{est} for the two AR designs of height 4 cm and 5 cm for regular wave conditions

The Shields' parameter method fails to capture the initiation of motion for both the regular and irregular waves considering the traditionally proposed threshold.

6.2. Morison method Predictions

In this section, the applicability of the Morison method will be examined. Once the force coefficients have been determined for each experimental condition, the only variables in equation 2.16 are the velocity and acceleration. Although these quantities are calculated, the appropriate representation to substitute in the equation might once again not be straightforward for the case of irregular waves. Accordingly, several approaches are examined, a summary of which is given it table 6.1. Moreover, given that the measured printed weights of the 4 cm and 5 cm ARs are **0.145kg** and **0.267kg** respectively, if the minimum required weight calculated by equation 2.15 is larger than the measured one, then the method predicts movement will occur.

6.2.1. Approaches considered

Considering that there are no specific guidelines on what parameters to use when designing an artificial reef configuration placed on a reef flat, different combinations of the forcing parameters used as inputs are considered.

Firstly, the influence of the incoming full frequency band waves is considered. This is selected as it is common practice in structural stability formulations to use the incoming spectral wave height $H_{m0,inc}$ in the the calculations. As such, **approach 1**, explores the stability using the **incoming** spectral wave height, combined with the mean water depth at the location of WG8 and the mean spectral period $T_{m_{-1,0,inc}}$, to estimate the minimum required weights for each condition.

Furthermore, for a project located in an environment such as a fringing reef where significant reflection occurs, the use of the total wave height may provide a more representative description of the wave forcing acting on the structure, as it accounts for the influence of reflection on the resulting wave conditions. Therefore, for **approach 2**, the **total** spectral wave height H_{m0} will be used, together with $T_{m_{-1,0}}$ and the mean water depth.

A limitation while applying equations 2.7 and 2.8 for the estimation of the velocity and acceleration terms for irregular waves, is the fact that they require the entire wave forcing spectrum to be summarized into a single harmonic. In the cases where there is a wide or bimodal spectrum, as for example C9WL11 and C11WL11 as proposed by figures 4.1 and 4.3, this simplification is increasingly less valid and using the entire frequency band might not adequately represent the dominant motion. As a result, approach 3 explores the contribution of each frequency band to the different force components.

To achieve that, the velocity and acceleration estimated separately for the IG and the SS waves are considered as inputs for the drag, inertia and lift force components. Assuming constant force coefficients, regardless of the choice of the frequency band used, the drag and lift force components are proportional to the velocity term and the inertia force is proportional to the acceleration term. Moreover, as illustrated by figure 4.7, the infragravity waves dominate the velocity term whereas the sew swell waves govern the acceleration term. Therefore, it can be inferred that the drag and lift forces are dominated by infragravity waves, while inertia forces are dominated by sea-swell waves. Consequently for **approach 3**, the **drag** and **lift forces** are computed using the **estimated infragravity wave velocity** $u_{est,IG}$ and the **inertia force** is computed using the **sea-swell estimated acceleration** $\alpha_{est,SS}$.

As discussed in chapter 2.2, Morison originally developed his formulation assuming regular waves where velocity and acceleration are estimated analytically through the surface elevation measurements, as described by equations 2.7 and 2.8. Conventionally, the application of the Morison method follows this approach, using estimated rather than measured hydrodynamic parameters. Examples from Düzbastılar and Şentürk (2009) and Diederen (2023) further support that practice. However, given the intricate hydrodynamic conditions found on a fringing reef, it is also examined whether the use of measured velocities provides a more accurate representation of the forcing when applied in the Morison formulation.

As such, **Approach 4** examines using as inputs into the Morison equation the **maximum measured velocity** and **acceleration** as proposed in tables 4.4 and 4.5.

Lastly, **approach 5** is designed in which the **maximum measured velocity** and **acceleration** values using only the **infragravity wave frequency band** is considered. This approach was introduced to isolate influence of the individual frequency bands and explore how different the predicted weights would be relative to approach 4. The IG wave components where chosen over the SS waves because they are found to dominate the reef flat, at least during the most unstable conditions.

The approaches mentioned are summarized in table 6.1 below.

Table 6.1: Alternative expressions for causal and conditional phrasing

Name	Origin of Input Variables	Type of waves considered
Approach 1	Estimated variables	Incoming waves, full frequency band
Approach 2	Estimated variables	Total waves, full frequency band
Approach 3	Estimated variables	Total waves, u_{IG} and α_{SS}
Approach 4	Measured variables	Total waves, full frequency band
Approach 5	Measured variables	Total waves, u_{IG} and α_{IG}

6.2.2. Choice of Force Coefficients

The most crucial prerequisite in the Morison method is the definition of the force coefficients.

The method followed to define the force coefficients is the one proposed by Sarpkaya (2010). This is justified on the grounds that he has proposed a comprehensive study in which the influence of relative surface roughness is incorporated into the determination of force coefficients. The influence of surface roughness on the estimation of the force coefficients is evident from the graphs presented in figures C.3, C.4 and C.5, which demonstrate substantial differences in the the values of force coefficients between rough and smooth surface assumptions. Since the ARs are built from cement and thus their surface is inherently rough, Sarpkaya's formulation can be theoretically considered as one appropriate choice.

In order to determine the force coefficients, the first step is to characterize the flow conditions for each run. Therefore, the dimensionless numbers Re, KC and k/D are calculated by equations 2.17, 2.3 and 2.18.

During the experiments, movement occurred abruptly at specific moments rather than continuously, which suggests that instability was most likely initiated during moments of maximum wave forcing. This consideration is particularly relevant for irregular wave cases, where the hydrodynamic forcing

varies greatly within the same run due to the irregular superposition of the multiple harmonics present. Consequently, to best approximate the conditions that lead to movement and capture the transition point for instability, it is decided to determine the force coefficients based on the extreme flow conditions found on each run. The flow parameters substituted into the Reynolds and Keulegan-Carpenter numbers are therefore selected based on the extreme values documented for each one.

Consequently, the characteristic velocity U used in both Re and KC numbers is taken as the maximum measured velocity u_{max}, determined as described in 3.2.5, with the values presented in tables 4.4 and 4.5. To account for the strong presence of long waves on the reef (as mentioned in chapter 4.1.1), the spectral wave period $T_{m_{-1,0}}$ was used. For regular waves, the period found on the reef was used. Regarding the characteristic length D, used in the Reynolds number and the relative density ratio, the nominal diameter d_n was used for each element, which is the diameter of the volumetric equivalent cylinder, defined in table 3.4. Lastly, the value of k for the relative roughness is substituted by 3 x 10^{-3} m, as proposed by Det Norske Veritas (2010) for a concrete elements. The resulting values are presented below:

Table 6.2: Reynolds number and Keulegan–Carpenter number calculated using measured maximum orbital velocities near the bed u_{max} for irregular waves, respectively for the AR units of nominal input height of 4 cm and 5 cm

	4 cm reef		**5 cm reef**	
Condition	Re	KC	Re	KC
C0WL05	20058	95	24011	79
C3WL05	30642	206	36682	172
C9WL05	44616	333	53409	279
C11WL05	42139	317	50445	265
C11*WL05	47228	359	56537	300
C0WL11	16871	26	20197	22
C3WL11	24138	58	28896	48
C9WL11	30618	133	36653	111
C11WL11	30287	149	36257	124

Table 6.3: Reynolds number and Keulegan–Carpenter number calculated using measured maximum orbital velocities near the bed u_{max} for regular waves, respectively for the AR units of nominal input height of 4 cm and 5 cm

	4 cm reef		**5 cm reef**	
Condition	$Re_{4\,\text{cm}}$	$KC_{4\,\text{cm}}$	$Re_{5\,\text{cm}}$	$KC_{5\,\text{cm}}$
R3WL05	12633	18	16324	16
R9WL05	12577	13	16755	12
R11WL05	11241	8	14726	8
R3WL11	12488	17	14901	14
R9WL11	17272	17	20654	14
R11WL11	16109	13	20008	11

The values presented on tables 6.2 and 6.3 indicate that a larger structure results in greater interference in the flow conditions. This is reflected in both the higher Reynolds numbers and the lower Keulegan-Carpenter values calculated for the 5 cm AR compared to the 4 cm one. Specifically, higher Re values are associated with more turbulent conditions, while lower KC values refer to cases where the inertia forces become relatively more important, as the fluid particle excursion during a wave cycle is smaller. Table 6.2, shows that for most irregular wave cases, KC exceeds 100, suggesting that oscillatory flow approaches steady flow conditions, where the drag forces are expected to dominate the hydrodynamic forcing. For regular waves, the KC number is much smaller in comparison and flow can no longer be

considered to approach steady flow conditions. However, the long input periods used for R3 and R9 still result in predominantly drag dominated regimes.

The force coefficients are then evaluated for each experimental run using the values found in table 6.2 and figures C.3, C.4 and C.5. Sarpkaya (2010) proposed 2 sets of figures for the C_d and C_m coefficients, corresponding to Keulegan-Carpenter numbers KC = 20 and KC = 100. The case KC = 20, represents drag dominated flow conditions, such as those observed in run C0WL11 and the regular waves, tables 6.2 and 6.3. In contrast, KC = 100 refers to conditions where steady flow is achieved. For KC values larger than 100, the coefficients the figures corresponding to KC = 100 are used.

For irregular waves, apart from C0WL11, the coefficients for all cases were defined using the graphs from figure C.4. The coefficients for C0WL11 and for the regular waves cases are defined with figure C.3. From the relative roughness curves proposed in the graphs, 1/50 was chosen, as it has the highest relative roughness and is the closest to the k/D values found in the experiments. Ultimately, the values of the force coefficients are:

Table 6.4: Hydrodynamic force coefficients per case for the 4 cm and 5 cm reef configurations for irregular waves

	4 cm reef			**5 cm reef**		
Condition	C_d	C_m	C_l	C_d	C_m	C_l
C0WL05	1.53	1.05	0.32	1.28	1.27	0.40
C3WL05	1.16	1.64	0.25	1.23	1.76	0.23
C9WL05	1.31	1.73	0.15	1.36	1.70	0.20
C11WL05	1.30	1.75	0.20	1.35	1.71	0.28
C11*WL05	1.34	1.71	0.15	1.38	1.70	0.20
C0WL11	1.54	1.43	1.20	1.56	1.42	1.55
C3WL11	1.28	1.27	0.58	1.17	1.55	0.71
C9WL11	1.16	1.64	0.23	1.23	1.76	0.30
C11WL11	1.16	1.64	0.23	1.23	1.76	0.30

Table 6.5: Hydrodynamic force coefficients per case for the 4 cm and 5 cm reef configurations for regular waves

	4 cm reef			**5 cm reef**		
Condition	C_d	C_m	C_l	C_d	C_m	C_l
R3WL05	1.65	1.19	2.00	1.57	1.34	2.05
R9WL05	1.65	1.19	2.20	1.57	1.34	2.40
R11WL05	1.69	1.15	2.00	1.63	1.22	1.80
R3WL11	1.65	1.19	2.10	1.57	1.34	2.10
R9WL11	1.54	1.43	2.10	1.57	1.42	2.10
R11WL11	1.54	1.42	2.20	1.56	1.43	2.40

As stated in chapter 2.2, the force coefficients depend on the prevailing flow conditions of each experiment and the relative roughness of the elements exposed to the flow. Therefore, given that the **values of the coefficients** are governed by the physical conditions of the experiment, their values defined in table 6.4 **are assumed to remain constant for a given condition, regardless of the method employed to calculate the velocity and acceleration used.**

6.2.3. Predictions using estimated parameters

Firstly, the effectiveness of the Morison equation will be tested using the estimated velocity and acceleration, presented in figures 4.5 and 4.7, therefore the results of approaches 1, 2 and 3 are presented in figures 6.3, 6.4, 6.5, 6.6 and 6.8.

For all the following graphs presenting the predicted required weights, stability is assessed by comparing the minimum predicted weight for each artificial reef unit with its actual measured weight. If the predicted required weight is lower than the measured printed weight, the AR unit is considered stable, indicating that the approach predicts no movement and vise versa. To explore the effectiveness of each approach proposed, the figures indicate whether the prediction of each approach matches the observed behavior, with “o” denoting a correct prediction and “x” an incorrect one. In cases of incorrect predictions, the required weight is either overestimated (when movement is predicted but not observed) or underestimated (when movement occurs but is not predicted). Since the exact required weight cannot be not known, the magnitude of the overestimation or underestimation is assessed based on the percentage of the deviation of the predicted value from the printed weight which defines the threshold of motion.

Using **approach 1**, the predicted weight for all cases is lower than the installed one, suggesting that no movement is expected for any of the cases. However, for WL05, conditions C11 and C11* were found to be unstable (table 5.1). This indicates that approach 1 underestimates the required weight, at least under these conditions. The minimum magnitude of the underestimation can be considered as the additional weight required to reach the instability threshold, and thus align with the experimental observations, which appears to be at least 30 gr for C11*WL05. Concerning the method’s intra-case predictability, C9 appears to be an outlier for the low water level, as it is shown to require a higher minimum weight compared to C11WL05. This contradicts the experimental observations where C11 was unstable but C9WL05 was not, but is nonetheless consistent with the observed variation of the calculated forcing illustrated in figure 4.5).

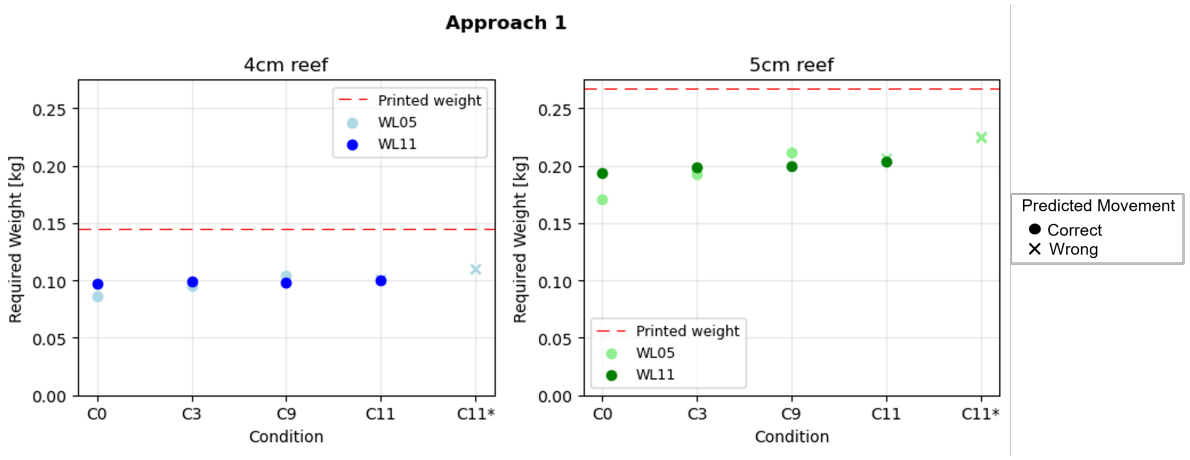

Figure 6.3: Predicted weights for the 4cm and 5cm reef under irregular wave conditions, for Approach 1, o: correct prediction x:incorrect prediction

Approach 2 demonstrates a relative improvement in predicting the required weights compared to approach 1. Although the transition point between C9WL05 and C11WL05 is still not captured and the miscalculation of the required weights for C11 and C11* for the 4 cm reef is still present, as they are incorrectly predicted as stable, the magnitude of the underestimation appears to be reduced, bringing approach 2 closer to accurately predicting instability. In particular, for the 5 cm reef, instability is incorrectly predicted only for C11WL05.

In addition, the results from **approach 2** make it clear that the printed 5 cm reef appears to be more unstable than the 4 cm one. Since the input hydrodynamic forcing is the same for both elements, the reduced stability of the 5 cm reef can be attributed to its bigger size and how it subsequently interacts with flow.

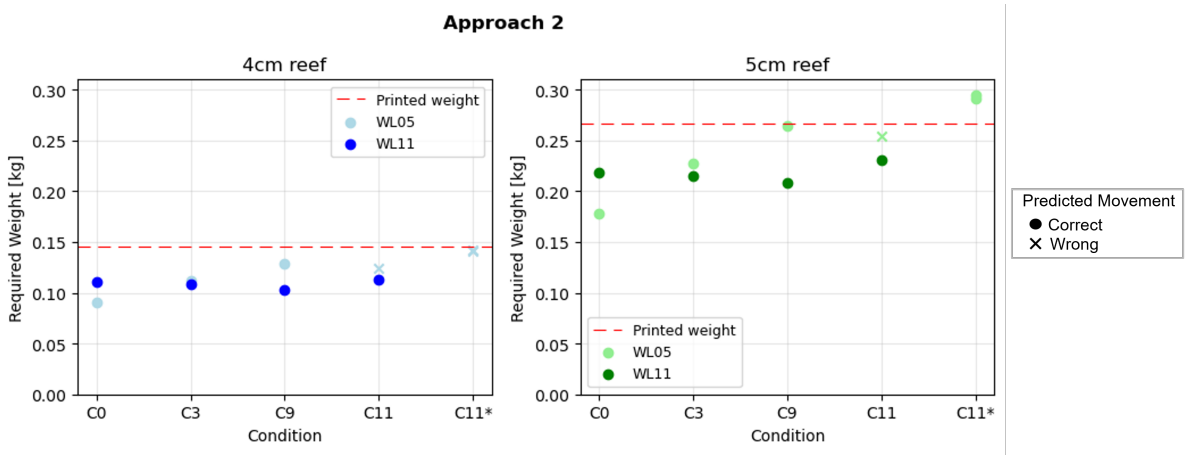

Figure 6.4: Predicted weights for the 4cm and 5cm reef under irregular wave conditions, for Approach 2, o: correct prediction x:incorrect prediction

In terms of comparing the values obtained for the two water levels, it is difficult to generalize which water level imposes the most adverse stability conditions. However, both methods agree that around the transition point, namely for conditions C9, C11 and C11*, the lower water level appears to have higher minimum weight requirements. Furthermore, both approaches consistently predict that for WL11, the required weight lies within a relatively narrow range, with a maximum variation of 0.009kg and 0.014kg, corresponding to approaches 1 and 2. In contrast, the same offshore variation in wave forcing results in a much wider range of required weights under low water level conditions, with a maximum variation of 0.054kg and 0.11kg from apporach 1 and 2 respectively. The wider range of weights required at lower water levels introduces greater uncertainty in the design of a stable reef.

The predictability of the two proposed approaches is further explored using the regular wave experiments. The use of regular waves, which have fewer harmonics, reduces the uncertainty of defining the appropriate wave parameter to represent the sea state. Furthermore, the formulations proposed both by Morison and Sarpkaya were originally developed under regular waves. Therefore, fewer factors are expected to contribute to any discrepancies between the predicted weights and the experimental observations. The calculated required weights for regular waves using approaches 1 and 2 are presented in figures 6.5 and 6.6

Considering that for regular waves all conditions were stable, **approach 1**, appears to predict the stability pattern correctly. It further suggests that WL11 creates more unstable conditions, a fact consistent with the forcing found on the reef, considering the values of both the estimated velocities for the incoming waves in figure 4.6 and the maximum measured velocities found in fig4.5. However, since no movement occurred, there is no transition point to validate the approach's variability. Therefore the apparent agreement between the model and the experiments might be coincidental and does not necessarily confirm the reliability of the approach.

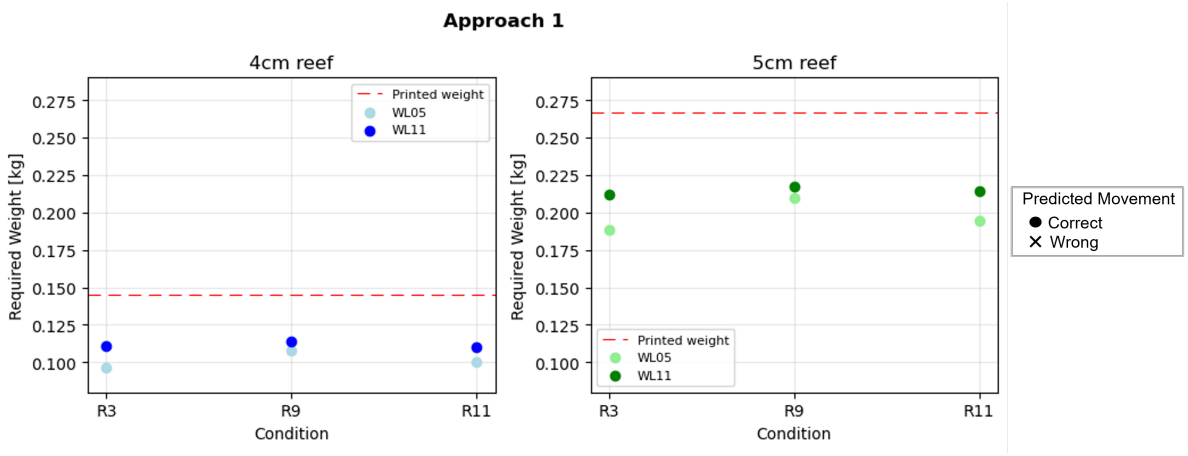

Figure 6.5: Predicted weights for the 4cm and 5cm reef under regular wave conditions, for Approach 1, o: correct prediction x:incorrect prediction

Approach 2 is less consistent with the experimental observations for the regular waves, despite providing more accurate predictions for the irregular wave experiments. Its predictions propose a different stability pattern than the one suggested by approach 1. Specifically, it reverses the trend on which water level is more unstable for conditions R9 and R11, while it also incorrectly predicts instability for condition R3WL11. Therefore, the use of the total wave height appears to over predict the required weight, at least for cases R3WL11.

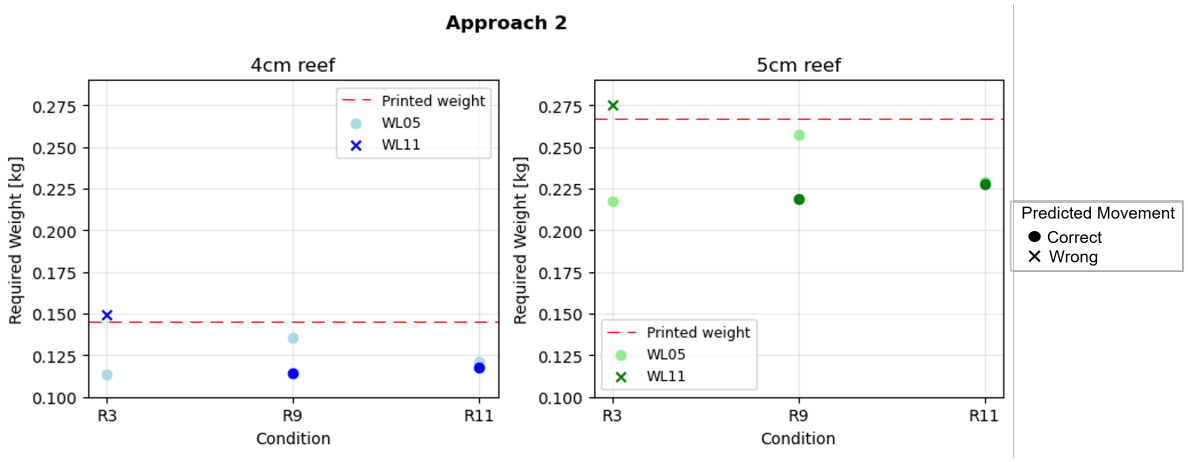

Figure 6.6: Predicted weights for the 4cm and 5cm reef under regular wave conditions, for Approach 1, o: correct prediction x:incorrect prediction

A common behavior observed in both approaches for the regular waves is that the required weights follow the intra-case variation in the estimated velocities, proposed by figure 4.6. In figure 6.7, the contributions of the wave dependent force components, namely the drag, inertia and lift forces, to the total required minimum weight are plotted separately. According to the figure, almost all cases are lift dominated, although, depending on the approach and the case, the impact of the inertia is definitely not negligible. Nevertheless, since the combined magnitude of the lift and drag forces exceeds that of the inertia force, and given that lift and drag scale with velocity while inertia scales with acceleration, it is reasonable to conclude that the required weight is governed by the velocity term.

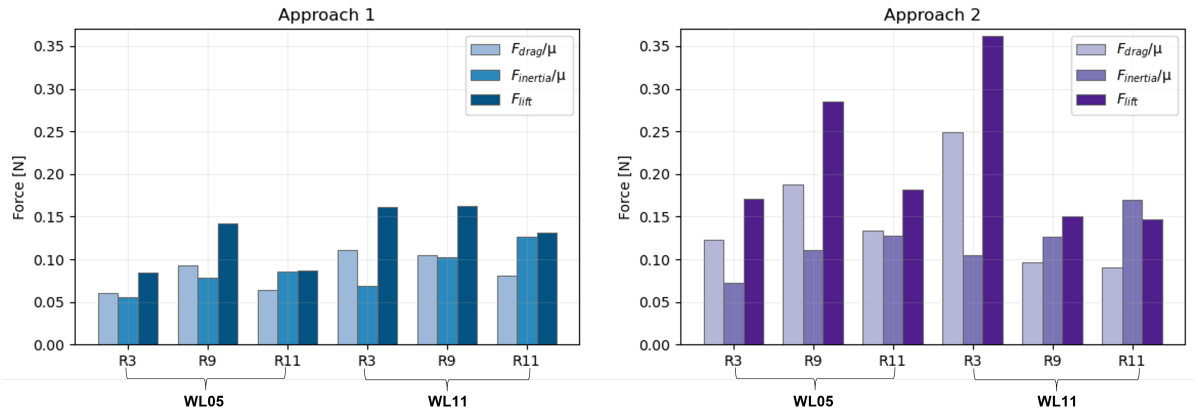

Figure 6.7: Drag, Inertia and Lift components, calculated separately based on the estimated velocity and acceleration, as defined by approaches 1 and 2, for regular waves and the 4 cm AR unit

It appears that for the estimated values of velocity and acceleration, for irregular waves, the use of total waves provides a better representation of the observed stability patterns, according to the results presented so far. For regular waves, this trend is reversed, with approach 1 performing better. As Approach 3 is not applied for regular waves, the following conclusion is drawn:

> For regular waves, using estimated velocity and acceleration as input to the Morison equation appears to yield the most accurate when based on incoming waves rather than the total wave field.

For irregular waves, the analysis of the use of the estimated parameters is extended by examining **approach 3**, with results illustrated in figure 6.8.

Approach 3 provides the most accurate results for the irregular wave experiments, concerning the use of estimated parameters, as most of the cases for both the 4 cm and the 5 cm AR are correctly predicted. In this case, the low water level conditions are clearly more unstable than the WL11 ones, consistent with experimental observations (table 5.1). Furthermore, figure 6.8 shows that the 5 cm reef element is more unstable than its corresponding 4 cm, in agreement with the predictions of approach 2 (Figure 6.4).

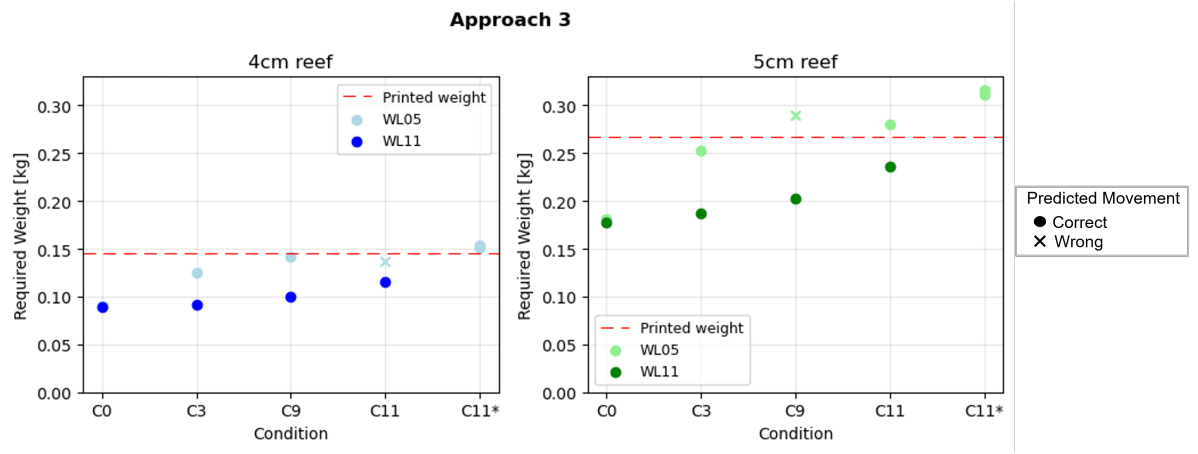

Figure 6.8: Predicted weights for the 4cm and 5cm reef under irregular wave conditions, for Approach 3, o: correct prediction x:incorrect prediction

One remark concerns the identification of the transition point, that the analysis fails to capture. Specifically, condition C9WL05, appears to require higher minimum weight than C11WL05, which incorrectly

implies that it is more unstable. This behavior stems from the magnitudes of the infragravity wave velocities $u_{est,IG}$ being larger for condition C9 than C11, as seen in figure 4.7. Although the sea swell acceleration in C9 is lower than in C11, as shown in figure 6.9, the corresponding inertia force remains smaller than the drag force. The drag force combined with the lift force, account for approximately 73% of the total wave dependent force. Since these forces are velocity dependent, the influence of velocity differences outweighs that of acceleration. Consequently, the higher velocities in C9 lead to a larger required weight for C9WL05 compared to C11WL05.

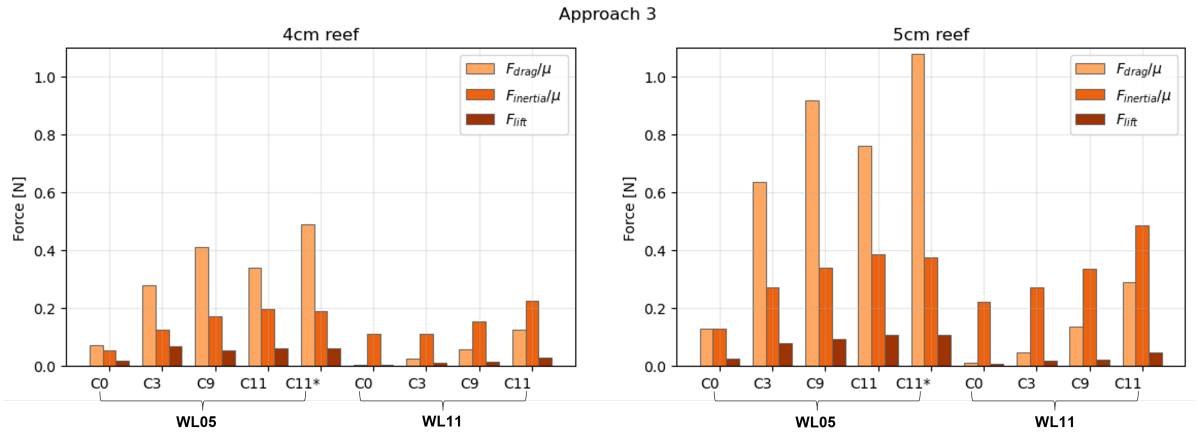

Figure 6.9: Drag, Inertia and Lift components, calculated separately based on the estimated velocity and acceleration, as defined by approach 3, for irregular waves and for both AR units

Approach 3 concludes the analysis of irregular wave conditions with respect to the use of estimated parameters as inputs. Based on the aforementioned, the following is true:

> For irregular waves, using the estimated velocity and acceleration as inputs to the Morison equation appears to yield the most accurate predictions when the total wave field is considered, with the velocity derived from the infragravity frequency band and the acceleration from the sea-swell band.

6.2.4. Predictions using measured parameters

The effectiveness of the Morison equation is subsequently evaluated using the maximum measured values of velocity and acceleration, by testing approaches 4 and 5. The input values of the calculations are found in tables 4.4 and 4.5, while the calculated minimum required weight, are presented in figures 6.10, 6.11 and 6.13.

First, the regular waves are examined, as Approach 5 is not applicable to these conditions. The estimated weights using the measured maximum values, are presented in figure 6.10. The predictions of **approach 4**, according to figure 6.10, incorrectly suggest that the elements were unstable for almost all of the examined cases. Consequently, the weights predicted by this approach appear to overestimate the actual required values.

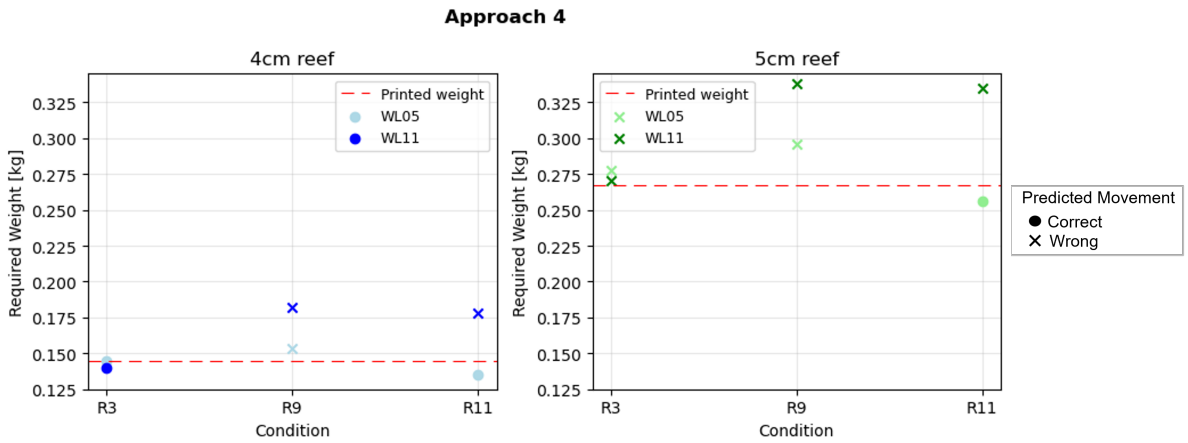

Figure 6.10: Predicted weights for the 4cm and 5cm reef under regular wave conditions, for Approach 4, o: correct prediction x:incorrect prediction

Figure 6.10 presents a similar pattern for irregular waves, with approach 4 again over predicting the required weights, as most wave conditions are incorrectly presumed to be unstable. Given that this trend is consistent for both regular and irregular waves, and that all other parameters such as the force coefficients and the dimensions of the AR units remained constant, the overestimation possibly stems from the magnitudes of the input parameters.

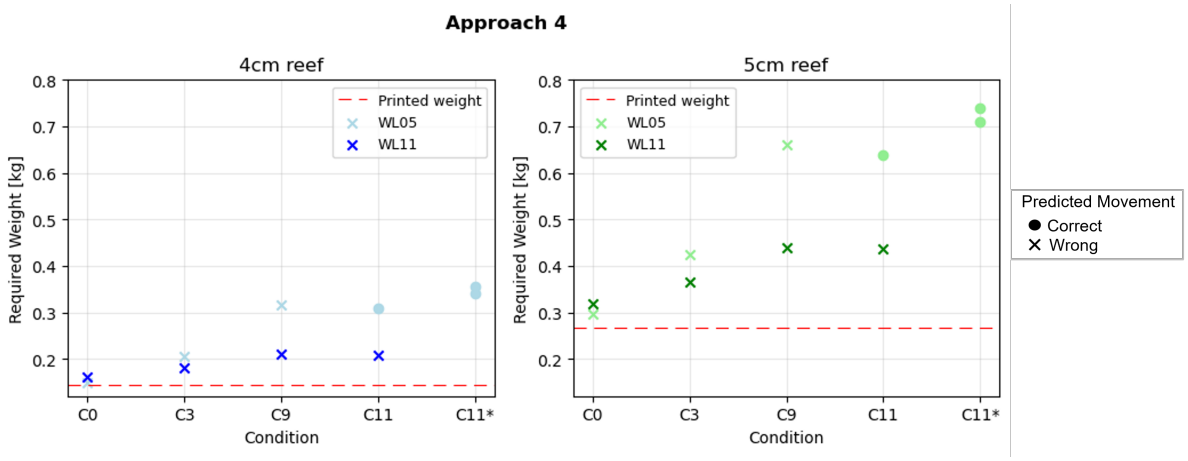

Figure 6.11: Predicted weights for the 4cm and 5cm reef under irregular wave conditions, for Approach 4, o: correct prediction x:incorrect prediction

To understand which parameter influences the results the most, and thus causes that big of an inflation in the predicted values, the force components are plotted. According to figure 6.12, the drag forces dominate the variable part of the force that defines the final required minimum weight of the elements. Especially for conditions C9, C11 and C11* under the low water level, the contribution of the drag force in the total weight is 49%, 45% and 51%Therefore, the velocities of the full frequency band spectrum, combined with the high values of the measured accelerations, lead to the pattern observed in figure 6.11

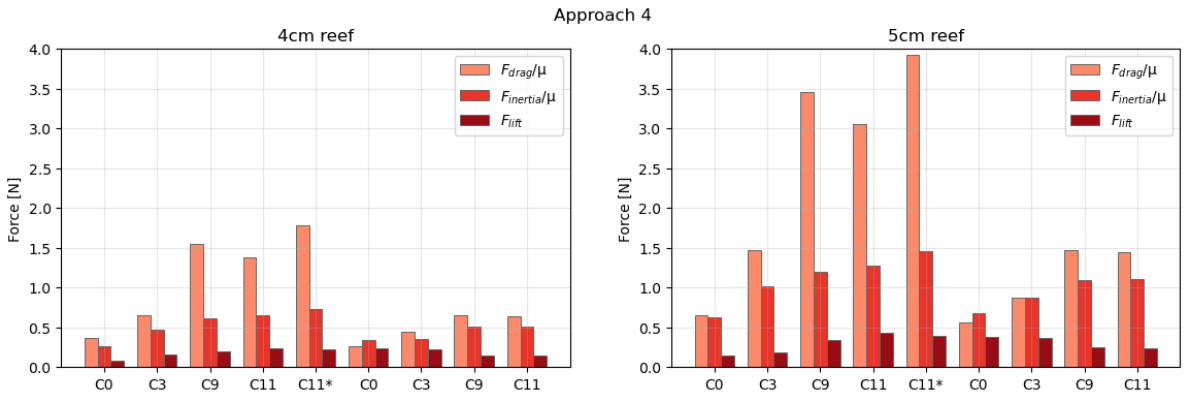

Figure 6.12: Drag, Inertia and Lift components, calculated separately based on the estimated velocity and acceleration, as defined by approach 4, for irregular waves and for both AR units

Lastly, the results considering **approach 5** are presented, with the corresponding estimated required weights shown in figure 6.13. Overall, the predictions demonstrate strong agreement with the observed behavior, with nearly all cases being predicted correctly. WL11 appears to be more stable than WL05, which is consistent with the experimental observations and moreover the transition point for instability between C9WL05 and C11WL05 is captured. Comparing the two AR sizes for C11WL05, further confirms suggests the findings of the previous approaches, that the 5 cm reef is more unstable than the 4 cm one. There is only one incorrect prediction, which refers to C9WL05 for the 5 cm reef. However, the predicted value lies very close to the threshold of motion. Considering this specific case exhibited in fact an almost inconceivable motion, which was neglected to simplify the analysis, the observed discrepancy can be considered small and could likely be accounted for in practical design applications by a safety factor.

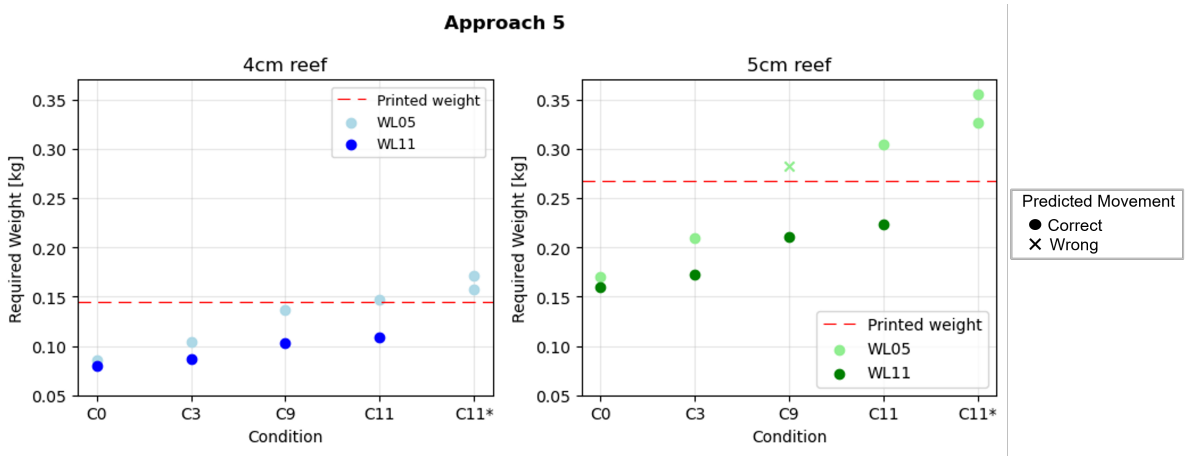

Figure 6.13: Predicted weights for the 4cm and 5cm reef under irregular wave conditions, for Approach 5, o: correct prediction x:incorrect prediction

Taking the above results into account the following can be stated for the use of the maximum estimated parameters:

> The use of the measured parameters overestimates the required weight, for both regular and irregular waves. However, for irregular waves, excluding the contribution of swell in the wave parameter calculation yields the most accurate predictions

7

Discussion

In previous chapters, initial remarks were presented regarding the influence of the fringing reef in shaping the nearshore forcing, together with stability observations obtained from both the experiments and the analytical stability methods considered. In this chapter, these results are interpreted in more detail. The applicability of the two methods, namely the Shields' parameter and the Morison equation, is further examined, along with their respective limitations.

7.1. Uncertainty in defining representative wave parameters

Throughout this report, the parameters adopted to represent the forcing on the reef flat are velocity and acceleration, chosen considering that they constitute the unknown variables in the Shields' and Morison methods which are directly related to wave forcing. In this section, the uncertainty of defining parameters that are representative of the nearshore sea state is discussed.

Two methods have been considered for the calculation of the relevant wave parameters; to estimate velocity by assuming an equivalent linear monochromatic wave, representative of the frequency band explored, whose wave height and period are substituted into equations 2.7 and 2.8, or to use measured quantities obtained from the respective time series of velocity and acceleration.

Concerning estimating the required variables, there exist certain limitations that are required to be valid for the aforementioned equations to approximate the velocity and acceleration on the reef accurately. Specifically, the assumption that the full frequency spectrum can be simplified and efficiently represented by a single monochromatic wave, is appropriate only if the surface elevation spectrum is narrow and has a single distinct peak. Although this is valid for low water level and high energy conditions, in the WL11 cases, this assumption is clearly violated considering that secondary peaks are present (figure 4.1). Furthermore, the foundation of equations 2.7 and 2.8, used to obtain the estimated velocity and acceleration is Linear Wave Theory, which assumes small wave height to water depth ratios. However, the ratios calculated for each wave condition using the time series obtained from the 2 element experiments range approximately from 0.30 to 0.70 indicating that Linear Wave Theory is not completely applicable. In addition, Linear Wave Theory assumes that the waves are not or have not been breaking on the reef flat, which is clearly violated. Lastly, as the name of the theory itself suggests, it is assumed that the substituted wave is linear. This is also not true, as the waves found on the reef flat, even if they are monochromatic for the cases of the regular waves, they become skewed, asymmetric and progressively less linear, as shown in figure 7.1.

Therefore, most of the prerequisite conditions for the equations 2.7 and 2.8 to be safely used, are not satisfied and using Linear Wave Theory to estimate the velocity and acceleration might not produce reliable results.

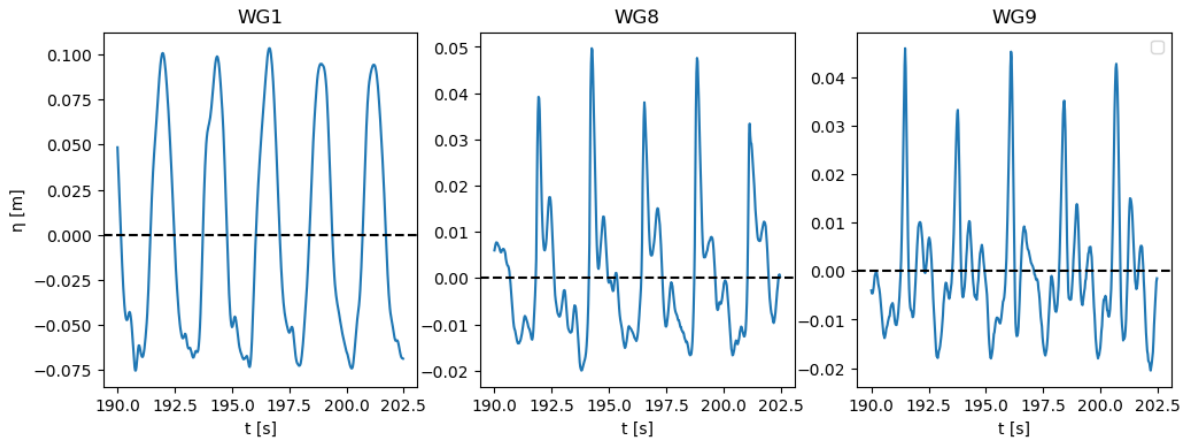

Figure 7.1: Evolution of surface elevation signal from offshore WG1, to the reef flat WG8 and WG9, for condition **R11WL05**

On the other hand, using the measured values might not necessarily be a straightforward improvement. Apart from the difficulties that arise because of the need of extra specialized equipment to record the velocity time series, the main disadvantage of using the measured parameters, is the uncertainty in the accuracy of the acquired acceleration time series. As already introduced in section 4.3, the maximum values of the measured acceleration time series, derived from the differentiation of the velocity one, are significantly larger than the corresponding estimated values. This deviation is further illustrated in figure 7.2, where a comparison between the estimated and measured parameters is presented. Considering the magnitude of the deviation displayed for the full frequency band, it cannot be justified that both approaches are correct in reliably estimating acceleration. The same pattern is observed in the acceleration values for the sea swell waves. The values for the infragravity waves show better agreement compared with the other two groups, however, especially under the low water level, the measured values are twice as large as the estimated ones.

Figure 7.2 indicates that the pattern of the measured parameters being higher than the estimated ones extends to the velocity variables as well. While the differences are less pronounced than for acceleration, the maximum measured values of the full frequency waves and the sea swell waves are, in most of the cases, approximately twice as large as the estimated values. This discrepancy is important when these values are substituted in the stability formulations, as for both the Shields' and the Morison method, the velocity terms scale quadratically. Therefore, the difference between outputs using measured or estimated input parameters magnifies, which explains the higher values found for both the Shields parameter θ and the required weight W_{req} when calculated using measured velocities.

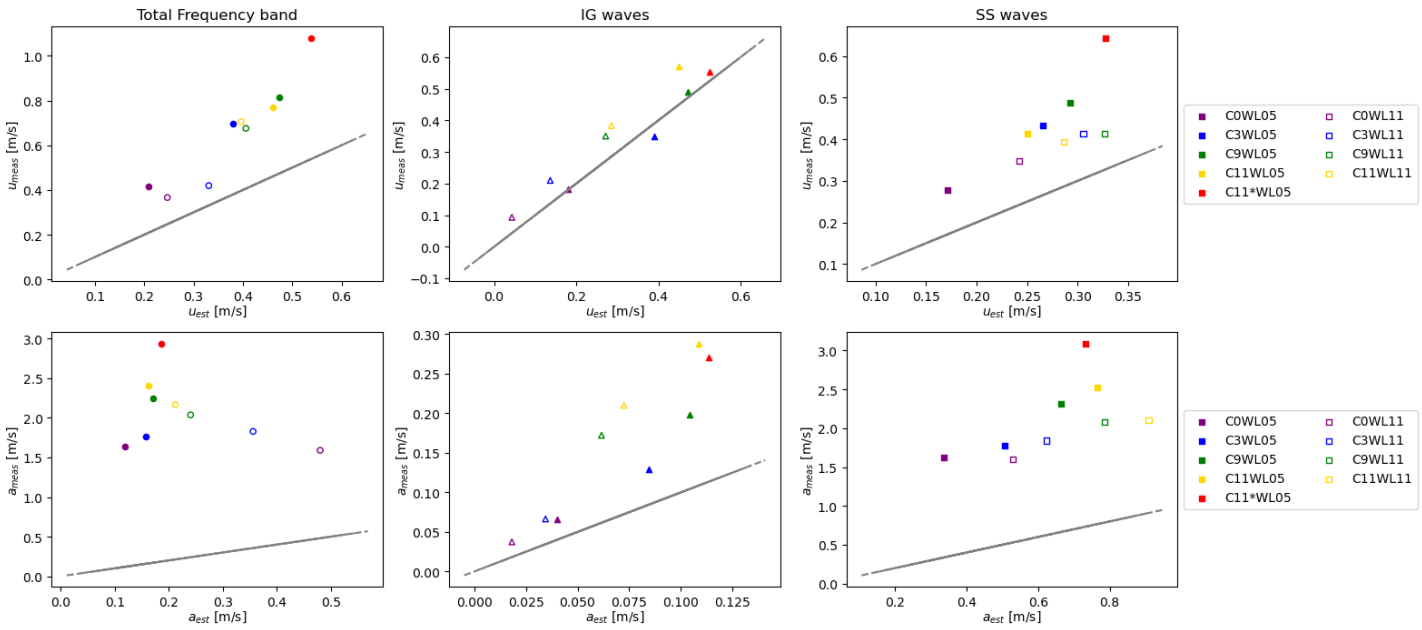

Figure 7.2: Variance density spectra of surface elevation for the total wave field, including both incoming and reflected waves on the reef flat and considering the entire frequency band, for all the explored wave conditions and water levels (WL05:first row, WL11: second row)

An important consideration that should be acknowledged, is that the effect of turbulence is not accounted for in either of the two approaches used to obtain the wave parameters, assumed to be representative of the forcing found on the reef flat, namely the velocity and acceleration. The absence of the influence of turbulence is further not compensated for in the stability formulations explored either, since both the Shields and Morison methods were derived assuming non breaking waves, for which the inclusion of turbulence is not essential. Consequently, the presence of turbulence is completely neglected in the representation of the nearshore hydrodynamic conditions. In the context of a fringing reef, where intense wave breaking is expected, especially under storm conditions, the assumption of turbulence being negligible in shaping the nearshore hydrodynamics becomes questionable. Considering that quantifying the effect of turbulence is a complicated task, completely neglecting it as well, introduces uncertainty regarding the reliability of the obtained stability predictions, particularly in assessing to what extent an agreement between the proposed predictions and the experimental observations, reflects the underlying physics correctly, or arises coincidentally.

7.2. Interpretation of experimental observations

For the regular wave cases, since no unstable cases were observed, it is not possible to observe which forcing generates more adverse conditions in terms of stability.

Regarding irregular wave conditions, the same offshore forcing produces different stability outcomes under the two examined water levels. As an example, considering condition C11 the AR units are unstable for WL05 and stable for WL11, suggesting that a lower water level tends to enhance instability on the reef flat. This result is consistent with the higher velocity values estimated and measured for WL05 compared to WL11 (figure 4.5 and table 4.4). The wave period appears to be another noteworthy factor affecting the stability outcomes, with longer periods (C11* with T_p = 3 sec) associated with more instability.

A parameter that has not been considered in the stability methods is turbulence whose contribution possibly provides an additional explanation for the increased instability observed under lower water levels. Specifically, the vertical spreading of wave breaking generated turbulence, where a lower water depth allows this disturbance to reach the reef units more easily. Therefore the additional forcing associated with the introduced turbulence acted on the artificial reef units, can potentially provide the additional forcing required to initiate movement. The greater vertical spreading for WL05 is depicted in

figure 7.3, where the panels in the first row, show that a larger portion of the AR units is immersed within the the turbulent vortexes. The methods used to predict stability examined, the Shields and Morison method, do not account for turbulence, a fact that might significantly affect the reliability of the results.

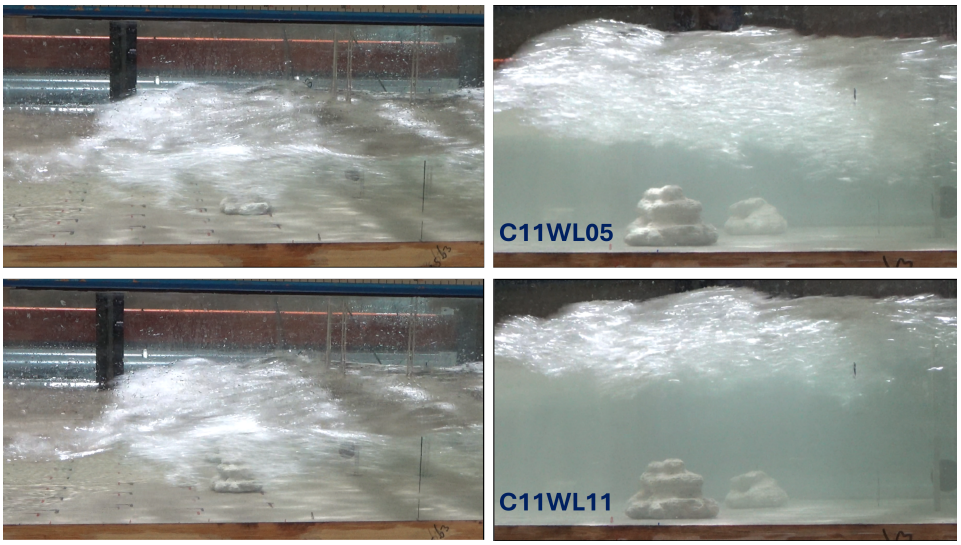

Figure 7.3: Turbulence spreading over the water column during the 2 element experiments, under conditions C11**WL05**:first row and C11**WL11**:second row, shown from two different angles

7.3. Shields' method applicability and limitations

In section 6.1, it was concluded that the Shields' parameter fails to capture the experimentally observed instability patterns for both types of waves, irregular and regular. It was further shown that this misalignment does not stem from the choice of which velocity parameter is considered as characteristic of the nearshore reef hydrodynamics. Therefore, the deviation between predictions and observations can be attributed to inherent limitations in the formulation of the method itself.

Shields developed the method to assess sediment transport over a planar granular bed, consisting of spherical particles and derived the critical θ_{cr} values empirically through experiments that simulated these conditions. In contrast, the artificial reef units considered in this thesis present a fundamentally different behavior compared to the sediment layer that Shields considered, as they are isolated elements that do not exert forces on each other and instead of having a spherical shape, they are characterized by significantly more complex geometries. Consequently, representing the individual artificial reef units by a granular bed, constitutes a substantial simplification. A direct limitation arising from the analogy made, concerns the acting hydrodynamic forcing considered. As mentioned in section 2.2.2, the Shields' parameter is derived as the ratio of the active to the resisting force. For grains in a granular bed, the assumption made by Shields that the driving force is friction caused by the bed shear stress, can be considered reasonable. However, for the isolated artificial reef units used, which are directly obstructing flow and thus drag and inertia forces gain influence, as suggested by Morison et al. (1950), this assumption is no longer representative of the dominant wave forces acted on the artificial reef elements. Another limitation of the method is the fact that it does not account for the turbulence created by the breaking waves.

Considering that many of the assumptions underlying both the formulation of the Shields parameter and the empirically derived range of critical Shields numbers are violated when applied to artificial reef units, the method's inefficiency to predict stability can be justified. However, despite these differences, the variation of the obtained θ values follows the stability trends observed experimentally. Therefore, a newly proposed value of the critical shear stress θ_{cr}, derived from experimental results of the 2 element experiments, could improve the identification of the conditions under which movement occurs.

To identify a new threshold of motion, the transition point between stability and instability has to have been established by the experimental observations. Therefore, it is not possible to safely suggest a

new θ_{cr}^{new} for the regular wave conditions. For the irregular waves, θ_{cr}^{new} is defined conservatively, thus prioritizing that condition C11WL05 could be correctly predicted as unstable, neglecting that such a threshold implies that C9WL05 would be incorrectly predicted unstable. Using the maximum measured velocity as input, the new threshold θ_{cr}^{new} could be defined at 1.65, resulting to the stability pattern presented in figure 7.4.

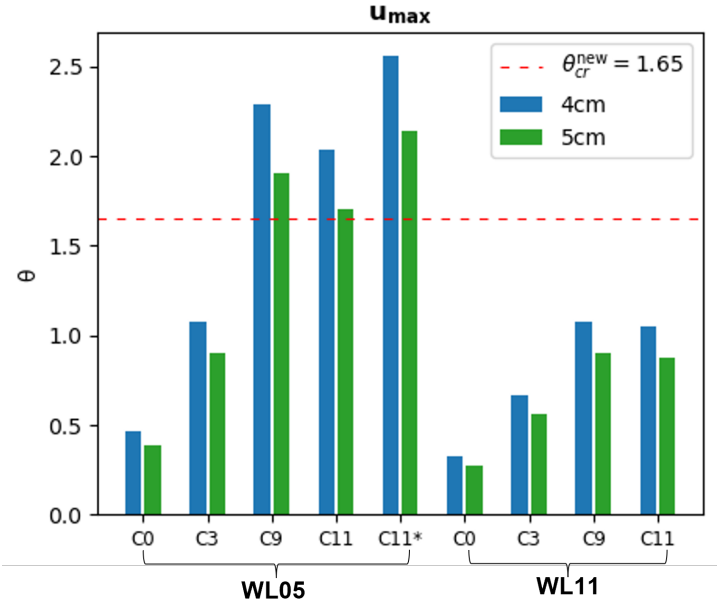

Figure 7.4: Newly defined critical Shields' parameter and Shields' numbers calculated using u_{max} for the two AR designs of height 4 cm and 5 cm for irregular wave conditions

Considering that even with a differently defined threshold of motion, the transition point is not accurately captured, it can be concluded that the Shields' method is insufficient for reliable stability predictions for the given design tested under fringing reef conditions. Furthermore, even though the newly defined threshold can conservatively predict motion, its validity requires further validation through additional experiments that explore a wider range of wave conditions and possibly include large scale experiments.

7.4. Morison Method applicability and limitations

The predictions obtained using the Morison method varied in terms of efficiency in reproducing the experimentally observed stability pattern, depending on the approach used. The discrepancies can be attributed either to the definition of the input variables, or to the formulation of the method itself and its limitations when applied on a complex shaped artificial reef unit in a fringing reef environment. To simplify the interpretation of the resulted minimum required weights, these two categories will be explored independently.

7.4.1. Uncertainty in the input variables

7.4.1.1. Force Coefficients

The force coefficients characterizing the wave induced forces on an obstacle placed in flow, are case specific and depend on the relative roughness of the obstacle's surface and the resulting hydrodynamic forcing governed by the flow-obstacle interaction. Taking into account the unique characteristics of both the shape of the artificial reef units and the resulting nearshore forcing, ideally, the force coefficients should have been calibrated based on force measurements. However, since there were no force measuring instruments available for the experiments, the values of these parameters had to be determined by references reported in literature, which directly introduces uncertainty and potential discrepancies between the used values and the true magnitudes of the coefficients.

Considering the complex geometry of Coastruction's artificial reef element, no studies exist that pro-

vide case specific values for the coefficients specifically derived for this design. Consequently, since no available reference can fully represent the coefficients required, the artificial reef geometry was approximated by a cylinder, as they are the most extensively studied and commonly reported in literature. However, this is an evident oversimplification, implying uncertainty in the results. Among the studies found in literature, the graphs proposed by Sarpkaya (2010) were selected, which as a choice itself, introduces an additional source of uncertainty regarding the validity of the parameters. Furthermore, the advantage of his graphs to partially account for the physical characteristics of the artificial reef units as they include the influence of surface friction in the calculations is also limited. In particular, the range of the relative roughness explored by Sarpkaya's graphs does not incorporate the minimum roughness that Coastruction's elements present, which is expected to increase, once the reefs are deployed to the sea and flora and fauna will be attached to their surface.

The unique pattern of the nearshore forcing conditions found on a fringing reef flat, can be implicitly accounted for, to a certain extent, as the influence of the flow conditions in shaping the force coefficients is represented by the Re and KC numbers. As a result, part of the uncertainty regarding the use of non case specific coefficients can theoretically be mitigated. However, in practice, the correct calculation of the aforementioned numbers requires the substitution of characteristic wave parameters that are not explicitly defined and therefore their selection is subject to interpretation. Especially for irregular waves, where due to the presence of multiple harmonics the definition of one representative velocity and wave period can be defined in various ways, the assumption made that the maximum measured velocity u_{max} and the mean spectral period $T_{m_{-1,0}}$ suffice to adequately represent the hydrodynamic conditions, may not be fully valid and lead to false predictions.

As an example, considering case C11WL11, if instead of the maximum measured velocity, the root mean square velocity u_{rms} was used in the calculations of the Reynolds and Keulegan-Carpenter numbers, their respective values for the 4 cm AR unit would be 7753 and 38, which translates to an approximate 74% decrease. This change suggests different characterization of the flow regime, with the KC number equal to 38 suggesting drag dominance instead of the steady flow conditions (KC equal to 148), found using u_{max}. Subsequently, the values of the force coefficients would be altered and as such, the predictions of the required weights would be different as well.

Most importantly, since the values of the coefficients cannot be verified experimentally, the uncertainty associated with the force coefficients cannot be identified and the validity of any conclusions regarding the applicability of the Morison method under the explored conditions, remains inherently dependent on the assumption that the selected coefficients are appropriate.

7.4.1.2. Wave Forcing

The uncertainty of obtaining the wave parameters itself was discussed in section 7.1. However, identifying the importance of this uncertainty in the obtained results is not straightforward, as isolating the contribution of each parameter to the final required weight remains challenging. Specifically, the interdependence of many of the unknowns in equation 2.16, makes it difficult to directly relate the variation of the input parameters to changes in the resulting required weights. For instance a 5% increase in velocity does not result in a proportional increase in the drag or lift forces, as would be expected from a purely quadratic relationship such as in the Shields method. Instead, changes in velocity also affect the Re and KC numbers which indirectly influence the force coefficients.

In this section, it is assumed that the values of the force coefficients lie within a reasonable range and do not deviate significantly from their true values. This assumption allows to focus on the influence of the wave parameters in determining the required weight.

To assess the influence of the proposed forcing in shaping the range of the required weights, the analysis is focused on a single element, namely the 4 cm artificial reef unit. Comparing the constants of each wave dependent force component in the Morison equation, marked blue in equation 7.1, reveals that the constant part of the inertia term, being equal to 0.15, is one order of magnitude smaller than the respective constants of the drag, equal to 1.4, and lift forces, equal to 1.6. This is attributed to the volume of the ARs being significantly smaller than their planform or cross-sectional areas.

$$W_{req} = \frac{\rho_w A_p}{\mu} C_d \frac{u^2}{2} + \frac{\rho_w V}{\mu} C_m \alpha + \rho_w V g + \rho_w S C_L \frac{u^2}{2} \tag{7.1}$$

Taking into account the resulting force coefficients for each wave condition, further reshapes the balance between the constants, as shown in table 7.1, with the constant of the drag force now clearly dominating the rest two force terms, being 8 to 15 times larger than inertia and 2 to 10 times larger than lift. Table 7.1 explains the drag dominance over the lift forces presented in figure 6.12. This dominance over the lift force, stems from the significantly large KC values, which result into negligible lift forces as the lift coefficients range around 0.25 for most of the cases (table 6.4). Considering that the large KC numbers can be attributed to the morphology of the reef which enhances the low frequency components and thus imposes a large mean spectral period, the lift forces acted on an the artificial reef design used in the CREST experiments, located on a fringing reef environment, will not be dominant.

The inclusion of the C_m coefficients in the calculation, increased the relative contribution of the inertia force in the required weight calculation (table 7.1). However, the magnitude of the inertia constants indicates that only a combination of an acceleration value that is significantly higher than the adopted velocity, can result in inertia being dominant over the drag component.

	Drag constant	**Inertia Constant**	**Lift Constant**
C0WL05	2.663	0.160	0.512
C3WL05	2.019	0.249	0.400
C9WL05	2.280	0.263	0.240
C11WL05	2.263	0.266	0.320
C11*WL05	2.333	0.260	0.240
C0WL11	2.681	0.217	1.920
C3WL11	2.228	0.193	0.928
C9WL11	2.019	0.249	0.368
C11WL11	2.019	0.249	0.368

Table 7.1: Constants of the wave dependent force components for the irregular waves, accounting for the selected force coefficients for each wave condition, for the 4 cm AR

Figure 7.5 presents the wave dependent force components for the full frequency band of the irregular wave cases using approach 2. Both figure 7.5 and 6.12, suggest that considering the full frequency band waves, as performed in approaches 2 and 4, drag is the dominant wave dependent force component. Therefore, velocity is the crucial wave parameter in shaping the minimum required weight to ensure stability, regardless of the method used to obtain it.

This observation suggests that the differences in the predicted required weights between approaches 2 and 4, shown in figures 6.4 and 6.11, are governed by the deviation in the measured and estimated velocities, instead of the discrepancy found in the accelerations. This is initially counterintuitive, given that the measured acceleration can be up to 15 times larger than its corresponding estimated value, as proposed by condition C11WL05 shown in figure 7.2, whereas the velocity values differ only by a factor of two. Nonetheless, it indicates that the uncertainty regarding the correct representation of the acceleration values found on the reef as discussed in section 7.1, is existent but not critical in defining the required weights, considering the full frequency spectrum.

Consequently, these findings suggest that the misalignment of the predictions of these approaches with the stability observations of table 5.1, are not primarily driven by uncertainties in the technical determination of the wave parameters, but rather by other factors such as the definition of the force coefficients or inherent limitations of the method. Between the two, approach 2 underestimates the required weight, while approach 4 overestimates it. Although the absolute magnitude of the prediction error cannot be fully validated, approach 4 not only incorrectly predicts movement in 77% of the cases, compared to 22% of approach 2, but also exhibits significantly larger deviations. Specifically, the maximum overestimation reaches 148% (condition C9WL05 for the 5 cm AR), whereas the maximum underestimation associated with approach 2 is 14% (condition C11WL05 for 4 cm AR). Therefore, assuming that the uncertainty in the force coefficients and the limitations of the method are neglected, using the full frequency band waves, the velocity and acceleration describe instability better when the estimated values are used for the wave parameters instead of their measured values.

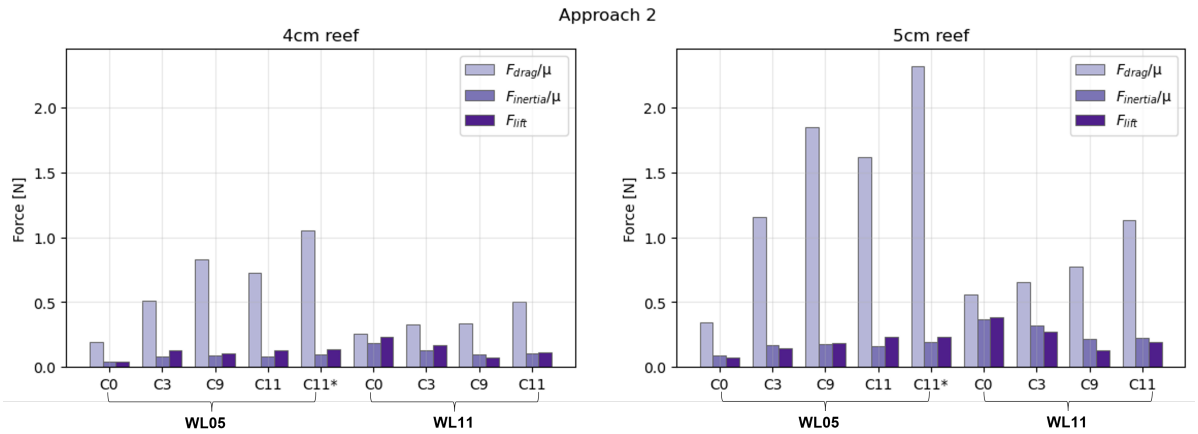

Figure 7.5: Drag, Inertia and Lift components, calculated separately based on the estimated velocity and acceleration, as defined by approach 2, for irregular waves and for both AR units

If the influence of the infragravity waves and the sea swell waves is considered separately and specifically the sea swell waves are used to calculate acceleration, the inertia term can dominate under certain conditions. Such conditions are found when approach 3 is employed under the high water level, shown in figure 6.9. In these cases, the magnitude of the acceleration is at least 13 times larger than the magnitude of the velocity squared.

However, as the inertia dominance is only observed under the high water level conditions, as shown in figures 6.9, for the low water level conditions which correspond to the most unstable cases, all approaches are in agreement that instability is dictated by velocity. Since the transition point is observed for WL05, the low water conditions are of primary interest, for which, the previously discussed uncertainties associated with the acceleration time series remain valid.

A final observation concerns the Reynolds numbers corresponding to the wave conditions tested, which fall within the resistance crisis regime identified in the force coefficients graphs (figure C.3 and C.4). As a result, the conclusion that velocity is the dominant parameter governing instability, cannot be generalized for any wave condition found on a fringing reef environment, and is limited to the range of conditions explored during the experiments. This is because relatively small changes in the nearshore forcing, can result in pronounced differences in the force coefficients thereby altering the balance between the dominance of velocity term contribution over the acceleration one in defining the required weight.

7.4.2. Limitations of the method

7.4.2.1. Assumption of Simultaneous Maximum Velocity and Acceleration

An assumption adopted in the approaches presented in chapter 6.2.3 and in studies found in literature (Diederen (2023), Düzbastılar and Şentürk (2009)) is that the maximum velocity and acceleration occur simultaneously when calculating the required weight. This assumption serves as a reasonable conservative simplification when only the surface elevation time series is available, however, as it is not valid for propagating waves, it leads to an overestimation of the minimum required weight. In the context of approaches 4 and 5, this overestimation can be avoided, using the obtained time series to construct the drag, inertia and lift force components. Subsequently, the signal of the minimum required weight can be composed, accounting for the correct phasing between velocity and acceleration.

To quantify the magnitude of the simplification, imposed by assuming the maximum velocity and acceleration occurring concurrently, the peaks in the minimum required weight series are defined and compared with the values obtained by approach 4. The weights found considering the full frequency band waves, are presented in figure 7.6. As can be seen, the predictions are slightly more accurate, compared to those obtained by approach 4 (figure 6.11), as the required weight weight proposed using the complete time series has decreased by an average of 17% among the conditions explored. The required weights remain over predicted, although, the magnitude of the prediction error has been re-

duced, with the maximum over prediction found for condition C9WL05, now being 109% instead of 147%.

Applying the same method to approach 5 yields reduced required weights as well, albeit the average reduction among cases is smaller, being 5%. The predicted weights for approach 5 obtained by the constructed time series can be found in figure C.6 in the Appendix.

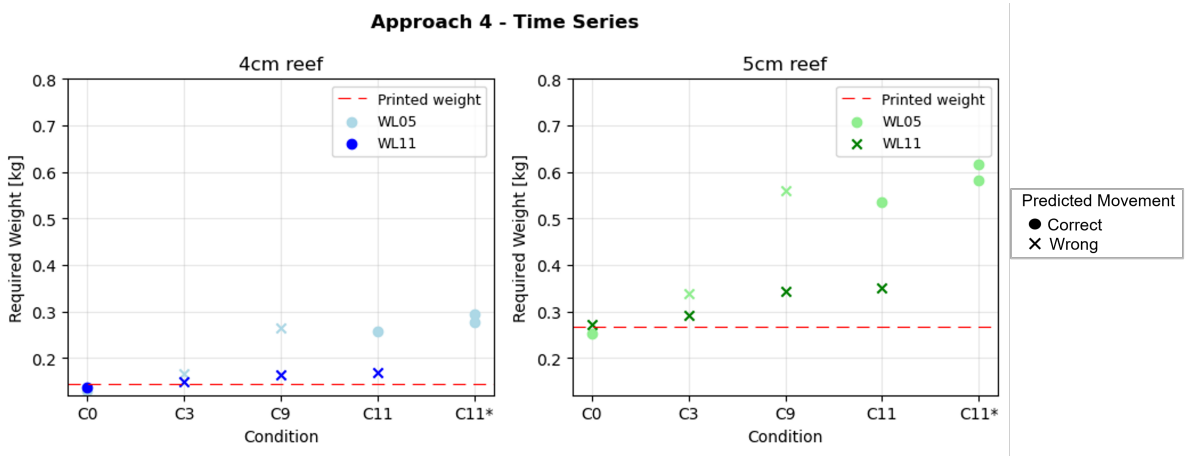

Figure 7.6: Predicted weights for the 4cm and 5cm reef under irregular wave conditions, using the required weight time series considering the full-band frequency total wave field, o: correct prediction x:incorrect prediction

An advantage of plotting the full time series of the required weight, is that it allows to identify how frequently movement is predicted as it can indicate the exact moment motion is expected to occur. As such, two examples of the constructed weight time series are presented in figure 7.7, where the required weight calculated separately for each frequency band, along with the corresponding peaks observed for each are shown. The figure corresponds to the 5 cm AR unit, for conditions C3WL05 and C11*WL05, where C3 is incorrectly predicted to be unstable according to approach 4, (both figures 6.11 and 7.6), while C11* is correctly predicted to be unstable.

Assuming that movement is expected when the predicted required weight exceeds the printed weight (consistent with the definition applied in chapter 5), the peaks of each signal in figure 7.7 indicate that the characterization of C3WL05 as unstable using the full frequency band (approach 4), stems from 14 exceedances of the printed weight by the required weight. For condition C11*WL05, the threshold of motion is exceeded a total of 103 times. The number of these exceedances evidently contradicts significantly the number of times movement was initiated as reported in section 5.1. Therefore, it can be inferred that:

> Using the full frequency band to calculate the required weight is not suitable for accurately predicting the occurrence of motion, unless an alternative definition of when movement occurs is adopted.

In contrast, the peaks in the required weight using the infragravity waves (approach 5), assuming that they are solely responsible for the movement of the AR elements, correctly identify the instances where significant movement was observed for C11* and capture the absence of motion for C3.

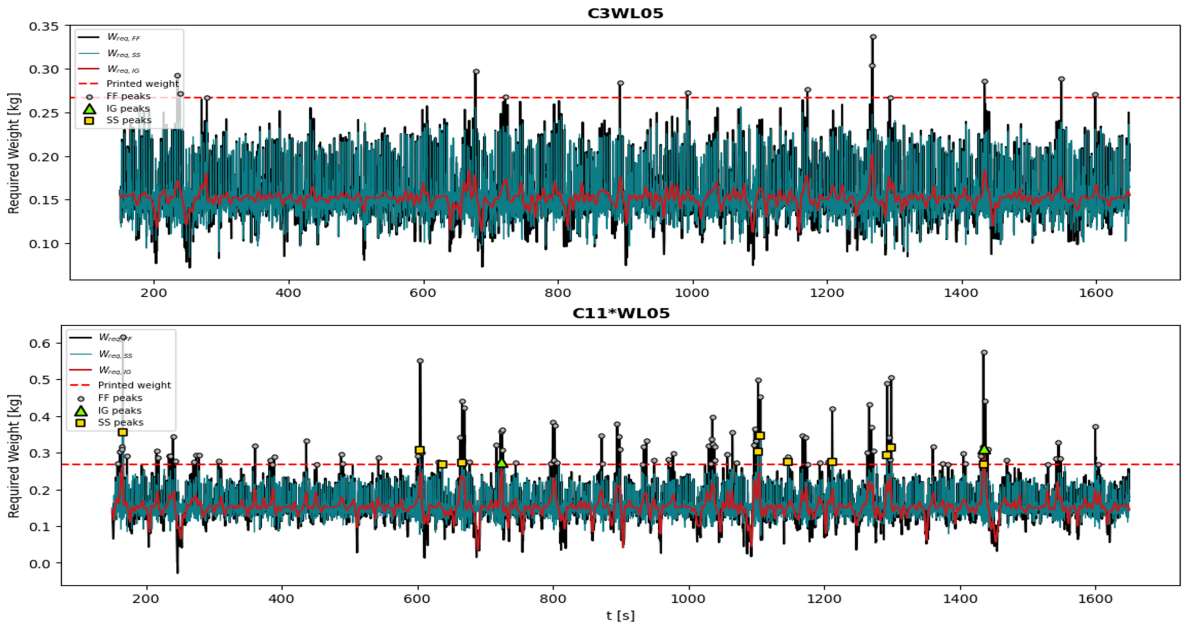

Figure 7.7: Required weight time series, considering the total wave field of the full frequency band, the IG and SS waves, for conditions C3WL05 and C11*WL05. Circle/Triangle/ Square markers: Exceedances of the printed weight by the predicted required weight calculated considering the FF, IG or SS respectivelly

7.4.2.2. Applicability of the method in a fringing reef environment

If the possibility of incorrectly predicted force coefficients is neglected and with the limitation of the non simultaneous occurrence of the maxima of velocity and acceleration addressed, the inability of the full frequency band to accurately predict stability, is attributed to inherent limitations of the Morison formulation applied in a fringing reef environment. In particular, as the Morison method was originally developed for regular waves, adaptations of it for irregular waves exist, but so far do not differentiate the contribution of the different frequency band components in stability. Given that the nearshore forcing on a fringing reef flat is characterized by both infragravity and sea swell waves, it is possible that the inefficiency of both approaches 2 and 4 to capture the resulting stability patterns therefore stems from the fact that they do not distinguish the influence of these two frequency bands in the required weight.

The improved performance of approaches 3 and 5, which adopt a frequency dependent representation of stability, further supports that argument. However, both approaches cannot be considered perfectly valid alternatives without further research, as they entail limitations that raise concerns regarding their ability to accurately represent the underlying physical processes. Specifically, in the approaches considered, the contribution of the sea swell or infragravity waves in stability was examined separately, assuming that the two frequency bands propagate independently and are thus uncorrelated. However, the following figures; 7.8 and 7.9 indicate otherwise.

Figure 7.8 presents a segment of the calculated wave dependent forces acting on the 5 cm AR element, considering the full frequency band, for condition C11WL05. It can be observed that the signal of the drag force component appears to be oscillating in multiple timescales, corresponding to both infragravity and sea swell waves. This is consistent with the fact that the measured velocity shows comparable contributions from both the infragravity and the sea swell waves (figure 7.2). Furthermore, it indicates that defining velocity and acceleration using only the dominant frequency band, and neglecting the contribution of the remaining one constitutes an oversimplification in practice.

In the context of approach 3, this simplification represents an underlying assumption that should be acknowledged, as it introduces uncertainty in the results. However, the contribution of the sea swell waves is not entirely neglected in the calculation of the required weight, as it is implicitly included through the inertia term. Therefore, the observation above reflects as a limitation associated with neglecting the correlation between the frequency components. In contrast, for approach 5 which neglects the sea swell contribution completely, the above observation serves to indicate that the method proposes a

representation of the system that is physically inconsistent with the observed forcing conditions.

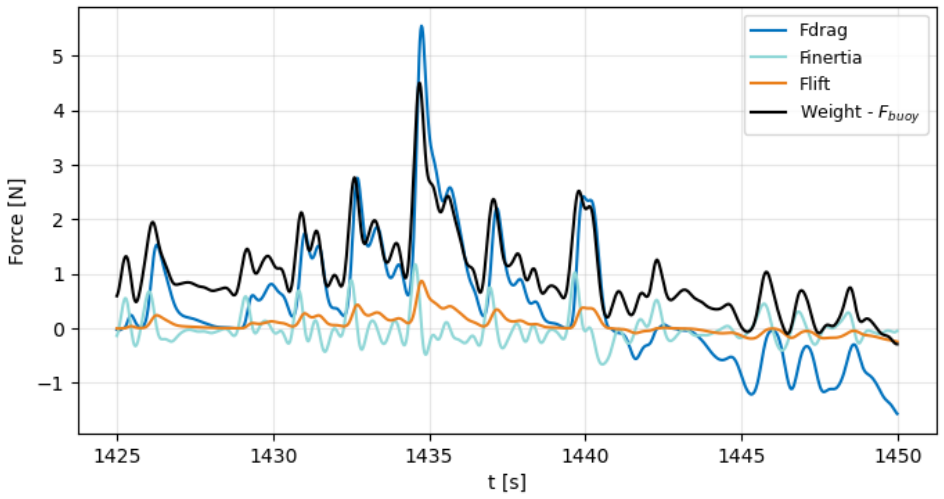

Figure 7.8: Segment of the time series of the drag, inertia, lift and weight forces acted on the 5 cm AR unit, for condition C11WL05

The contribution of each frequency band is further illustrated in figure 7.9, which examines the required weight calculated considering separately the full frequency band, the infragravity and the sea swell waves, under the same conditions as figure 7.8, during the instance when instability was observed. Condition C11WL05 was chosen deliberately as an example, since it exhibits the highest percentage of infragravity waves, suggested by figure 4.3. Despite the high infragravity wave energy found on the reef flat, the pattern of the oscillations of the required weight associated with the sea swell waves component, appears to be imprinted on the oscillations of the required weight of the full frequency band. Consequently, it can be concluded that excluding sea swell waves completely in the calculations of the required weight, as performed in approach 5, does not accurately reflect the hydrodynamic forcing.

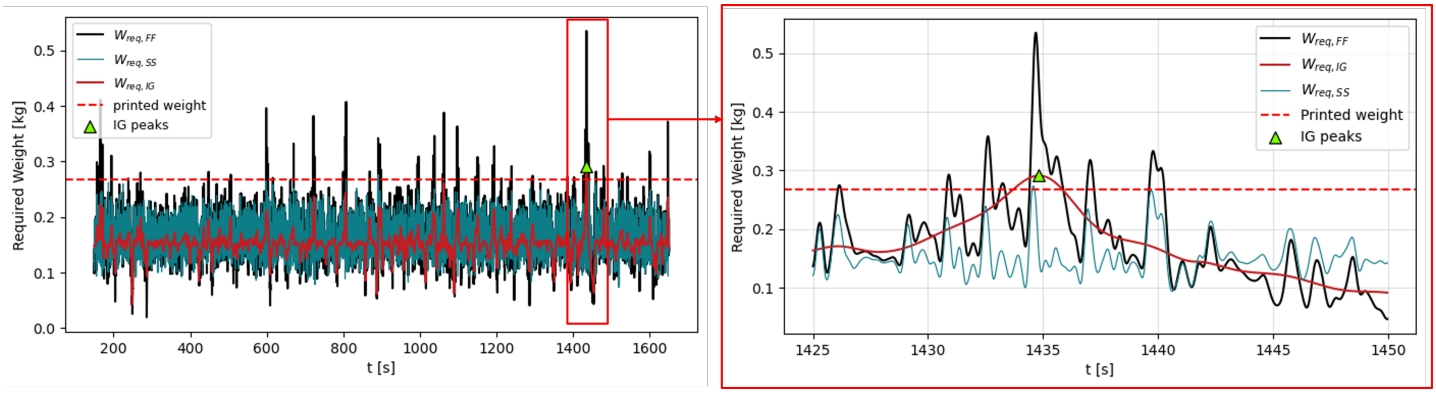

Figure 7.9: Segment of the required weight time series, considering the total wave field of the full frequency band, the IG and SS waves, for condition C11*WL05

Although the formulation of approach 5 is not fully representative of the hydrodynamic processes of a fringing reef, figure 7.9 suggests that its success in predicting the occurrence of motion might not be completely coincidental. As mentioned, the peaks in the required weight signal associated with infragravity waves, consistently identify the instances of significant movement. In contrast, the peaks corresponding to sea swell waves are not systematically translated into motion.

Figure 7.9 indicates that it is the combined effect of the short term fluctuations by the sea swell waves, coinciding with the elevated levels dictated by the low frequency signal of the infragravity waves, that

results in the significant movement observed. Given that the sea swell oscillations are frequent and persistent, when the infragravity wave induced required weight exceeds the threshold imposed by the printed weight, the additional contribution of the sea swell peaks is sufficient to guaranty observable motion explaining the success of approach 5, at least for conditions examined in this study. This behavior further highlights the importance of IG waves in influencing the stability state.

As a result, despite the physical limitations of approach 5, which result in uncertainty regarding the validity of the proposed values of the required weight, it could serve as a useful initial indicator of movement on the reef flat. Although further research is required to assess its applicability under a broader range of conditions, if proven to be effective, its ability to correctly identify the transition point, suggests high practical potential. Furthermore, the uncertainty in the predicted required weight could be mitigated through the application of an appropriate safety factor, used to implicitly account for the neglected contribution of the sea swell waves.

In conclusion, according to the above observations, the conventional application of the Morison equation on a fringing reef environment may require reconsideration, such that the correlation of the infragravity and sea swell waves is correctly accounted for.

7.5. Limitations of the physical model

In addition to factors explored in the previous sections of this chapter, limitations associated with the physical model introduce additional uncertainty into the results.

One source of this uncertainty arises from the possibility that the instruments placed in front of the reef restoration affect the local forcing that the ARs are subjected to, both during the 2 element experiments as well as during the full restoration phase.

As the dimensions of the instruments are small, their presence typically does not affect the flow. However, the side view videos showed that the sequential arrangement of the 4 WGs placed on the flat (WG 5 to 8) occasionally resulted in flow separation around the cylinders they are attached to. During most waves, flow was reattached after propagating by the WG array, and the wave crest regained its shape before reaching the location of the first row of the restoration. Therefore, for the majority of the waves, the influence of the instruments was limited if not insignificant. However, there exist some instances, as the ones presented in figure 7.10, where flow separation due to the WGs resulted into a wave crest that was no longer perpendicular to the flume. Defining locations 1 and 2 as the positions where the AR are placed, as indicated in figure 7.10, it can be seen that especially in image b of figure 7.10, that the crest evidently propagates faster at location 1 than 2, resulting in the tilted crest that is presented on the photo. The presence of the EMF may further enhance this imbalance, with location 1 experiencing higher forcing than location 2, which may explain the movement patterns presented in 5.1.

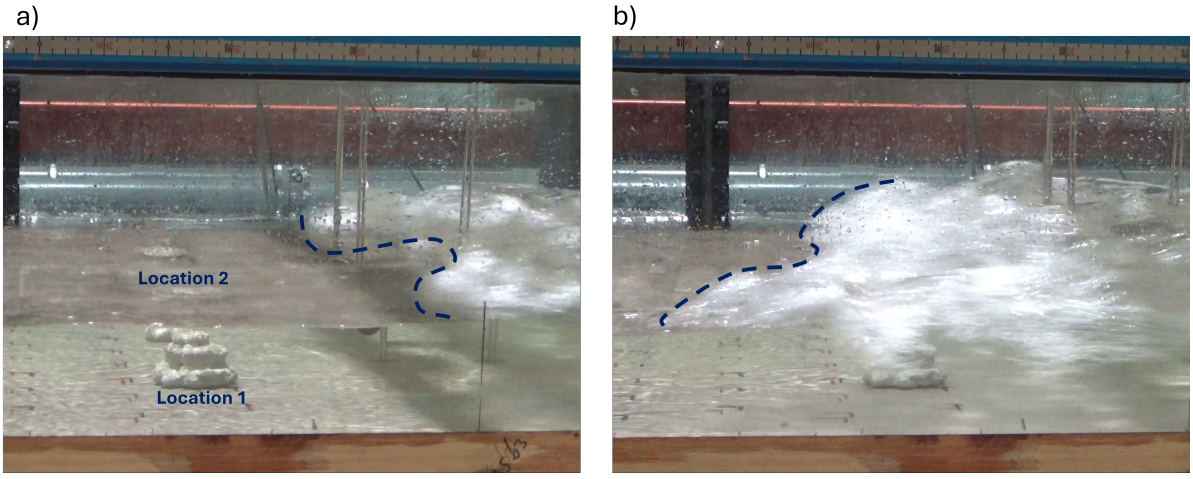

Figure 7.10: Side view snapshots illustrating two instances in which the presence of instruments in front of the AR restoration resulted in a) flow separation and b) asymmetric forcing across the cross-section

A direct consequence of the possibility of asymmetric forcing, is that it complicates the comparison of the stability between the 4 cm and the 5 cm ARs based on experimental observations, making it unreliable to classify either unit as more unstable. This is due to the inconsistent trends observed in the 2 element experiments where under conditions C11WL05 and C11*WL05_Op the 4 cm unit covered a greater distance than the 5 cm, whereas for condition C11*WL05 the opposite is true. Among the theoretical approaches considered, the uncertainty remains unresolved, as the Shields and Morison methods provide conflicting predictions regarding which size is more unstable. The Shields method suggests greater instability for the 4 cm unit, while the Morison method predicted the 5 cm to be more unstable.

Although there is no direct answer on which AR was truly more unstable during the 2 element experiments, observations from the full reef experiments where the 5 cm reef was more stable, suggest that a restoration consisting of the 5 cm design would be more resilient.

8

Conclusions

8.1. Conclusions

In this section. the conclusions derived from the entire report are summarized. That being said, the main research question that frames the research documented in this report is the following:

> **What is the hydrodynamic stability of the artificial reef design previously used in the CREST project?**

The main research question is further dissected by following sub-questions, presented and answered below.

> 1. How is the offshore wave climate affecting the hydrodynamic stability of individual artificial reef units of varying height over a fringing reef?

Which is further analyzed into:

> 1.a How does the presence of a fringing reef transform the offshore wave climate into the hydrodynamic forcing that reaches the shore?

The reef's steep slope imposes significant offshore energy dissipation and redistribution, resulting to dominance of the infragravity waves over the sea swell waves.

The reef's steep slope induces intense and concentrated depth induced wave breaking leading to energy dissipation and infragravity (IG) wave generation through the moving break point mechanism. The combined effect results in substantial portion of the energy initially contained in the Sea Swell (SS) frequency band offshore being either dissipated or transferred towards the low frequencies. For the low water level conditions tested (WL05), the reduced water depth available (5 cm on the reef flat) enhances wave breaking intensity, which can be quantified by the wave height attenuation rates measured in at the location of WG8, which is placed in front of the artificial reef restoration on the reef flat. In particular, for WL05, attenuation reaches up to 69% for the most energetic case, C11WL05 ($H_s = 0.21$m, $T_p = 2.31$sec) , compared to 65% found for the same offshore wave conditions during the high water level WL11 (11 cm still water depth on the reef flat). Since infragravity wave generation is proportional to the intensity of wave breaking, their presence is more pronounced for WL05, with infragravity wave energy comprising between 32% for the least energetic condition C0 ($H_s = 0.40$m, $T_p = 3.70$sec) to 66% for the most energetic one (C11) of the total wave spectrum. For high water level conditions WL11, there are still distinct peaks in the low frequencies, and thus the surface elevation spectra presents a bimodal behavior, with peaks in both the IG and the SS waves. In this case the contribution of the infragravity waves in shaping the full frequency spectrum is much more moderate, ranging form 4% to 42%.

The reef's slope causes significant reflection which amplifies the resulting forcing

The reef's slope causes significant reflection. For almost all the WL05 cases, the reflection coefficient K_r, defined as the ratio of the incoming to the reflected wave height, is higher than 0.707 implying that more of 50% of the incoming wave energy got reflected. The increased presence of the IG waves on the reef, contributes to the high reflection rates, as cases with high percentages of IG waves, such as C11WL05, tend to reflect more ($K_r = 0.813$), compared to cases consisting mainly of short waves, as C0WL05 ($K_r = 0.628$). Due to superposition of the incoming with the reflected components, the total forcing on the reef flat gets amplified for the location of WG8, with the total wave heights measured increasing up to 28% (C11WL05). This is particularly relevant for the stability outcomes of the artificial reef units under irregular waves, as the total wave forcing found on the reef is better represented considering the total wave field instead of the incoming waves.

The lower water level results in higher velocities The velocities and accelerations used as input in the stability formulations are calculated by either th equations 2.7 and 2.8, which are based on Linear Wave Theory, or they are directly measured from the obtained time series. For both approaches, the reef modifies the forcing such that the highest flow velocities are found under low water levels. It is established that velocity is the most representative parameter linking hydrodynamic forcing to structural stability, when considering the full frequency band. Therefore, the occurrence of higher velocities under low water levels, implies that WL05 exhibits greater instability compared to WL11.

1.b Does the presence of infragravity waves on the reef flat, created by the irregular wave field, lead to a greater instability of the units?

The presence of infragravity waves on the reef flat implicitly contributes to a greater instability of the artificial reef units

The presence of infragravity waves influences the resulted forcing, as it results in high mean spectral periods. Especially for a fringing reef bathymetry where the infragravity waves gain dominance under the low water level, the resulted mean spectral period $T_{m_{-1,0}}$ being approximately 17 sec for the cases close to the transition point, (cases C9, C11 and C11* for WL05), contributes to the high values of the Keulegan-Carpenter number observed, ranging from 317 (C11WL05 for the 4 cm reef) to 359 (C11*WL05 of 4 cm reef). The Sarpkaya's graphs, used for the definition of the force coefficients, suggest that KC numbers of that magnitude render the contribution of the lift forces negligible and increase the contribution of the drag forces. Thus, the presence of infragravity waves on the reef flat defines the dominant force component in shaping the minimum required weight.

Furthermore, so far the existing stability prediction methods are not formulated to explicitly account for the distinct contributions of IG and SS waves. As a result, and given that the propagation of SS and IG waves is correlated, the specific influence of the IG on artificial reef stability cannot be directly isolated. Nevertheless, the graphs of the plotted timeseries of the required weights, suggest that the presence of infragravity waves imposes a long scale oscillation of the minimum required weight, while the sea swell components introduce short term fluctuations. Considering that if the calculation of the required weights is performed utilizing only the sea swell wave components, no movement is predicted, it is implied that it is possibly their combined effect that helps provide the additional forcing necessary to exceed the stability threshold during periods when the IG-induced baseline is elevated. In fact, even though neglecting the presence of sea swell waves is not physically meaningful, an initial estimation of when instability occurs can be performed by using the maximum measured infragravity wave velocity and acceleration as inputs into the Morison method (approach 5). Then, instability is expected to occur when the required weight imposed by the isolated contribution of the infragravity waves is predicted be higher than the actual printed weight. Nonetheless, further research needs to be done to accurately establish the contribution of each frequency band in the resulting stability patterns.

2. How consistent are the predictions derived from the Morison and Shields' methods, using time series data from the laboratory experiments as input, compared to the observed stability outcomes?

The Shields' method fails to accurately capture instability considering its traditional formulation

The Shields' parameter where calculated using the maximum measured velocity u_{max}, the root mean square velocity u_{rms} and the maximum estimated velocity u_{est}. The resulting values appear to not be able to predict movement using a traditionally defined critical Shields' number of $\theta_{cr} = 0.055$ under the experimentally tested conditions. In particular, the resulting Shields' parameter values range from 0.3 for C0WL11 to 3.13 for C11*WL05 considering the 4 cm artificial reef unit, corresponding to values approximately 10 to 100 times higher the critical Shields number. The values obtained for the 5 cm reef are 16% lower, however they remain within the same order of magnitude. Although the use of the estimated velocity u_{est} reduces the magnitude of the threshold exceedance, resulting to a range of values from 0.11 (C11*WL05) to 0.77(C0WL11) for the 4 cm case, the predicted values still fail to capture the observed stability pattern. The use of the root mean square velocity results θ values around the 0.055 threshold, however, as they incorrectly predict conditions C3WL05, C9WL11 and C11WL11 as unstable, the use of the u_{rms} is not advised.

Acknowledging that the assumptions under which the method was developed are violated, a new critical value θ_{cr}^{new} equal to 1.65 is proposed, based on the use of the maximum measured velocity, which improves the performance of the method. The threshold is selected conservatively, and as a result is incorrectly classifies condition C9WL05 as unstable. In fact, as the resulting velocity for C9WL05 is higher than C11WL05, the transition point of instability cannot be predicted accurately using the Shields method, regardless of the threshold chosen.

Therefore, although further experimental validation is required, it is expected that the method will fail to reliably predict the resulting motion for wave climates similar to these of C9WL05 and C11WL05. Considering that the Shields approach is intended to provide an initial estimate of stability, its inability to correctly identify the transition point, renders its application questionable in the context of the current conditions.

The effectiveness of the Morison method depends on the definition of the input parameters in regards to the type of waves examined

Assuming that the force coefficients are correctly predicted, the values of the required weights predicted varies depending on how the input parameters are defined. For regular waves it is concluded that the Morison method best reflects the observed stability results when the estimated parameters are used, considering the forcing resulted from the incoming waves (approach 1). On the contrary, the use of the total wave field, that incorporates the effect of reflection into the results, apparently overestimates the minimum required weights, as the predicted values exceed the measured weights and thus suggest movement, despite all tested conditions being stable. Furthermore, since no movement occurred, the predictability of approach 1 cannot be generalized under any given wave conditions and thus requires further testing.

For the case of irregular waves, several options were explored in terms of how to most accurately represent the resulting nearshore forcing. Examining the resulting forcing of the full frequency band, it is concluded that approach 2, which uses estimates of the velocity and acceleration based on the total wave field, results in more reliable predictions than approach 4 that instead uses the maximum measured quantities of these two parameters. Nevertheless, neither approach suffices to perfectly define instability, as approach 2 under predicts movement while approach 4 over predicts it. Instead, possibly due to the distribution of the total wave energy between infragravity and sea swell components, treating the contribution of each frequency band separately leads to more effective results. Approach 5 presents the most accurate predictions, which uses the maximum measured values considering the independent propagation of the resulted infragravity waves found on the reef flat. However as the presence of the sea swell waves appears to be not negligible in shaping the required weight, opting for approach 5 implies accepting a representation of the reef that is not physically meaningful. Conclusively, the most appropriate approach to predict stability from the ones proposed, is approach 3. Approach 3 uses the values of the estimated parameters, accounting for the dominance of IG waves in the velocity term and the dominance of SS waves in the acceleration. Specifically, the drag and lift forces that are a function of velocity are calculated using the IG waves, and the inertia force is proportional to acceleration, is calculated using the SS waves. The method fails to capture the transition point, since C9WL05 is predicted to require a larger weight than C11WL05 thus incorrectly implying that it is more

unstable. Additionally, for the 4 cm reef, the predicted required weight for condition C11WL05 (0.137kg), is smaller than the printed one (0.145kg), incorrectly suggesting that the AR was stable. To account for such discrepancies, although relatively small, and to maintain a conservative design approach, a safety factor of 1.10 is proposed if the method is to be applied future reef design.

8.2. Recommendations

In this section, some recommendations are mentioned that could help improve and expand the current research or assist future experiments with similar objectives.

8.2.1. Recommendations to reduce uncertainty in the present study

According to the data obtained in the present study, Approach 3 was considered the most applicable method for the stability assessment at hand. However, further steps are required before its effectiveness can be confirmed. The first logical step in this direction is to reduce the uncertainty in the obtained results. Following any or even a combination of the proposed suggestions would significantly benefit the study.

Obtain case specific force coefficients: This can be performed either directly by the use of force measuring instruments during the experiments, or alternatively through numerical simulations. By combining force measurements with time series of velocity and acceleration, the force coefficients in the Morison equation can be calibrated using a regression analysis. This is performed assuming a phase difference of 90 degrees between velocity and acceleration, which allows the separation of the contribution of the drag and inertia forces in the horizontal force. Although this method still entails limitations, the uncertainty regarding the force coefficient will be reduced. Thus the reliability or more importantly, the misalignment observed in the present results of the proposed approaches to the experimental observations, will be more easily directed towards either the miscalculation of the force coefficients, or the inability of the method itself to give reliable results under the conditions explored.

Create a bigger dataset of conditions: Since most of the approaches failed to identify the transition point between conditions C9WL05 (Hs = 0.16 m, Tp = 3 sec) and C11WL05 (Hs = 0.21 m and Tp = 2.31 sec), it would be valuable to create more conditions around this threshold. This allows to assess both the approaches' sensibility and the physical limits of stability even further. Thus, the period and wave height of condition C9 could be incrementally increased to produce more unstable cases, while the period of C11 can be reduced, to introduce more stable conditions until movement is no longer observed. Furthermore, considering that both approaches 3 and 5, rely on a spectral approach of stability, varying the percentage of the IG waves in the resulted nearshore forcing is key in creating a more robust dataset.

Address the hypothesis of the asymmetric forcing: To assess whether the placement of the measuring instruments did indeed influence the stability results, the 2 element experiments should be repeated, for conditions C11WL05 and C11*WL05, after removing all measuring instruments from the reef flat. In addition, the experiments should be repeated with position of the 4 cm and the 5 cm AR units reversed within the same transect(as performed in C11*WL05 and C11WL05_Op). The resulting movement patterns would then provide a direct indication of which element size, 4 cm or 5 cm, is more unstable under identical forcing conditions.

Obtain a value for the required weight W_{req}: In the present experiments, the classification of a prediction as correct or incorrect is based solely on whether the predicted weight exceeds the printed one, implying that movement is expected. However, there is no validation against the actual required weight for instability. One suggestion to determine the true required weight empirically, would be to subject an AR element of the exactly the same design and dimensions under the same forcing conditions while systematically varying its weight. An idea on how to practically achieve that, given the limitations discussed in the printing process, would be to create a hollow AR unit that can be assembled from two components in a watertight manner. The internal cavity could then accommodate a sphere of varying weights, thus dictating a controlled variation of the total weight of the element, while maintaining its external geometry.

Perform the experiments in a larger scale: Due to unexpected obstacles encountered during the overall printing process, the final geometry of the artificial reef units is neither a fully accurate scaled

down representation of the intended design from CREST, nor is it consistently replicated across samples. A direct consequence of that is the limited ability to upscale the obtained results. Furthermore, as the issues appear to be difficult to eliminate at a small scale, conducting the experiments at a larger scale would help avoid these problems, consequently improving the reliability and the applicability of the results to real conditions. Additionally, performing the experiments in a large scale implies that the possible asymmetry in the forcing observed due to the small scale nature of the experiments will be mitigated.

8.2.2. Recommendations for further analysis on the existing data

Perform a statistical analysis on the minimum required weight time series: By fitting an appropriate probability distribution to the observed peaks, a probabilistic description of instability can be developed. An alternative definition of movement could also be explored based not only on the instantaneous occurrence of exceedance, but also on its magnitude and its duration. As such, some exceedances can be characterized as statistically insignificant in terms of movement, which would help explain the large number of peaks observed in the full frequency band signal.

Explore the effectiveness of the Morison method using alternative force coefficient definitions: Different approaches can be considered, either by evaluating alternative formulations found in literature, or by using Sarpkaya's graphs with modified input parameters for the calculation of the Reynolds and Keulegan-Carpenter numbers. Regarding the use of other approaches from literature, although they will not be specifically tailored to the conditions examined, they could still be evaluated in terms of their effectiveness in predicting stability. Examples include following the guidelines proposed by USACE (1984) as well as more innovative approaches like Hölzer and Sommerfeld (2008). Furthermore, the coefficients used were assumed to be constant for all the different approaches explored. However, this assumption may not be fully correct when the influence of each frequency band is explored separately, as coefficients derived using the corresponding frequency band might be more representative. For example, if the inertia term is explored using only the sea swell waves, calculating the corresponding inertia coefficient using parameters obtained from the full frequency can be argued to be inconsistent with the flow characteristics represented by the SS waves alone.

8.2.3. Recommendations for the extension of the research scope

Investigate the influence of scour on stability: Stability formulations that explore the impact of wave forces on the stability of an element, typically assume a fixed bed which provides uniform support. However, in practical applications, considering that most likely the ARs will be placed on a sandy bed, this assumption is no longer completely valid. Seabed erosion and specifically scour, can reduce the contact area between the units and te bed, resulting to uneven load distribution. As a result, the stability of the structure may be compromised and therefore, a full stability analysis should account for that effect as well.

Perform the full reef restoration experiments in a hydraulic basin: The experiments performed explored the unidirectional interaction of waves with the proposed design. Given the asymmetric design of the AR units used, a comprehensive stability assessment should include different wave attack angles, by varying the orientation of the units relative to the flume axis. While performing the experiments on a flume suffices to explore the hydrodynamic stability of isolated elements, as the conditions developed represent a simplified approximation of the complex three dimensional forcing encountered in reality, spatial flow patterns which become important for the stability of the full reef restoration are not adequately captured. Conducting the experiments in a hydraulic basin allows for the impact of processes such as diffraction, wave propagation angle and the resulting flow redistribution between the units to be properly accounted for.

Explore the influence of turbulence on stability: As the mathematical representation of turbulence is one of the key challenges in hydraulic engineering, many stability formulations refrain to simpler conditions where the effect of turbulence is neglected. However, in fringing reef environments, the reef's steep slope results into significant wave breaking generated turbulence, which introduces additional highly variable hydrodynamic forces. Therefore, not accounting its impact on stability, despite its evident presence of the reef flat, constitutes a considerable simplification and increases uncertainty in interpreting the effectiveness and applicability of the proposed methods to accurately predict move-

ment.

8.2.4. Practical considerations for similar small scale experiments

Improve visibility during the experiments: The reduced transparency and clarity of the water, caused by the residual cement particles in suspension during the experiments, can be mitigated by introducing additives that promote particle flocculation. The formed flocs being heavier will settle thus improving visibility. Furthermore, as both the AR units and the foreshore are constructed from concrete, they have similar colors. In future experiments, it would be more efficient if either the foreshore or the AR elements were painted a different color to create a bigger contrast. This would facilitate the observation of movement.

Improve documentation: To prevent the formation of asymmetric flow patterns that could influence the experimental results, a symmetric instrument layout is recommended , especially for small-scale experiments. In terms of documentation, cameras positioned along the side of the flume provide more reliable footage, compared to plan view cameras, provided that at least part of the element remains continuously submerged. This ensures that the observed motion is not affected by optical distortions arising from refraction as the water level varies. The key limitation of plan view cameras is that, in addition to image distortion due to refraction caused by the moving water level, wave breaking generated turbulence propagating along the flume, makes it difficult to discern individual units and accurately identify movement. If multiple cameras are used simultaneously, it is highly recommended to implement a mechanism that enables remotely controlled synchronized recording across all devices. This ensures that the footage from each camera has the same duration and is temporarily aligned. The synchronization significantly simplifies the analysis as it facilitates the identification of specific moments across different frames.

References

Albers, K. (Feb. 2025). “Artificial Reefs: Effects on Wave Transformation and In-Canopy Flow: Insights from Large-Scale Wave Flume Experiments of a Fringing Reef”. Faculty of Civil Engineering and Geosciences; Supervisors: Dr. M.F.S. Tissier, Dr. R.T. McCall, Dr. A.J.H.M. Reniers, Ir. F. Roelvink, Dr. S.G. Pearson, Ir. S. Haage. MA thesis. Delft, The Netherlands: Delft University of Technology.

Baine, M. (2001). “Artificial reefs: a review of their design, application, management and performance”. In: *Ocean & Coastal Management* 44.3–4, pp. 241–259. ISSN: 0964-5691. DOI: 10.1016/S0964-5691(01)00048-5.

Bonakdar, L. and H. Oumeraci (2015). “Pile group effect on the wave loading of a slender pile: A small-scale model study”. In: *Ocean Engineering* 108, pp. 449–461. ISSN: 0029-8018. DOI: 10.1016/j.oceaneng.2015.08.031.

Bosboom, J. and M. J. F. Stive (2023). *Coastal Dynamics*. Delft, The Netherlands: TU Delft Open. ISBN: 978-94-6366-371-7. DOI: 10.5074/T.2021.001. URL: https://textbooks.open.tudelft.nl.

Buckley, M. L. et al. (2016). “Dynamics of wave setup over a steeply sloping fringing reef”. In: *Journal of Geophysical Research: Oceans* 121.10, pp. 7187–7205. DOI: 10.1002/2015JC011261.

Dalrymple, R. A., J. T. Kirby, and P. A. Hwang (1984). “Wave Diffraction Due to Areas of Energy Dissipation”. In: *Journal of Waterway, Port, Coastal, and Ocean Engineering* 110.1, pp. 67–79. ISSN: 0733-950X. DOI: 10.1061/(ASCE)0733-950X(1984)110:1(67).

Deltares (n.d.). *Experimental Facility: Scheldt Flume*. https://www.deltares.nl/en/facilities/scheldt-flume/. Deltares, Delft, The Netherlands. The Scheldt Flume is a state-of-the-art wave flume with a total length of 110 m, equipped with wave generators at both ends for wave generation and dissipation.

Det Norske Veritas (Oct. 2010). *Environmental Conditions and Environmental Loads*. Recommended Practice DNV-RP-C205. Oslo, Norway: Det Norske Veritas.

Diederen, C. (2023). “Experimental Wave Flume Study: The Stability of an Artificial Reef”. MA thesis. Delft University of Technology.

Düzbastılar, F. O. and U. Şentürk (2009). “Determining the weights of two types of artificial reefs required to resist wave action in different water depths and bottom slopes”. In: *Ocean Engineering* 36.11–12, pp. 900–913. DOI: 10.1016/j.oceaneng.2009.05.004.

Ferrario, F. et al. (2014). “The effectiveness of coral reefs for coastal hazard risk reduction and adaptation”. In: *Nature Communications* 5, p. 3794. ISSN: 2041-1723. DOI: 10.1038/ncomms4794. URL: https://www.nature.com/articles/ncomms4794.

Frostick, L. E., S. J. McLelland, and T. G. Mercer, eds. (2011). *Users Guide to Physical Modelling and Experimentation: Experience of the HYDRALAB Network*. IAHR Design Manual. Lead authors: J. Kirkegaard, G. Wolters, J. Sutherland, R. Soulsby, L. Frostick, S. McLelland, T. Mercer, and H. Gerritsen. Leiden, The Netherlands: CRC Press/Balkema. ISBN: 978-0-415-58439-7.

Gijón, M. A. et al. (2021). “Wave transmission and drag coefficients through dense cylinder arrays: Implications for designing structures for mangrove restoration”. In: *Ecological Engineering* 165, p. 106231. ISSN: 0925-8574. DOI: 10.1016/j.ecoleng.2021.106231.

Gijón Mancheño, A. (2016). “Interaction between Wave Hydrodynamics and Flexible Vegetation”. MSc thesis. Delft, The Netherlands: Delft University of Technology. URL: http://repository.tudelft.nl.

Harris, L. E. (2004). *Stability Analysis for the Submerged Reef Ball Breakwater Proposed for the Mayan Palace Resort, Quintana Roo, Mexico*. Tech. rep. Performed for Ing. Jose Enrique Chacon Gonzalez, Marenter S.A. de C.V., Cancun, Q. Roo, Mexico. Melbourne, FL, USA: Florida Institute of Technology.

Holthuijsen, L. H. (2007). *Waves in Oceanic and Coastal Waters*. Cambridge, United Kingdom: Cambridge University Press. ISBN: 978-0-521-86028-4.

Hölzer, A. and M. Sommerfeld (2008). “New simple correlation formula for the drag coefficient of non-spherical particles”. In: *Powder Technology* 184.3, pp. 361–365. DOI: 10.1016/j.powtec.2007.08.021.

Hughes, S. A. (1993). *Physical Models and Laboratory Techniques in Coastal Engineering*. Vol. 7. Advanced Series on Ocean Engineering. Singapore: World Scientific. ISBN: 978-981-02-0420-4. DOI: 10.1142/1810.

Jonsson, I. G. (1966). “Wave Boundary Layers and Friction Factors”. In: *Proceedings of the Tenth Conference on Coastal Engineering*. American Society of Civil Engineers. Tokyo, Japan, pp. 127–148.

Keulegan, G. H. and L. H. Carpenter (1958). “Forces on Cylinders and Plates in an Oscillating Fluid”. In: *Journal of Research of the National Bureau of Standards* 60.5. Research Paper 2857, pp. 423–440.

Lokesh, A., V. Sundar, and S. A. Sannasiraj (2013). “Artificial Reefs: A Review”. In: *International Journal of Oceans and Oceanography* 4.2, pp. 85–96. ISSN: 0973-2667.

Lowe, R. J. et al. (2007). “Spectral wave flow attenuation within submerged canopies: Implications for wave energy dissipation”. In: *Journal of Geophysical Research: Oceans* 112.C05018. ISSN: 2169-9275. DOI: 10.1029/2006JC003605.

Mendez, F. J. and I. J. Losada (2004). “An empirical model to estimate the propagation of random breaking and nonbreaking waves over vegetation fields”. In: *Coastal Engineering* 51.2, pp. 103–118. ISSN: 0378-3839. DOI: 10.1016/j.coastaleng.2003.11.003.

Miao, Z. (2006). “Effects of water-depth on hydrodynamic force of artificial reef”. In: *Hournal of Hydrodynamics* 1.2, pp. 372–377.

Morison, J. R. et al. (1950). “The force exerted by surface waves on piles”. In: *Petroleum Transactions, American Institute of Mining Engineers* 189, pp. 149–154.

NOAA, N. O. A. A. (2024). *Why are coral reefs important?* https://oceanservice.noaa.gov/education/tutorial_corals/coral07_importance.html. Last updated December 12 2024; accessed October 30 2025.

Pequignet, A. C. N. et al. (2009). “Forcing of resonant modes on a fringing reef during tropical storm Man-Yi”. In: *Geophysical Research Letters* 36. HAL Id: hal-01009305, p. L03607. DOI: 10.1029/2008GL036259. URL: https://hal.science/hal-01009305.

Phan, K. L. et al. (2019). “The effects of wave non-linearity on wave attenuation by vegetation”. In: *Coastal Engineering* 147, pp. 63–75. ISSN: 0378-3839. DOI: 10.1016/j.coastaleng.2019.01.004.

Roshko, A. (1993). “Perspectives on Bluff Body Aerodynamics”. In: *Journal of Wind Engineering and Industrial Aerodynamics* 49, pp. 79–100. DOI: 10.1016/0167-6105(93)90038-B.

Sarpkaya, T. (2010). *Wave Forces on Offshore Structures*. Cambridge, United Kingdom: Cambridge University Press. ISBN: 9780521893701.

Takens, V. (2024). “Optimising Artificial Reef Design through Large-Scale Experiments”. MA thesis. Delft University of Technology.

Tomasicchio, G. R., F. Aristodemo, and P. Veltri (2009). “Wave and current hydrodynamic coefficients for bottom pipeline stability”. In: *Proceedings of the 6th International Conference on Coastal Structures*. Singapore: World Scientific, pp. 1067–1078. DOI: 10.1142/9789814282024_0094.

Trégarot, E. et al. (2023). “Effects of climate change on marine coastal ecosystems – A review to guide research and management”. In: *Biological Conservation* 287, p. 110639. ISSN: 0006-3207. DOI: 10.1016/j.biocon.2023.110639.

USACE (1984). *Shore Protection Manual*. Vol. II. Approved for public release; distribution unlimited. Vicksburg, Mississippi: Department of the Army, Waterways Experiment Station, Corps of Engineers.

A

Data Processing

A.1. Linear Wave Theory

Linear Wave theory provides an analytical solution to the system of equations stemming from the mass and momentum balance, formulated in such a way where they describe the motion of a water particle. During the process of formulating the equations and defining the boundary conditions, the velocity potential function Φ is defined such that:

$$u_x = \frac{\partial \phi}{\partial x}, \quad u_y = \frac{\partial \phi}{\partial y}, \quad u_z = \frac{\partial \phi}{\partial z} \tag{A.1}$$

The solution proposed by Linear Wave Theory is then obtained after neglecting all the non-linear terms in the system of the equations (governing equations and boundary conditions) and is a propagating harmonic wave with constant and relatively small amplitude where the resulted oscillation for the surface elevation is given by:

$$\eta\left(x,t\right) = a\sin\left(\omega t - kx\right) \tag{A.2}$$

Where: a [m] = Wave amplitude, equal to $\frac{H}{2}$
ω [rad/s] = Angular Frequency, equal to $\frac{2\pi}{T}$, where T [sec] is the period of the harmonic wave
k [rad/] = Wave number, equal to $\frac{2\pi}{L}$, where L [m] is the wave length

The velocity potential function assuming all non-linear terms negligible and derived from the Laplace equation, (mass balance equation) is then given by:

$$\phi\left(x,z,t\right) = \frac{\omega a}{k}\frac{\cosh\left(k\left(h+z\right)\right)}{\sinh\left(kh\right)}\cos\left(\omega t - kx\right) \tag{A.3}$$

Combining equations A.1 and A.3 and including the term kx in the phase shift α [rad], the final formulation for the horizontal velocity is given by:

$$u_x\left(z,t\right) = \omega a\frac{\cosh\left(k\left(h+z\right)\right)}{\sinh\left(kh\right)}\sin\left(\omega t + \alpha\right) \tag{A.4}$$

The above formulations represent the propagation of only one wave harmonic, which corresponds to regular wave conditions. In reality, the wave conditions found, are more accurately described by irregular waves, where the signal of the measured surface elevation is much more random. The complex pattern of the surface elevation can be simplified by the **random-phase model** which suggests to assume the total signal as a linear summation of a number of harmonic wave components each (j)

characterized by a frequency f_j, propagating with a constant amplitude a_j and a random phase α_j, that is uniformly distributed between 0 and 2π.

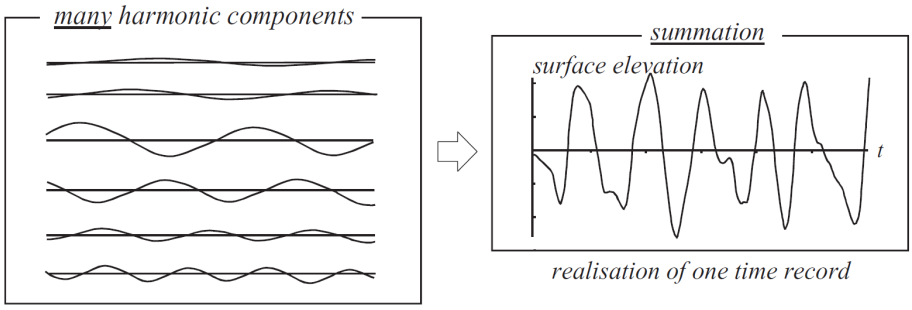

Figure A.1: Decomposition of the random surface elevation signal at sea into many harmonic components of constant amplitude and phase, figure taken from Holthuijsen (2007))

The linear superposition of harmonics implies that Linear Wave Theory is still valid and can be used to represent the motion of the surface elevation and the horizontal velocity. Accordingly modifying equations A.2 and A.4, their formulations for irregular waves are :

$$\eta(t) = \sum_{j=1}^{N} a_j \sin\left(\omega_j t + \alpha_j\right) \tag{A.5}$$

$$u_x(z,t) = \sum_{j=1}^{N} a_j \omega_j \frac{\cosh\left(k_j\left(z+h\right)\right)}{\sinh\left(k_j h\right)} \sin\left(\omega_j t + \alpha_j\right) \tag{A.6}$$

Forming the ratio $\eta(t)/u_x(z,t)$, the relationship between the two signals can be expressed as:

$$u_x(z,t) = \sum \omega_j \frac{\cosh\left(k_j\left(z+h\right)\right)}{\sinh\left(k_j h\right)} \eta_i(t) \tag{A.7}$$

From the dispersion equation 3.6:

$$\frac{\omega}{\sinh\left(kh\right)} = \frac{gk}{\omega\cosh\left(kh\right)} \tag{A.8}$$

Substituting A.8 in equation A.7, ultimately, the kinematic relationship between the surface elevation and horizontal velocity given in 3.5 is formed:

$$u_x(z,t) = \sum \frac{gk_j \cosh\left(k_j\left(z+h\right)\right)}{\omega_j \cosh\left(k_j h\right)} \eta(t) = \sum \frac{gk}{2\pi f} K_{u_j} \eta_j(t) \tag{A.9}$$

Where:

$$K_u = \sum \frac{\cosh\left(k_j h_u\right)}{\cosh\left(k_j\left(h_0 + \overline{\eta}\right)\right)} \tag{A.10}$$

To simplify the calculations for irregular waves, the Fast Fourier Transform (FFT) is applied on equation A.9. The transformation of the equations from the time to the frequency domain, allows for decoupling and results on the formulations given by equations **??**.

A.2. Wave number Calculation

The wave number calculation is performed in the frequency domain using the dispersion equation 3.6 at locations A and B. For each run, the water depth h is assumed constant, equal to the mean measured water-depth at each location. Then, the dispersion equation 3.6 is solved iteratively with the Newton-Rhapson method to determine k_j for each f_j frequency present in the spectrum. Specifically, applied on the dispersion equation to calculate kh, treating kh as the unknown variable, the Newton-Rhapson method defines:

$$kh_{n+1} = kh_n - \frac{f(kh_n)}{kh'(x_n)} \tag{A.11}$$

where:

$$f(kh) = kh \tanh kh - \frac{\omega^2 h}{g} \tag{A.12}$$

$$f'(kh) = \tanh kh + kh\left(1 - \tanh^2 kh\right) \tag{A.13}$$

The initial guess used in each iteration loop, meaning the kh_0 per frequency, is calculated by:

$$kh_0 = \frac{\omega^2 h}{g\left(1 - \exp\left(-\left(\frac{\omega^2 h}{g}\right)^{5/4}\right)^{2/5}\right)} \tag{A.14}$$

The maximum allowed error in the iterations is 10^{-7} and the maximum number of iterations defined is 20. Since h is known in advance, the value of the wave number k_j for each j frequency is calculated as $k = kh/h$.

B

Physical Model

B.1. Location of instruments

WGs				EMFs			
Name	x-positioning [m]	y-positioning [m]	z-positioning [m]	Name	x-positioning [m]	y-positioning [m]	z-positioning [m]
WHM1	22.375	0.50	0.72	-	-	-	-
WHM2	23.475	0.50	0.72	-	-	-	-
WHM3	24.075	0.50	0.72	-	-	-	-
WHM4	24.525	0.50	0.72	-	-	-	-
WHM5	34.954	0.50	0.72	-	-	-	-
WHM6	35.309	0.50	0.72	-	-	-	-
WHM7	35.499	0.50	0.72	-	-	-	-
WHM8	35.630	0.50	0.72	**EMS1**	35.630	0.60	0.82
WHM9	37.550	0.50	0.72	**EMS2**	37.550	0.60	0.82
WHM10	37.950	0.50	0.72	-	-	-	-
WHM11	38.150	0.50	0.72	-	-	-	-
WHM12	38.300	0.50	0.72	-	-	-	-

Table B.1: Detailed positioning of instruments

B.2. Experimental Runs

Table B.2: Summary of wave conditions and measured depths

Condition	H_{m0} input	T_p input	d_{meas}
C0WL05	0.0400	3.7000	0.8503
C3WL05	0.0800	3.7000	0.8503
C9WL05	0.1600	3.0000	0.8503
C11WL05	0.2100	2.3100	0.8503
C11*WL05	0.2100	3.0000	0.8489
C0WL11	0.0400	3.7000	0.9097
C3WL11	0.0800	3.7000	0.9099
C9WL11	0.1600	3.0000	0.9095
C11WL11	0.2100	2.3100	0.9099
C0WL05_R	0.0400	3.7000	0.8491
C3WL05_R	0.0800	3.7000	0.8489
C9WL05_R	0.1600	3.0000	0.8491
C11WL05_R	0.2100	2.3100	0.8491
C11*WL05_R	0.2100	3.0000	0.8491
C11*WL05_R_Op	0.2100	3.0000	0.8497
C0WL11_R	0.0400	3.7000	0.9098
C3WL11_R	0.0800	3.7000	0.9085
C9WL11_R	0.1600	3.0000	0.9103
C11WL11_R	0.2100	2.3100	0.9102
C3WL05_FR4	0.0800	3.7000	0.8490
C9WL05_FR4	0.1600	3.0000	0.8505
C11WL05_FR4	0.2100	2.3100	0.8503
C11*WL05_FR4	0.2100	3.0000	0.8495
C0WL11_FR4	0.0400	3.7000	0.9083
C3WL11_FR4	0.0800	3.7000	0.9083
C9WL11_FR4	0.1600	3.0000	0.9089
C11WL11_FR4	0.2100	2.3100	0.9085
C3WL05_FR5	0.0800	3.7000	0.9493
C9WL05_FR5	0.1600	3.0000	0.8493
C11WL05_FR5	0.2100	2.3100	0.8503
C11*WL05_FR5	0.2100	3.0000	0.8503
C3WL11_FR5	0.0800	3.7000	0.9101
C9WL11_FR5	0.1600	3.0000	0.9097
C11WL11_FR5	0.2100	2.3100	0.9095

C

Wave Forcing

C.1. Variance density Spectra

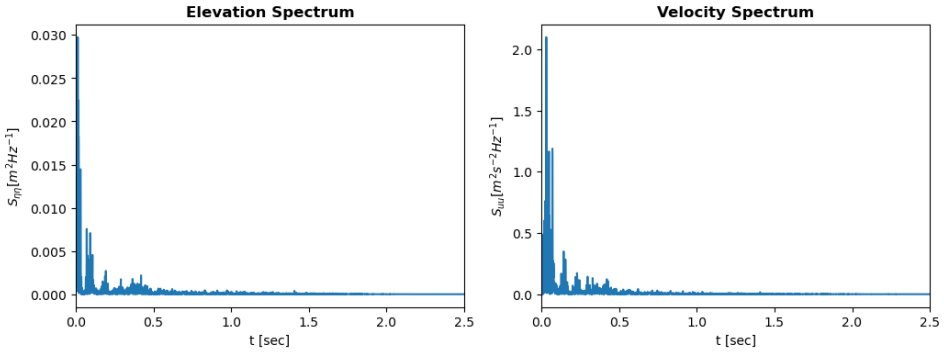

Figure C.1: Surface elevation and velocity spectra

Figure C.2 shows the total velocity variance spectra, the integral of which, gives the u_{rms} of the total near bed velocity signal. The velocity spectra follow the general trend proposed by surface elevation, in the sense that energy gets transferred to lower frequencies for all of the cases and for WL11 short wave components are still significant. One difference is that the peaks for WL05 are higher than for WL11, therefore the moments resulting from the WL05 spectra bigger than the ones in from WL11. Furthermore, the peaks are reduced at location WG9. These observations are depicted in table 4.4 where near-bed velocities decrease with increasing depth and while moving onshore.

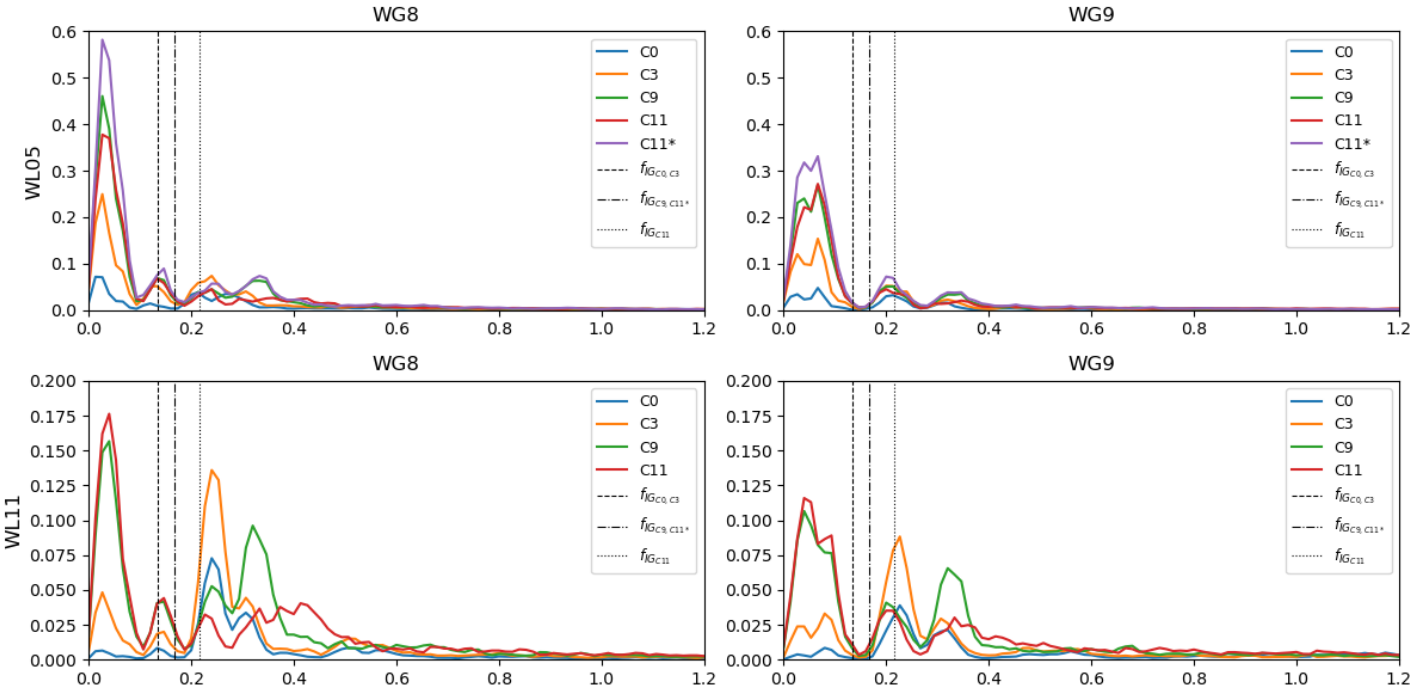

Figure C.2: Velocity Variance spectra

C.2. Precise values of wave parameters

Table C.1: Mean water depth, wave height and wave period at location A, for the incoming waves and total waves considering the full frequency band, the infragravity frequency band and sea swell frequency band for the irregular wave cases

		Total		Incident		IG		SS	
Condition	d_{mean} [m]	H_{m_0} [m]	$T_{m_{-1,0}}$ [s]	$H_{m0,inc}$ [m]	$T_{m_{-1,0},inc}$ [s]	$H_{m0,IG}$ [m]	$T_{m_{-1,0},IG}$ [s]	$H_{m0,SS}$ [m]	$T_{m_{-1,0},SS}$ [s]
C0WL05	0.066	0.035	11.084	0.028	9.207	0.019	28.216	0.029	3.218
C3WL05	0.066	0.061	15.824	0.045	12.911	0.042	29.408	0.044	3.317
C9WL05	0.089	0.087	17.559	0.064	14.253	0.066	28.448	0.056	2.782
C11WL05	0.096	0.085	17.687	0.062	14.510	0.069	25.688	0.050	2.061
C11*WL05	0.103	0.105	17.875	0.076	13.953	0.080	28.684	0.068	2.815
C0WL11	0.110	0.052	3.615	0.040	3.551	0.011	20.360	0.051	2.900
C3WL11	0.125	0.069	5.629	0.056	4.516	0.024	23.883	0.065	3.080
C9WL11	0.188	0.090	10.177	0.076	6.672	0.049	27.569	0.075	2.613
C11WL11	0.135	0.092	11.544	0.070	7.949	0.060	24.560	0.070	1.970

Table C.2: Mean water depth, wave height and wave period at location A, for the total and incoming wave field of regular waves

		Total		Incident	
Condition	d_{mean} [m]	H [m]	T [s]	H_{inc} [m]	T_{inc} [s]
R3WL05	0.071	0.040	3.623	0.028	3.336
R9WL05	0.096	0.057	2.922	0.040	2.913
R11WL05	0.107	0.051	2.057	0.036	2.121
R3WL11	0.115	0.072	3.547	0.048	3.623
R9WL11	0.135	0.051	2.295	0.053	2.922
R11WL11	0.144	0.053	1.633	0.049	2.071

Table C.3: Estimated velocity and acceleration at WG8 using equations 2.7 and2.8, for the incoming waves and total waves considering the full frequency band, the infragravity frequency band and sea swell frequency band for the irregular wave cases

	Total		**Incident**		**IG**		**SS**	
Condition	u_{est} [m/s]	a_{est} [m/s^2]	$u_{\text{est,inc}}$ [m/s]	$a_{\text{est,inc}}$ [m/s^2]	$u_{\text{est,IG}}$ [m/s]	$a_{\text{est,IG}}$ [m/s^2]	$u_{\text{est,SS}}$ [m/s]	$a_{\text{est,SS}}$ [m/s^2]
C0WL05	0.211	0.120	0.172	0.117	0.183	0.041	0.173	0.338
C3WL05	0.396	0.157	0.279	0.136	0.415	0.089	0.268	0.507
C9WL05	0.476	0.170	0.337	0.148	0.475	0.105	0.292	0.659
C11WL05	0.447	0.159	0.317	0.137	0.434	0.106	0.243	0.741
C11*WL05	0.529	0.186	0.371	0.167	0.510	0.112	0.326	0.727
C0WL11	0.245	0.425	0.186	0.329	0.053	0.016	0.238	0.516
C3WL11	0.304	0.340	0.244	0.340	0.118	0.031	0.282	0.575
C9WL11	0.323	0.200	0.275	0.259	0.192	0.044	0.261	0.626
C11WL11	0.392	0.213	0.297	0.235	0.280	0.072	0.284	0.906

Table C.4: Estimated velocity and acceleration at location A, using equations 2.7 and 2.8, considering the total and incoming wave field of regular waves

	Total		**Incident**	
Condition	u_{est} [m/s]	a_{est} [m/s^2]	$u_{\text{est,inc}}$ [m/s]	$a_{\text{est,inc}}$ [m/s^2]
R3WL05	0.290	0.552	0.219	0.443
R9WL05	0.280	0.750	0.221	0.581
R11WL05	0.248	0.890	0.195	0.649
R3WL11	0.405	0.788	0.270	0.547
R9WL11	0.273	0.761	0.271	0.668
R11WL11	0.291	0.999	0.251	0.804

Table C.5: Maximum velocity and acceleration at location A from LPF signals, including total, infragravity (IG), and sea-swell (SS) components

	Total		**IG**		**SS**	
Condition	$u_{\max}$ [m/s]	$a_{\max}$ [m/s^2]	$u_{\max,IG}$ [m/s]	$a_{\max,IG}$ [m/s^2]	$u_{\max,SS}$ [m/s]	$a_{\max,SS}$ [m/s^2]
C0WL05	0.414	1.633	0.181	0.066	0.278	1.624
C3WL05	0.632	1.893	0.342	0.130	0.370	1.911
C9WL05	0.920	2.312	0.508	0.234	0.512	2.331
C11WL05	0.869	2.460	0.542	0.266	0.405	2.232
C11*WL05	0.974	2.810	0.586	0.280	0.622	2.746
C0WL11	0.348	1.583	0.084	0.035	0.333	1.593
C3WL11	0.498	1.846	0.187	0.060	0.392	1.835
C9WL11	0.632	2.049	0.337	0.151	0.387	1.965
C11WL11	0.625	2.058	0.366	0.225	0.424	2.026

C.3. Force Coefficients

As mentioned in Chapter 6.2.2, the force coefficients are determined by the graphs proposed by Sarpkaya (2010), as they include element roughness in their proposed values. However, for figure C.4, the curve corresponding to a roughness of 1/50 does not continue for the low Re numbers calculated for many of the cases, both for regular and irregular waves (tables 6.2 and 6.3). Nevertheless, even though, there is lack of experimentally validated data for these values, the curves will be assumed to continue in a similar pattern as for the rest roughness cases, shown with blue part of the curve. The shape of the curves is also naturally dictated by the governing physics.

More specifically, figures C.3 and C.4 suggest that for both Keulegan-Carpenter numbers, KC = 20 and KC = 100, over a range in the Reynolds numbers, a transition region exists in which the drag coefficient decreases and subsequently increases. This is defined in literature as the *resistance crisis* and is dependent on the nature of the wake formed by the presence of an object in flow (Sarpkaya 2010). Experiments by Roshko (1993) using smooth cylinders under steady flow, show that the resistance crisis observed, was found for Reynolds numbers in the region of 2x10^5 to 5x10^5. For periodic flow around a cylinder, the resistance crisis might occur at smaller Reynolds numbers Sarpkaya (2010), which explains the difference between graphs with KC = 100 where flow approaches steady flow, compared to KC = 20. That being said, roughness apparently moves the transition point towards smaller Reynold numbers.

The line used to extend the curves in the KC = 100 figure, was created taking these considerations into account. Then the values of the C_d and C_m can be read.

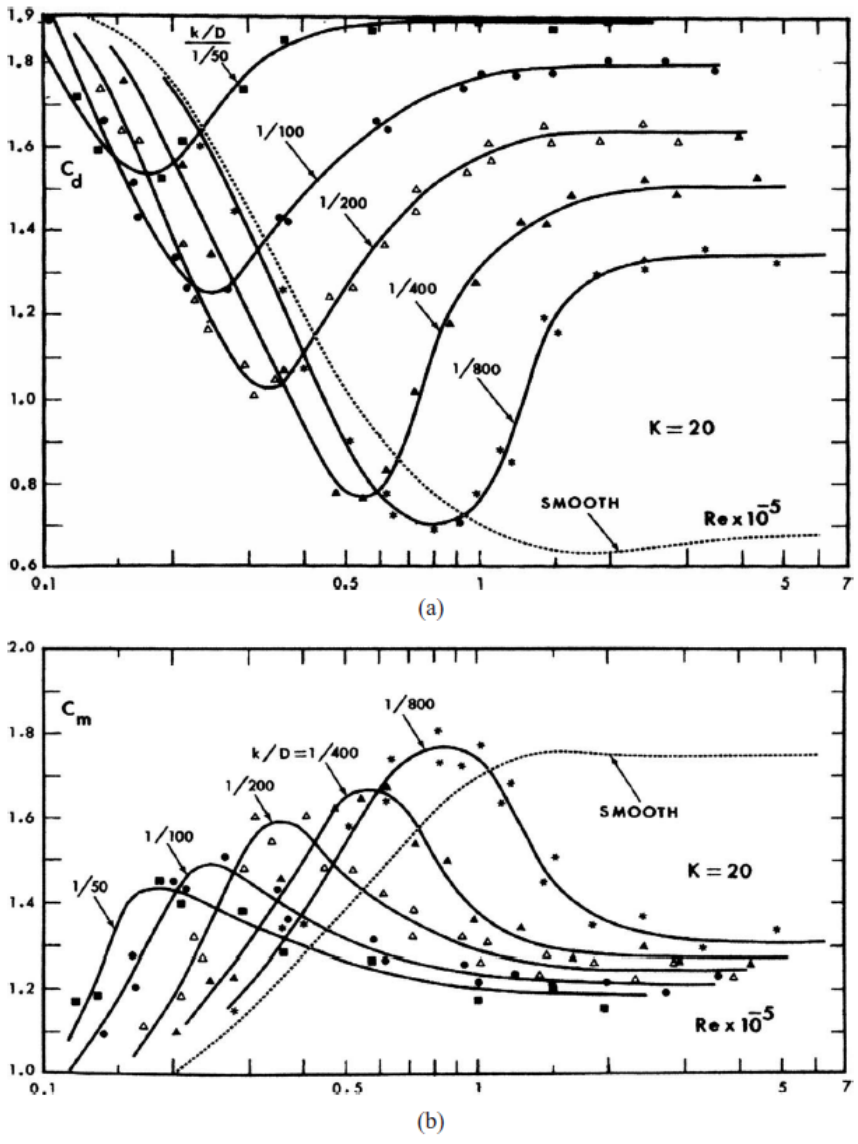

Figure C.3: a. **Cd** versus Re, b. **Cm** versus Re
for rough cylinders, KC = 20, (Sarpkaya 2010)

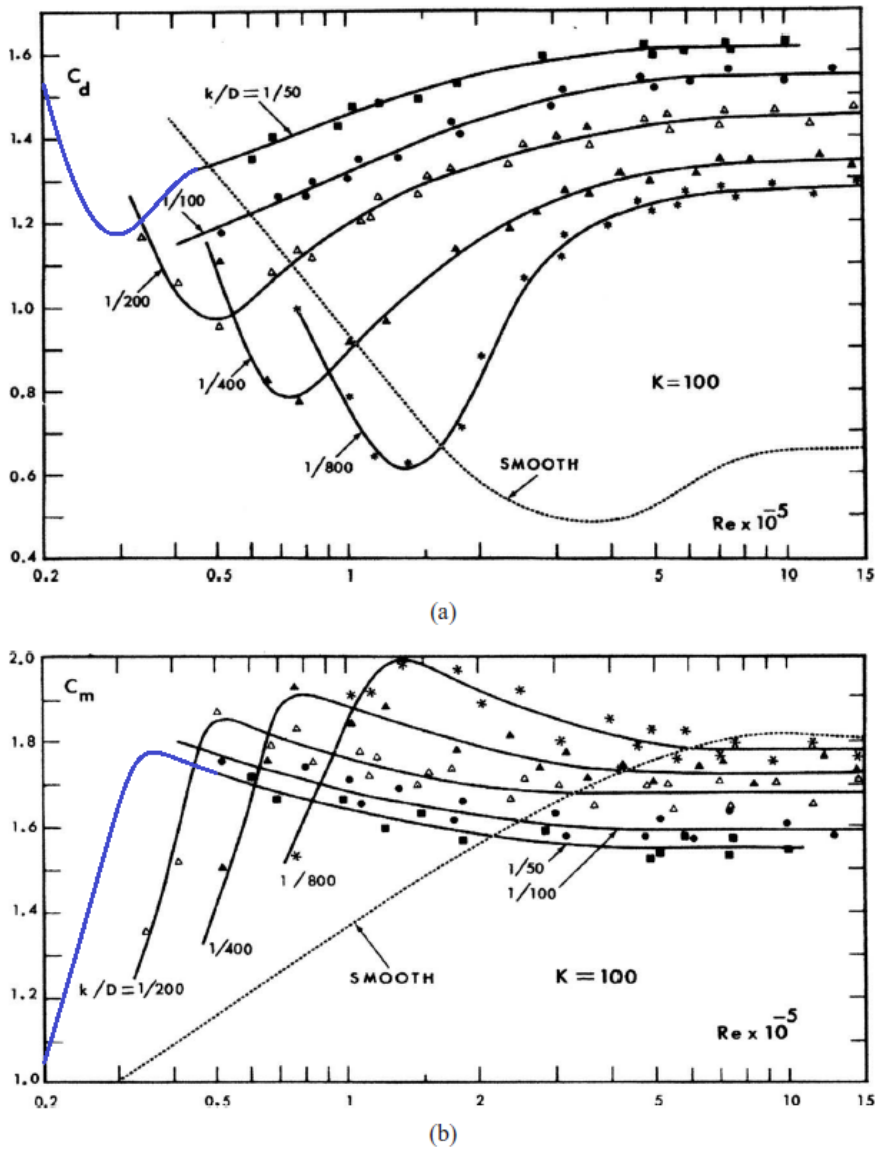

Figure C.4: a. **Cd** versus Re, b. **Cm** versus Re for rough cylinders, KC = 100, (Sarpkaya 2010)

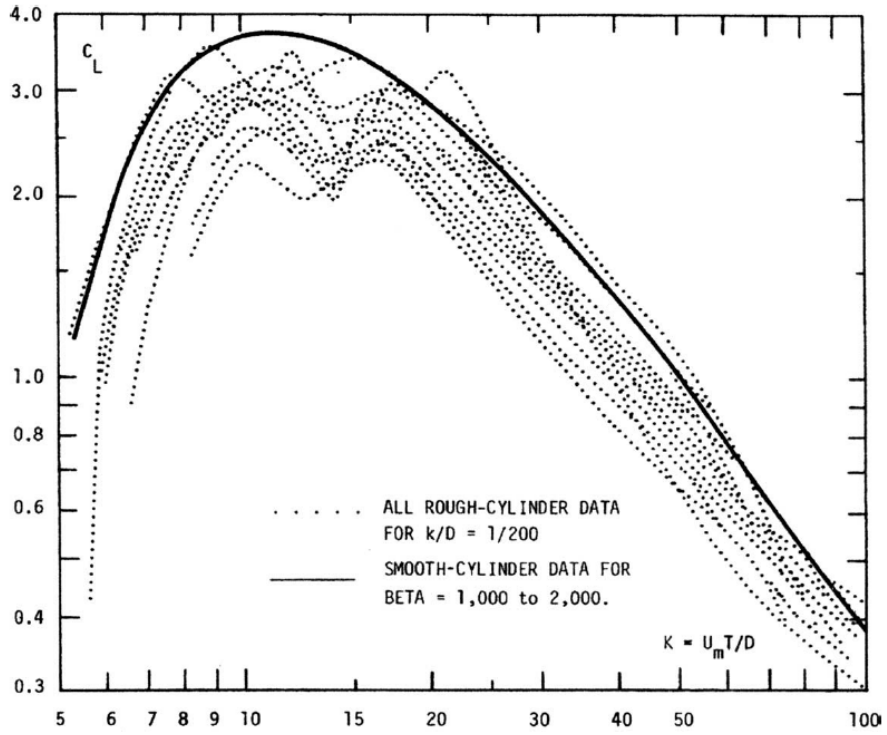

Figure C.5: Lift coefficients for rough cylinders as functions of K for various relative roughnesses (Sarpkaya 2010)

C.4. Stability Results

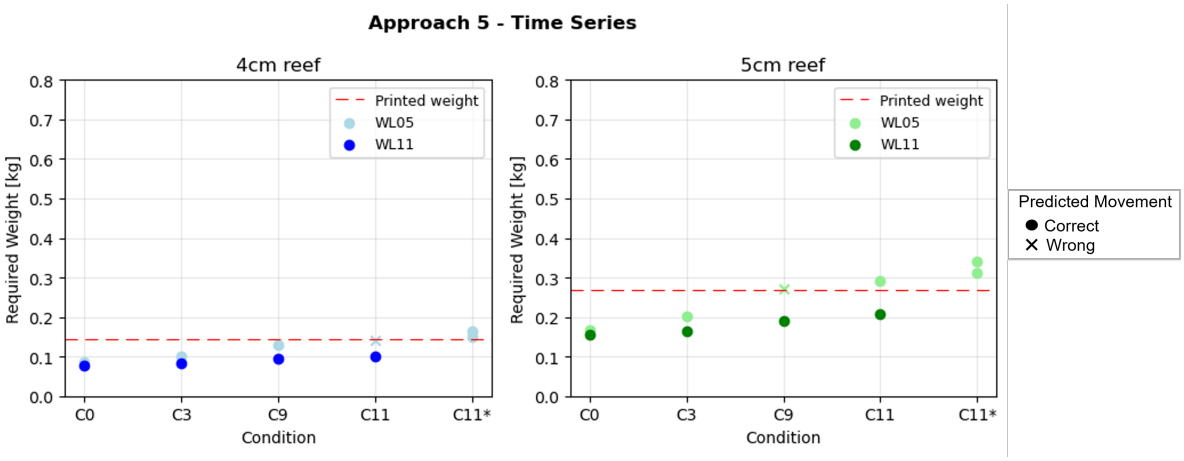

Figure C.6: Predicted weights for the 4cm and 5cm reef under irregular wave conditions, using the required weight time series considering the IG frequency total wave field, o: correct prediction x:incorrect prediction